A fully first-principles approach to the Kondo problem and spin-polarized STM imaging in molecules.

Thesis

Condensed Matter Physics department. Autonomous University de Madrid.

Author:
María Soriano Santacruz
Departamento de Física de la Materia Condensada.
Universidad Autónoma de Madrid.
Spain.

Supervisor:
Dr. Juan José Palacios Burgos
Departamento de Física de la materia Condensada.
Universidad Autónoma de Madrid.
Spain.

2nd December 2014

Contents

Introduction

Cramming more molecules onto quantum circuits

The information society in which we live today has been made possible thanks to the progressive reduction in the size of integrated circuits and memory storage devices. In this context, one of the most self-evident technological indicators of devices scale-down is the progressive increase in efficiency of magnetic memories and microprocessors. The occupied area by memory unit determines this efficiency. Namely, the number of bits per square inch or the number of instructions per second which is capable of processing. Both are functions of the device size.

In 1965 the 35th anniversary of the magazine *"Electronics Magazine"* was celebrated. Gordon E. Moore was asked to write an article in which he predicted the electronics evolution over the next 10 years. In those times, Moore was directing Fairchild laboratories. A semiconductor company founded by Moore himself, along with others, after leaving the William Shockley laboratory. At that time, the integrated circuits were only four years old. Moore had been aware of the number of transistors and resistors replicated each year. Hence, he forecast the same evolution for years to come: *"Certainly over the short term this rate can be expected to continue, if not to increase. Over the longer term, the rate of increase is a bit more uncertain, although there is no reason to believe it will not remain nearly constant for at least 10 years."* [1]. The most complex integrated circuits were made of 64 components, thus he advanced that in the next 75 years, they should have a minimum of 64,000 components. The number of components into integrated circuits followed, more or less, the path that Moore had expected. In 1968, Moore, along with Robert Noyce (other of the founders of Fairchild), founded the company named **Intel**, creating the first microprocessor. In 1975, Moore modified its own law, ensuring that the growth rate would diminish, doubling the integration capacity each 24 months.

Moore's law has an expiration date. We are probably living his last valid decade and right now, in this last stage, is where nanotechnology emerges to keep the present and as an alternative for the future. Nanotechnology refers broadly to a field of applied science and technology whose unifying theme is the control of matter on the atomic and molecular scale, normally 1 to 100 nanometers, and the fabrication of devices within that size range. It is a highly multidisciplinary field, drawing from fields such as physics, materials science, chemistry, biology, robotics and engineering. Nanotechnology can be seen as an extension of existing sciences into the nanoscale, or as a recasting of existing sciences using a newer, more modern term.

It is difficult to find an origin or a father to the nanoscience. Richard Feynman thought that everything could be explained by motions and contortions of atoms. Today he is considered one of fathers of nanoscience thanks to his talk titled: *"there is plenty of room at the bottom"* which encourages researchers to go further on the atomic scale, [2]. Already then, he proposed outlandish ideas for that time as writing the Britannica Encyclopedia on the head of a pin.

However had to spend several years before the nanotechnology would become in a science with own name.

In 1981 G. Binnig and H. Rogher initiated a new era of surface science field inventing the **S**canning **T**unneling **M**icroscope (STM) [3]. In 1986, just five years later, they received the Nobel Prize in Physics. The Scanning Tunneling Microscope has contributed vastly to the development of the nanoscience. To me, this is one of the milestones of nanoscience. The big impact of this technique is due to the ability of Scanning Tunneling Microscope to probe the electronic structure, and a wide range of properties, of different kinds of surfaces with real space atomic resolution. In the last years, Scanning Tunneling Microscope has been established as one of the most powerful techniques for the study of several quantum-physical phenomena at the atomic scale. Also, the Scanning Tunneling Microscope has been used to resolve the internal structure of adsorbed atoms and molecules. In fact, the ability to discriminate between chemically different atoms makes this technique unique compared to others surface analytical techniques [4].

Speaking about the origin of Nanoscience, we should also include the contribution of Eric Dexle in the 80's. Dexle proposed engineering systems at the molecular level, trying to build nanomachines made out of atoms. These nanomachines would be able to construct other molecular components, which would be part of other machines. His basic idea was that if you borrowed ideas from nature, and the scientific advancement permits it, it would possible to build machines that could influence the order of the atoms so precisely as to emulate the biologic evolution process. In 1986, these ideas were collected in his book titled: *"The engines of creation"*, [5] and, as of today, nanomachines and nanotechnology engineering is one of the most active areas in nanoscience. Furthermore and finally, we should mentioned the Nobel Prize given in 1996 to R. F. Curl, H. W. Kroto and R. E. Smalley for fullerenes and carbon nanotubes structure elucidation, [6], and the discovery of the conductive polymers, Nobel Prize 2000, [7]. These were important pieces for a new field to begin to walk, leading to the development of a new science and technology of carbon known as molecular electronics.

As the components size of integrated circuits decreases and the semiconductors industry enters the nanoelectronics real, the principles of classical physics fail as we enter the quantum physics's world. To continue to fulfill Moore's law we must overcome certain limits imposed by the miniaturization of electronic devices. It is essential to control the evolution of the physical properties as quantum confinement emerges with the reduction of dimensionality. Moreover, since the ultimate limit of Moore's Law will be at the level of molecules or atoms, controlling their optical, electrical, and magnetic properties and its assembly capacity and synthesis, will be the only way to continue with this famous law for the next ten, maybe fifteen years.

The molecular and atomic limit gives rise to what today is known as Molecular Electronics. This idea dates back to 1974 when Ari Aviram and Mark

Ratner published an article called *Molecular Rectifiers* in Science magazine, [8]. In this paper, based on the concept of charge transfer between molecules, they discussed the theoretical possibility of building an electronic system which could function as a rectifier diode using organic molecules. The device consisted in three molecular parts: i) a charge acceptor molecule, ii) a molecular group spacer, iii) and another molecule which is able to give electrons. The proposed system would behave as a diode, being the current direction more favorable in one direction than the opposite. The operating principle for this molecular diode is based on the energy difference between the frontier orbitals of the two π-system, acceptor and donor molecules. The spacer molecule is responsible for maintaining the energy difference of the donor-acceptor frontier orbitals, but in turn, allows a certain degree of transport, which has a preferred direction within the device. Molecular electronics considers organic molecules as nanoelectronic devices. These nanodevices are designed under a controlled process of synthesis and self-assembly. Electrical circuits are assembled through processes of self organization and self alignment, drawing on the very nature of molecular systems.

Today, it has been demonstrated the applicability of organic molecules in nanoelectronic devices such as **O**rganic **L**ight-**E**mitting **D**iode (OLED), and **o**rganic **f**ield-**e**ffect **t**ransistor (OFET), and solar cells where charge transfer phenomena are crucial. In the near future, the critical goal to be achieved in molecular electronics is to use molecules as electronic and magnetic switches, wires or components in nanocircuits [9–11]. Moreover, thanks to its magnetic properties and the control that can achieved on them, organic molecules appear as excellent candidates for new materials to advanced technology for memory storage devices.

The study of the spin properties of these systems, either in tandem or as an alternative to the electric charge as an information carrier, is called molecular or organic spintronics. One requirement for spintronic devices is the efficient injection of charge carriers from spin-polarized ferromagnetic electrode or a semiconductor layer. Other requirements for these devices is to have a high-spin relaxation time in order to achieve a good performance. Semiconductors based on organic molecules have been suggested as good candidates in this field due their magnetic properties. The use of magnetic molecules for information technology is also one of the main objectives. **G**iant **M**agneto**R**esistance (GMR) and **T**unnel **M**agneto**R**esistance (TMR) discoveries in metallic spin valves, [12], have revolutionized molecular applications in the field of magnetic recording. The control of the magnetic properties of organic molecules constitute a step towards its application in the growing field of spintronics, which is based on the active manipulation and control of the degree of freedom of electron spin. The success of modern spintronics devices depends crucially on the ability to store and manipulate the electron spin state transport within a properly chosen material. The ability to manipulate electron spin in molecular materials offers a new interesting route, both from fundamental and technological standpoints. This is mainly due to the unquestionable advantage of weak spin-orbit coupling and hyperfine interaction of the electronic states of organic

molecules that are involved in the process of electrical conductivity. This allows for relaxation times of spin, and wave coherence lengths much longer than in conventional metals or semiconductors. The fact that also these materials are optically active makes them also good candidates for magneto optoelectronic devices [13]. The control of these organic devices would allow for non-volatile computer memories with one million times the surface density of bits in the DRAM (**D**ynamic **R**andom **A**ccess **M**emory) and current and power efficiency with a billion times greater than circuits of conventional CMOS (complementary metal-oxide-semiconductor).

Molecular electronics and spintronics can be considered as an advanced reference point when assessing the potential of nanotechnology in the field of digital electronics and computers. The fact that the scale-down of electronic devices can continue with their current exponential rate, described by Moore's law, implies that they will approach molecular dimensions within a decade. In addition, Nanotechnology applications are not limited to the area of computer electronics technology, but cover all imaginable areas in modern society: Communication, medicine, pharmacy, chemistry, physics, environment, sensors, mechanics, fuel, etc. Nanotechnology will not only keep Moore's Law until the end, but also, will serve as an alternative to current technologies, once reached their present limit. Maybe in this context quantum computing will also have something to say in the future.

"Still there is plenty of room at the bottom"

Atomistic electronics.

Ferromagnets are the simplest example in condensed matter physics where the time reversal symmetry is spontaneously broken. Because spins (angular momentum) change sign under time reversal, the spontaneous magnetization in the ferromagnet breaks the symmetry. This is a macroscopic example. We can find this behavior in the nanoscale in magnetic molecules where the molecular spin state is a consequence of the symmetry broken. Nevertheless, the behavior of ferromagnets can dramatically change when we scale down its size and temperature, ferromagnetic nanocontacts are a very good example of that [14]. Low temperature techniques have revealed in last decades the existence of unexpected phenomena such as superconductivity, Kondo effect and topological protected states between others.

The time reversal symmetry plays an important role in all these phenomena. The 3-part of this thesis is focused in the magnetoresistance effect observed in ferromagnetic systems such as Nickel, Iron or Manganese when a polarized tunnel current passes through them. The tunneling magnetoresistance (TMR) is a direct consequence of the absence of time reversal symmetry in these systems. In addition we will to present our result of the effect in the magnetoresistance of an organic molecule such as the Manganese Phthalocyanine (MnPc), a high magnetic spin state molecule, when is deposited on this kind of surfaces.

Actually, it is curious how the electronic properties can change when the spin symmetry is kept or broken. In the part-2 of this thesis we will illustrate that this molecule, the MnPc, can exhibit a Kondo-like resonance, which involves a spin symmetry when it is deposited, at low temperature, on metallic surfaces such as Bismuth or Lead. In this case the MnPc can act as a magnetic impurity on a metal host.

From a theoretical point of view a magnetic impurity is anything that contributes a Curie-weiss term to the magnetic susceptibility; in other words, each localized spin state. When this impurity is deposited or embedded in a metallic host, the impurity can be imagine such a charge excess which it should be screened by the metal to avoid any macroscopic electric field. This argument was proposed by Friedel in the late 50s. Nevertheless this basic idea is insufficient to explain the minimum in the electrical resistivity of Au observed by de Haas, de Boer and van den Berg in 1934 [15], and the unconventional resistivity behavior of other transition metals known today as Kondo effect.

The behavior of magnetic impurities in metals has posed problems to challenge the condensed matter theorist over the past sixty years. Nowadays there is no a definitive or absolute way to resolve this problem, specially in realistic complex system such as organic molecules. The Hamiltonian of the impurity can be described by a very general Hamiltonian specifying all the N_0 electrons

and their interactions.

$$H = \sum_{i=1}^{N_0} \left[\frac{\mathbf{p}_i^2}{2m} + U(\mathbf{r_i}) + V_{imp}(\mathbf{r_i}) \right] + \frac{1}{2} \sum_{i \neq j}^{N_0} \frac{e^2}{|\mathbf{r}_i - \mathbf{r}_j|} + \sum_{i=1}^{N_0} (\mathbf{r_i}) \mathbf{l}_{ii}. \qquad (1)$$

The three first terms in the above equation are the kinetic energy of the electrons, the periodic potential of the host metal due to the nuclei and the potential due to the nucleus of the impurity respectively. The fourth term is the Coulomb interaction between the electrons, and the last one is a relativistic correction due to the spin-orbit coupling.

A first principles calculation resolution of this equation is very difficult because the strong Coulomb interaction which cannot be treated perturbatively. By the mid sixties, Hohenberg, Kohn and Sham [16, 17] proposed a self-consistent field approach in which the problem is reduced to a single electron moving in some averaged potential of all the other electrons, which has to be determined self-consistently. This is the beginning of the well-known today **D**ensity **F**unctional **T**heory (DFT). According to the DFT theory, the ground state properties can be calculated exactly, in principle, since its energy is a universal functional of the electron density. The problem is that the functional is non-local and is no known exactly. Hence, at the end, the Hamiltonian is solved using different kind of local and non-local functional approximation which we will describe in the part-1 of this thesis. Also in this part of the thesis we will to describe different technical aspects of the Green's Function formalism to the transport problem, and the partition and operator theory used and developed as a part of this thesis.

It is well-known that the local approximation to the functional does not work well with strong correlated system, due to the self-interaction problem. The spurious interaction of an electron with itself is not canceled because the exact exchange potential is unknown and the Coulomb interactions are not well compensated. In addition, to solve the Kondo problem, we shall be more interested in the behavior of the system as a function of temperature and in the response to dynamic probes such as the excitation spectrum of the system, rather than ground state properties. Because all these problem, the Kondo effect has been historically studied via simpler model Hamiltonians.

As experiments in nanoelectronics[18] or molecular electronics[19] become more sophisticated, being able to reveal physical phenomena in unprecedented detail, the need for an improvement of the theoretical description of the electronic structure of the studied systems is more and more pressing. Fortunately, on many occasions, one can readily identify an *active* region, i.e., a region in space where the relevant physics takes place and which may be the only one needed of a sophisticated theoretical treatment. In electronic transport problems the active region is where the largest resistance is located. For instance, when a single molecule is connected by metallic electrodes, the main source of resistance is the molecule itself[19–23]. Another prototypical example of active region is the transition metal (TM) atom at the core of organic molecules

such as Phthalocyanines[24]. When these molecules are adsorbed on metallic surfaces, low-temperature scanning tunnelling spectroscopy usually reveals a Kondo effect associated to the TM atom[25–27].

In last years, different authors have been proposed different approaches to the Kondo problem from first-principles calculations. Notably the work of N. Lorente's team and D. Jacob between others to the Molecular Kondo problem. The more important part of this thesis has been the development of a molecular approach to the Kondo problem from first principles calculations without any parameters. For that, and in collaboration with D. Jacob, we developed a partition technique to reduce the full Hamiltonian in the above equation to an active space which has the full information to the system for the Kondo effect. Then, using a constraint-DFT techniques, we remove the electron-electron interaction to correct it via an exact diagonalization which at the same time is the input of an impurity solver combined with a Dynamical Mean Field Theory (DMFT) which allow us to obtain the excitation spectrum.

This set of approaches, which aims to compute the physical properties of realistic systems and therefore complex, whose starting point is an atomistic calculation such as the DFT calculations, and generally requires a high level of theory, is what is known as atomistic electronics.

Part I

I Part: Theoretical Methods

Chapter 1

Electronic Structure Methods.

In this thesis we have studied realistic systems, whose electronic structure can not be determined either by heuristic approaches or by simple models, but they need a clever mix of both due to the complexity of them.

This chapter summarizes the computational electronic structure methods employed in this thesis. In the first section we introduce basics features of standard density functional theory, largely following the excellent reference. In the second section we introduce the basic kind of density functional. In the third section we introduce the self-interaction problem and the Janak's theorem. Because it is very important in our work in the fourth section we introduce the concept of local basis set. In the fifth section we introduce the general theory of constrained DFT techniques which we will use in this thesis. In the last section we briefly describe the basic aspect of the Dynamical mean field theory used in this thesis and the basic concept of the exact diagonalization techniques.

1.1 Density Functional theory.

To obtain the Hamiltonian of any system, firstly we need to solve the many-body Schrödinger equation:

$$\hat{H}\Psi(\vec{r}_1, ..., \vec{r}_N) = E\Psi(\vec{r}_1, ..., \vec{r}_N) \tag{1.1}$$

Where E is the energy of the ground state.
Nevertheless, solving this equation for something bigger than the hydrogen molecule is basically impossible, so we need approximations. In the present work we have used the density functional theory (DFT) for this purpose.
The DFT is a mean field approach used to investigate the ground state electronic structure of an interacting electron system, where the density is the fundamental variable. The origin of this theory dates to the 1920's when Thomas and Fermi described an independent particles system with electrostatic electron-electron interactions, moving under external potential v_{ext} in terms of the electron density distribution $n(\vec{r})$. [28]

$$\hat{H} = \hat{T} + \hat{V}_{ee} + \sum_{i=1}^{N} \hat{V}_{ext}(\vec{r}_i) \tag{1.2}$$

$\hat{T}$ is the Kinetic energy operator and $\hat{V}_{ee}$ is the electron-electron interaction due to electrostatic energy, and N is the number of electrons. To find the ground state of this system, Thomas and Fermi applied the calculus of variations, writing an energy functional, $E[n]$, where all terms in the Hamiltonian are expressed as a function of the density.

$$E[n] = T[n] + V_{ee}[n] + \int v_{ext}(\vec{r}) n(\vec{r}) d\vec{r} \tag{1.3}$$

Here

$$V_{ee}[n] = \frac{1}{2} \int \frac{n(\vec{r}) n(\vec{r}\,')}{|\vec{r} - \vec{r}\,'|} d\vec{r} d\vec{r}\,' = \frac{1}{2} \int v_{int} n(\vec{r}) d\vec{r} \tag{1.4}$$

Since v_{int} is the internal potential:

$$v_{int} = \int \frac{n(\vec{r}\,')}{|\vec{r} - \vec{r}\,'|} d\vec{r}\,' \tag{1.5}$$

And

$$T[n] = \int t\left[n(\vec{r})\right] d\vec{r} \tag{1.6}$$

To define the kinetic energy in terms of the density is the most complicated part in this approach, because the relationship between this energy and the density distribution is unknown. In the Thomas Fermi Theory, $t[n(\vec{r})]$, is the kinetic energy density for a system of noninteracting electrons with density n. A functional is a mathematical function which depend on other functions; In this case, The functional is a function depending on the electron density function distribution. Using the calculus of variations, is possible to find the extremes of this functional. Thomas and Fermi were interested in obtaining the minimum of this object. Hence, keeping constant the number of electrons, $\int n(\vec{r}) d\vec{r} = N$, and using the Lagrange multipliers method, they minimized this system obtaining the corresponding Euler equation:

$$E[n] - \lambda N = t[n(\vec{r})] + \int \left[v_{int} + v_{ext} - \lambda\right] n(\vec{r}) d\vec{r} \tag{1.7}$$

Here λ is the Lagrange parameter. Setting:

$$\delta \left\{E[n] - \lambda N\right\} = 0 \tag{1.8}$$

The Thomas-Fermi Theory certainly is a rough representation of the exact solution of the many-electron Schrödinger equation, but in terms of the electron

density distribution $n(\vec{r})$. However, although there is no clear connection between the electron density theory and the solution of the Schrödinger equation in terms of the wave function, $\Psi(\vec{r}_1, ..., \vec{r}_N)$, the suggestion that a knowledge of the ground state electron density could determine the system became the starting point of a new theory in the 1960's. In two seminal papers, Hohenberg, Kohn [29] and Sham [17] changed the vision and the application of the computational quantum mechanics. This theory is what we call today Density functional theory (DFT). [30]

1.1.1 The Hohenberg Theorem and Kohn-Sham equations

In 1964 Hohenberg and Kohn developed an exact formal variational principle using an universal functional $F[n(\vec{r})]$, i.e independent of the external potential, where the density, $n(\vec{r})$, was the variable fundamental [30]. The two fundamental theorems of this theory are:

Theorem 1: The external potential $V_{ext}(\vec{r})$ is a unique functional of the electron density $n(\vec{r})$.

This theorem implies that the Hamiltonian and consequently the total ground state energy can be expressed as a functional of the electron density, so then, the equation 1.3 can be written as:

$$E[n] = F[n] + \int V_{ext}(\vec{r}) n(\vec{r}) d\vec{r} \tag{1.9}$$

Theorem 2: The ground state energy can be obtained on variational way. i.e. the electron density $n_0(\vec{r})$, which minimizes the total energy, is the exact ground state density.

This theorem provides a minimization scheme for finding the exact ground state energy and electron density if $F[n(\vec{r})]$ is known. Nevertheless, these theorem do not give any idea on how to derive $F[n(\vec{r})]$. For this reason Kohn and Sham provided a solution to this problem [17]. By applying the variational principle of quantum mechanics, Kohn and Sham derived a set of single electron Schrödinger equations known as the Kohn-Sham equations:

$$\left[-\frac{1}{2}\nabla^2 + V_{eff}(\vec{r}) \right] \psi_i(\vec{r}) = \epsilon_i \psi_i(\vec{r}) \tag{1.10}$$

Where the set of single-electron wave functions must correspond to the electron density: $n(\vec{r}) = \sum_{i=1}^{N} |\phi_i(\vec{r})|^2$. The effective potential $V_{eff}(\vec{r})$ involves the total electrostatic potential and the derivative of the exchange-correlation energy:

$$V_{eff}(\vec{r}) = V_{ext}(\vec{r}) + \int \frac{n(\vec{r'})}{\left| (\vec{r}) - (\vec{r'}) \right|} d(\vec{r'}) + \frac{\partial E_{XC}[n]}{\partial n(\vec{r})} \tag{1.11}$$

In DFT calculation, the Kohn-Sham equations are solved self-consistently. First we choose a trial $n(\vec{r})$ and then we evaluate $V_{eff}(\vec{r})$ and a set $\psi_i(\vec{r})$. Finally a new $n(\vec{r})$ can be found. This is repeated in an iterative way until convergence. The total energy can then be found as:

$$E = \sum_{i=1}^{N} \in_i - V_{ee} + E_{XC}[n] - \int \frac{\partial E_{XC}[n]}{\partial n(\vec{r})} n(\vec{r}) d\vec{r} \tag{1.12}$$

The Kohn-Sham equations are in principle exact. However, in practice the exchange-correlation energy $E_{XC}[n]$ has to be approximated because its exact functional form is unknown.

1.2 Local and non-local density functional approximations.

1.2.1 Local Density Approximation (LDA) and Generalized Gradient Approximation (GGA).

The local density approximation assumes that the exchange and correlation energy can be described in terms of the homogeneous electron gas approximation [31]. The homogeneous electron gas defines a system where the interacting electrons are moving around a positive background, keeping the charge neutrality. The expression for the homogeneous electrons gas exchange energy is known analytically [32]:

$$E_X^{LDA} = \frac{1}{N} \sum_k n_k \Sigma_X (k) \tag{1.13}$$

Where N is the number of electrons, n_k is ..., and $\Sigma_X(k)$ is the electron self energy defined at the Fermi level as:

$$\Sigma_X (k_F) = -\frac{e^2 \, k_F}{\pi} \tag{1.14}$$

k_F is the wave vector at the Fermi energy, $k_F = \frac{1}{a_0 r_s} \left(\frac{9\pi}{4}\right)^{1/3}$, a_0 is the Bohr radius $a_0 = \frac{\hbar^2}{me^2}$, and r_s is the radius of the sphere which encloses one unit of electron charge, $r_s = \left(\frac{3}{4\pi n}\right)^{1/3}$, where n is the density. Normally, the exchange energy of electron gas is expressed in terms of r_s and in atomic units:

$$E_X^{LDA} = -\frac{0.4582}{r_s} \tag{1.15}$$

The correlation energy in the local density approximation is defined by the Wigner formula (in atomic units):

$$E_c = -\frac{0.44}{r_s + 7.8} \tag{1.16}$$

In the local density approximation the effects of the exchange and correlation are local and depend only on the value of the electronic density at a point. This approximation only can be applied in the limit of the low variation of the electronic density. Moreover, the most surprising characteristic of this method are the good results obtained using a very simple approximation based on the jellium model and without evaluate accurately the exchange-correlation hole. One of the disadvantages known to this approximations is the fact that the binding energies tend to be too high.

One improvement of the local density approximation is the Generalized gradient approximation, where gradients of the density are introduced [33].

$$E_{XC}^{GGA}\left[n\left(\vec{r}\right)\right] = \int \epsilon_{XC}\left[n\left(\vec{r}\right), \vec{\nabla} n\left(\vec{r}\right)\right] n\left(\vec{r}\right) d^3r \tag{1.17}$$

It has been found that GGA usually gives a better description of the energetics.

1.2.2 Hartree-Fock approximation and the B3LYP functional

In traditional **H**artree-**F**ock (HF) theory one writes antisymmetrized wave functions [34] of the type:

$$\Phi(\vec{x}_1, \vec{x}_2) = \frac{1}{\sqrt{2}}\left[\chi_i(\vec{x}_1)\chi_j(\vec{x}_2) - \chi_j(\vec{x}_1)\chi_i(\vec{x}_2)\right] \tag{1.18}$$

These antisymmetric wave function can be rewritten as a determinant which is called Slater determinant. For an N-electron system the generalized Slater determinant is:

$$\Phi(\vec{x}_1, \vec{x}_2, ..., \vec{x}_N) = \frac{1}{\sqrt{N!}}\begin{vmatrix} \chi_i(\vec{x}_1) & \chi_j(\vec{x}_1) & \cdots & \chi_k(\vec{x}_1) \\ \chi_i(\vec{x}_2) & \chi_j(\vec{x}_2) & \cdots & \chi_k(\vec{x}_2) \\ \vdots & \vdots & & \vdots \\ \chi_i(\vec{x}_N) & \chi_j(\vec{x}_N) & \cdots & \chi_k(\vec{x}_N) \end{vmatrix} \tag{1.19}$$

An Slater determinant has N electrons occupying N spin orbitals without specifying which electron is in which orbital. The interchange of any two columns of the determinant changes the sign of the determinant. This ensures compliance with the Pauli exclusion principle.

$$|\cdots\chi_m\cdots\chi_n\cdots\rangle = -|\cdots\chi_n\cdots\chi_m\cdots\rangle \tag{1.20}$$

Then, using the variational principle, we can obtain the best Slater wave function, $|\Psi_0\rangle = |\chi_1\chi_2\cdots\chi_N$, which gives the lowest possible energy:

$$E_0 = \langle\Psi_0|H|\Psi_0\rangle \tag{1.21}$$

This minimization process leaves a set of eigenvalue equations, called the Hartree-Fock equation, which determines the optimal spin orbitals.

$$F\chi_i(\vec{x}) = \epsilon_i\chi_i(\vec{x}) \tag{1.22}$$

where F is the Fock operator. The Fock operator can be understood as a Hamiltonian. In this Hamiltonian, the potential is the external potential and the average potential experienced by the ith-electron due to the presence of the other electrons. In the Hartree-Fock method, the many-body electron problem has been replaced by a one-electron problem in which electron-electron interactions are treated in an average way.

Hartree-Fock is a traditional alternative to DFT. Nevertheless, neither of them describes well the energy levels. DFT calculations tend to reduce drastically the energy separation between occupied and virtual energy levels and, in contrast, HF calculations tend to increase excessively this gap. For this reason, a hybrid functional, such as B3LYP, mixing these two methods is commonly used. Hybrid functionals include a mixture of Hartree-Fock exchange with DFT exchange-correlation. The **B**ecke **Three** (B3) Parameter Hybrid Functionals have the form devised by Becke in 1993 [35]:

$$F[n] = AE_X^{Slater} + (1-A)E_X^{HF} + B\Delta E_X^{Becke} + E_C^{VWN} + C\Delta E_C^{non-local}. \tag{1.23}$$

Where A, B, and C are constants determined by Becke. There are several variations of this hybrid functional. B3LYP uses the non-local correlation provided by the LYP (Lee, Yang, Parr) expression [36], and VWN functional (VWN: Vosko, Wilk, and Nusair 1980) for local correlation [31]. Note that since LYP includes both local and non-local terms, the correlation functional used is actually:

$$CE_C^{LYP} + (1-C)E_C^{VWN} \tag{1.24}$$

In other words, VWN is used to provide the excess local correlation required, since LYP contains a local term essentially equivalent to VWN.

1.3 The self-interaction problem

A large number of problems in simple DFT approximations comes from the interaction of an electron with the field it generates, which is known as the self-interaction problem. In the HF equations the exchange term appears in the place of the exchange-correlation potential of KS equations:

$$\left(-\frac{\hbar^2}{2m}\nabla^2 + V_H(\mathbf{r})\right)\psi_i(\mathbf{r}) - e^2\sum_{j\in\sigma}\int\frac{\psi_j(\mathbf{r})\psi_j^*(\mathbf{r}')}{|\mathbf{r}-\mathbf{r}'|}\psi_i(\mathbf{r})d\mathbf{r} =_i \psi_i(\mathbf{r}). \tag{1.25}$$

Consequently, the self-interaction cancels exactly, by construction. Self-interaction mostly affects finite systems, or systems containing localized electrons, while its effect is vanishing for delocalized electronic states in extended systems (solids). In finite systems the presence of self-interaction is reflected in an incorrect long-range behavior of the potential felt by an electron.
Several recipes for "Self-Interaction Correction" (SIC) are known, but their theoretical foundation is not completely convincing and their usage often meets numerical trouble, so their usefulness is still a matter of debate. More advanced functionals (e.g hybrid functionals) seem to perform better in this respect.

1.4 The concept of local Basis set.

The basis functions are a mathematical concept. Generally speaking, a base is an ordered set that generates a given vector space. So, any element of the vector space can be written as a linear combination of basis elements that, at the same time, must be linearly independent from each other. In other words, basis functions are the set of mathematical functions with which we generate our vector space. In quantum mechanics, we want to solve the Schrödinger equation on a complex Hilbert space. With this purpose, we will have to decide whose basis set use to create this space. One way to generate this space is using localized basis. Another is using plane waves. In the ab-initio molecular electronics field is common to use the local basis formalism. The ratio between computational time and result accuracy is better in the local basis codes in relationship with the plane waves codes. Nevertheless, the description of a wave function with plane waves is more accurately than the description of that wave function with local basis because plane waves are a complete basis set.

In the localized basis formalism the wave function associated with a molecular orbital ψ_i is defined as a linear combination of atomic orbitals.

$$\psi_i = \sum_{\mu=1}^{n} C_{\mu i}\phi_\mu \tag{1.26}$$

Where ϕ_μ is the wave function associated with the atomic orbital i. In this approach the atomic orbitals are used as basis functions, assuming that molecular orbitals (ψ_i) can be written as a linear combination of them. $C_{\mu i}$ are the coefficients of the linear combination. Classically, these atomic orbitals have been described as Slater Type Orbitals (STO). To improve the time of the calculation, the shape of these STO functions can be approximated by summing up a number of Gaussian Type Orbitals (GTO):

$$g(\alpha, l, m, n; x, y, z) = Ne^{-\alpha r^2}x^l y^m z^n \tag{1.27}$$

Where N is a normalization constant, α is called the exponent, x, y and z are the Cartesian coordinates and l, m and n are integral exponents at Cartesian coordinates. The sum of exponents at Cartesian coordinates: $L = l + m + n$,

is used analogously to the angular momentum quantum number for atoms to mark functions as s-type, $L = 0$, p-type, $L = 1$ ..., assigning thus atomic orbital to basis functions:

L=0 $\rightarrow$ *s-type;* $l = m = n = 0$

$$s = Ne^{-\alpha r^2}$$

L=1 $\rightarrow$ *p-type;* $l = 1, m = n = 0$ (or another equivalent combination)

$$p_x = Ne^{-\alpha r^2}X$$

$$p_y = Ne^{-\alpha r^2}Y$$

...

Now the basis set is an ensemble of primitive Gaussians. For example, to describe an s-atomic orbital, we can use the following function:

$$\psi_s = -0.13N_1e^{-4.4r^2} + 0.59N_2e^{-0.44r^2} + 0.38N_3e^{0.17r^2} + 0.13N_4e^{0.09r^2}$$

In this case, we have only used one basis function to describe the s-orbital. Nevertheless, it is possible to describe this orbital with more than one basis function as follows:

$$\psi_s = -0.13N_1e^{-4.4r^2} + 0.59N_2e^{-0.44r^2} + 0.38N_3e^{0.17r^2}$$

$$\psi_{s'} = 0.13N_4e^{0.09r^2}$$

Now, the atomic s-orbital is described by two basis functions. This method to increase the number of basis function is called *"the segmentation method"*. Increasing the number of basis functions gives more accurate results, regardless of the concommitant increase in the computational time. Hence, this method really is an easy and useful method to obtain more basis functions based on the same basis set.

In figure 1.1 we have plotted a base convergence curve for a benzene molecule. This study has been performed applying the segmentation method. The chosen functional is BPBE [33] and the basis set for the molecular hydrogen atoms is STO-3G always [37]. The basis set for the carbon is the so called CRENBL

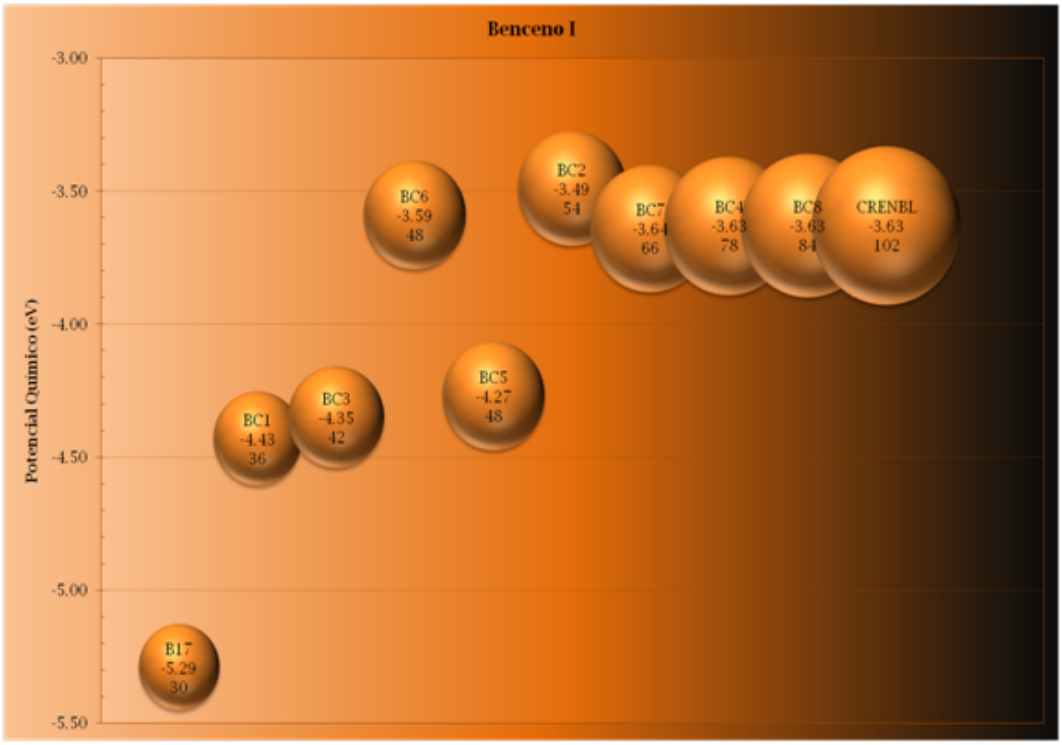

Fig. 1.1: Benzene Convergence Curve based on the CRENBL basis set. In the plot we have represented the chemical potential for this molecule as a function of the number of basis functions.

basis set with different segmentation levels. The computed property in this case is the chemical potential of the molecule. The size of the sphere relates to the number of basis functions, i.e., the bigger the sphere the more basis functions. The figure 1.1 shows that an increase in the number of basis function results in an increase in the chemical potential value until convergence. Also, this plot shows how the choice of a correct segmentation method means a better result. In BC5 and BC6 cases, the number of basis functions is the same. BC5 case segments the s-orbital keeping the p-orbital contracted, while the BC6 case, we segment both, s and p-orbitals. BC6 case is better than BC5 because is always better to extend or to segment more the valence orbital than the core orbitals. And in the carbon atom, strictly speaking, the valence orbital is the p-orbital.

Chapter 2

Quantum transport and ANT.G

2.1 Quantum Tunneling

The Quantum Tunneling refers to the non-zero probability of an electron to be transmitted through a potential barrier whose energy is greater than the electron energy. Quantum tunneling is the quantum mechanical phenomenon in which The Scanning Tunneling Microscopy is based on. In order to introduce basic concepts about the theory of Scanning Tunneling Spectroscopy and Microscopy, we can use an elementary model of one-dimensional tunneling process. Assume that the differential operator, H, of an electron moving along in an one-dimensional potential, $V(x)$ can be written as:

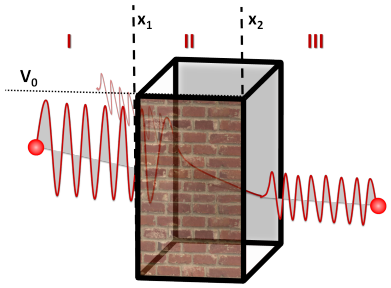

Fig. 2.1: Schematic representation of Quantum Tunnelling. The energy of the tunneled electron is kept constant whereas the probability quantum amplitude decreases through the barrier. $d = x_2 - x_1$. $\psi_n^L(\psi_{n''}^L)$ is the incoming(reflecting) wave function from the left. $\psi_{n'}^R$ is the outgoing wave function to the right

$$H = -\frac{\hbar^2}{2m}\frac{d^2}{dx^2} + V(x) \tag{2.1}$$

where m is the electron mass, $\hbar = h/2\pi$ and h is the Planck's constant. $V(x)$ is a one-dimensional potential which is zero outside the interval $[x_1, x_2]$, but which varies in an arbitrary way inside this interval. In this case, we are going to consider a square potential barrier so that $V(x) = V_0$. Every wave function $\psi(x)$, associated with a stationary state of energy E satisfy the one-dimensional time-independent Schrödinger equation:

$$H\psi(x) = E\psi(x) \quad \rightarrow \quad \left[-\frac{\hbar^2}{2m}\frac{d^2}{dx^2} + V_0\right]\psi(x) = E\psi(x)$$

$$\frac{d^2}{dx^2}\psi(x) + \frac{2m}{\hbar^2}\left[E - V_0\right]\psi(x) = 0 \tag{2.2}$$

We can obtain exactly a solution for this equation in which the wavefunction is defined as a lineal combination of exponential functions of the type $C_n e^{ik_n x}$. C_n are arbitrary complex constants and k_n refers to the momentum of the particle. Hence, for any $E < V_0$ there exists an x-function solution of the form:

$$< V_0 \quad \rightarrow \quad \begin{cases} x < x_1 \rightarrow \psi_I(x) = C_1 e^{ik_1 x} + C_1' e^{-ik_1 x} \\ x_1 < x < x_2 \rightarrow \psi_{II}(x) = C_2 e^{\rho_2 x} + C_2' e^{-\rho_2 x} \\ x > x_2 \rightarrow \psi_{III}(x) = C_3 e^{ik_3 x} + C_3' e^{-ik_3 x} \end{cases} \tag{2.3}$$

where

$$k_n = \frac{\sqrt{2mE}}{\hbar} \qquad \rho_2 = \frac{\sqrt{2m(V_0 - E)}}{\hbar} \tag{2.4}$$

In these solutions $C_n e^{ik_n x}$ represents a wave propagator in a one-way, and $C_n' e^{-ik_n x}$ in the opposite way along the same direction, commonly dubbed propagation and reflexion waves, or incoming and outgoing waves. Boundary conditions require that $C_2, C_3' \rightarrow 0$ at $x \rightarrow \infty$, and $C_1 = 1$. In the barrier the solution of the Schrödinger equation is an evanescent wave which looks like $\psi_{II}(x) = C_2' e^{-\rho_2 x}$. Also boundary conditions require the continuity of wave functions and its derivative at points x_1 and x_2 as shown in figure 2.1.

$$C_1 e^{ik_1 x_1} + C_1' e^{-ik_1 x_1} = C_3 e^{ik_3 x_2} \tag{2.5}$$

$$k_1 \left[C_1 e^{ik_1 x_1} + C_1' e^{-ik_1 x_1} \right] = k_3 \left[C_3 e^{ik_3 x_2} \right] \tag{2.6}$$

Rewriting these equations in a matrix form we can obtain the transmission matrix $\mathbf{M}$:

$$\begin{bmatrix} C_1 \\ C_1' \end{bmatrix} = \overbrace{\begin{bmatrix} M_{11} & M_{12} \\ M_{21} & M_{22} \end{bmatrix}}^{\mathbf{M}} \begin{bmatrix} C_3 \\ 0 \end{bmatrix} \tag{2.7}$$

The boundary conditions showing in equations 2.5 and 2.6 are the elastic scattering condition. Elastic transport means that the energy of the particle-wave is kept constant along the tunneling process, i.e. the process is phase coherent.

Quantum mechanics establishes that the wave particle probability density, $\omega(t, \vec{r})$ is equal to $\omega(t, \vec{r}) = \psi(t, \vec{r})\psi^*(t, \vec{r})$. The Schrödinger equations for both wave functions, $\psi(t, \vec{r})$ and it complex conjugate, $\psi^*(t, \vec{r})$ is written:

$$i\hbar \frac{\partial}{\partial t}\psi(t, \vec{r}) = -\frac{\hbar^2}{2m}\Delta\psi(t, \vec{r}) + V(t, \vec{r})\psi(t, \vec{r})$$

$$-i\hbar \frac{\partial}{\partial t}\psi^*(t, \vec{r}) = -\frac{\hbar^2}{2m}\Delta\psi^*(t, \vec{r}) + V(t, \vec{r})\psi^*(t, \vec{r})$$

Multiplying by $-\psi(t, \vec{r})$ or $\psi^*(t, \vec{r})$ as appropriate, and adding both equations:

$$i\hbar \frac{\partial}{\partial t}\left[\psi^*(t, \vec{r})\psi(t, \vec{r})\right] = -\frac{\hbar^2}{2m}\left[\psi^*(t, \vec{r})\Delta\psi(t, \vec{r}) - \psi(t, \vec{r})\Delta\psi^*(t, \vec{r})\right]$$

And assuming the local conservation of probability, i.e:

$$\frac{\partial}{\partial t}\omega(t,\vec{r}) + \nabla\vec{\mathbf{j}}(t,\vec{r}) = 0 \tag{2.8}$$

We can obtain the so called quantum probability density current, $\vec{\mathbf{j}}(t,\vec{r})$:

$$\vec{\mathbf{j}}(t,\vec{r}) = \frac{\hbar^2}{2mi}\left[\psi^*(t,\vec{r})\nabla\psi(t,\vec{r}) - \psi(t,\vec{r})\nabla\psi^*(t,\vec{r})\right] \tag{2.9}$$

Probabilities currents associated with the incoming and outgoing waves are, in our one-dimensional case:

$$j_{in}(x_1) = \frac{\hbar k}{m}\left|C_1\right|^2 \qquad j_{out}(x_2) = \frac{\hbar k}{m}\left|C_3\right|^2 \tag{2.10}$$

These equations demonstrate that the probability current associated with a wave-particle can be express in terms of probability density, which is uniform throughout all space and independent on time.
The transmission coefficient $T(E)$, is the ratio of the incoming and the outgoing currents in the point x_2:

$$T(E) = \frac{j_{out}(x_2)}{j_{in}(x_1)} = \left|\frac{C_3}{C_1}\right|^2 \tag{2.11}$$

In the same way, the reflexion coefficient $R(E)$, is the ratio of the incoming and the outgoing currents in the point x_1:

$$R(E) = \frac{j_{out}(x_1)}{j_{in}(x_1)} = \left|\frac{C_1'}{C_1}\right|^2 \tag{2.12}$$

In a classical system, if $E < V_0$, one would expect that the particle does not pass through the barrier, and therefore, the wave-particle transmission probability (T), was zero ($T = 0$); However, in a quantum system there is any probability of that the electron-wave passes through the potential barrier. We can rewrite the equation 2.10 in terms of the elements of the transmission matrix defined in equation 2.7, taking into account that $C_1 = M_{11}C_3$:

$$j_{in}(x_1) = \frac{\hbar k}{m}\left|C_1\right|^2 = \frac{1}{\left|M_{11}\right|^2} \tag{2.13}$$

$$M_{11} = \left[cosh\left(2\rho_2 a\right) - \frac{i}{2}\left(\frac{k^2-\rho^2}{k\rho_2}\right) sinh(2\rho_2 a)\right] e^{2ika} \tag{2.14}$$

Where $a = d/2$ and we have taken $k_1 = k_2 = k$. Now the transmission coefficient can be written as:

$$T(E) = \left|\frac{C_3}{C_1}\right|^2 = \left|\frac{C_3}{M_{11}C_3}\right|^2 = \left|\frac{1}{M_{11}}\right|^2 =$$

$$= \left[cosh^2(2\rho_2 a) - \frac{i}{2}\left(\frac{k^2-\rho^2}{k\rho_2}\right)^2 sinh^2(2\rho_2 a) \right]^{-1} =$$

$$= \frac{1}{1+\left(\frac{k^2+\rho_2^2}{2\rho_2 k}\right)^2 sinh^2(2\rho_2 a)} \tag{2.15}$$

If we considerer the tunneling limit, where $2\rho_2 a >> 1$ the transmission coefficient can be approximated as an exponential decay such as we have illustrated in figure 2.1 into the barrier:

$$T(E) \approx \left(\frac{2\rho_2 k}{k^2+\rho_2^2}\right)^2 e^{-4\rho_2 a} \tag{2.16}$$

To explain this effect we may recur to the Heisenberg uncertainty principle:

$$\Delta E \Delta t \approx \hbar \qquad \Delta p_x \Delta x \approx \hbar \tag{2.17}$$

Due the uncertainty, the electron energy can be represented by a normal distribution function. At given time, the energy of electron can take any value defined in this distribution function with more or less probability.

If an electron goes to the potential barrier with energy, $E \pm \delta E$, in such a way that $E < V_0$, the transmission probability is proportional to the probability of what electron has the barrier energy. Thus, while $V_0 \in [E \pm \delta E]$ is fulfilled, there will be a non-zero probability of what the electron is transmitted despite the potential barrier and leading to tunneling process. Also, the Heisenberg uncertainty principle can also be written as $\Delta p_x \Delta x \approx \hbar$. So, there is some uncertainty in the electron position. If the thickness of the barrier, $d = x_2 - x_1$ is inside of this uncertainty, i.e. $d \in [x \pm \Delta x]$, the wave function will have some probability to cross the barrier before to vanish, resulting in a tunneling process.

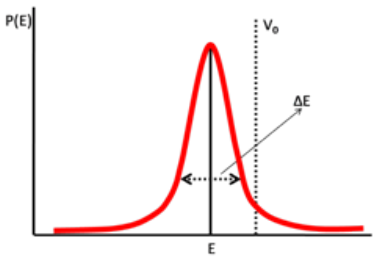

Fig. 2.2: Energy Distribution Function showing the broadening of a energy level due to the Heisenberg uncertainty principle

2.2 From Bardeen to Landauer Formalism.

We are going to consider a simple tip-vacuum-surface junction based on the unidimensional potential model explained in the last section. The vacuum plays the role of the potential barrier height V_0. If we assume that the tip-surface difference in work functions is small, we may suppose a square potential barrier developed between the tip and the surface, neglecting the thermal excitation of electrons in the metal. The electron can tunnel from the tip to the surface and vice versa. By applying a bias voltage, V, a net tunneling current occurs and we end up with a model like figure 2.3.

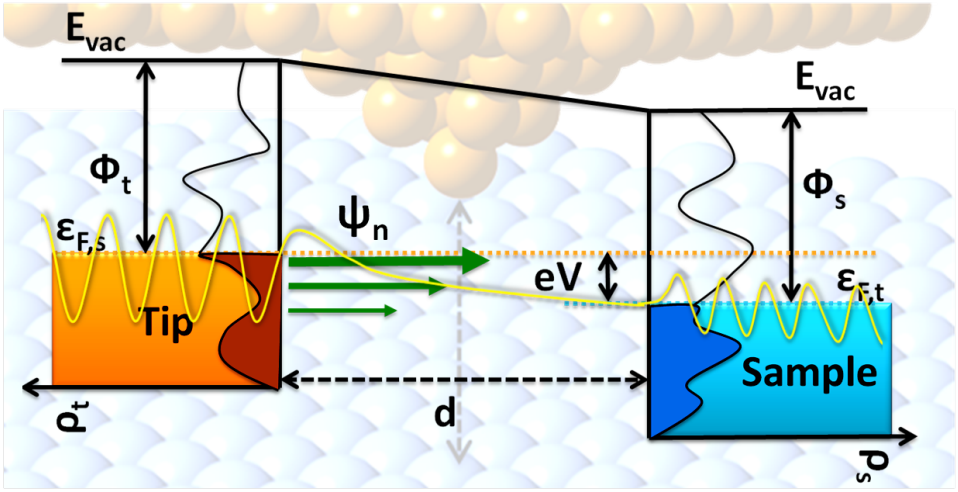

Fig. 2.3: Schematic one-dimensional energy diagram for a sample-tip tunnel junction with a width d. In this representation a positive bias voltage has been applied to the sample, and electrons therefore tunnel from occupied tip states into empty sample states. Occupied states in the tip/sample are darkened and the size of horizontal arrows indicates different tunneling probabilities for electron of different energies. Tunneling is only permitted within the small energy interval eV. $\Phi_s(\Phi_t)$ is the work function of the sample(tip). The density of states of the sample(tip), $\rho_s(\rho_t)$, has been sketched. Ψ_n illustrates a wave function with energy ϵ_n that decays exponentially in the junction but still has a non-zero amplitude at the position of the sample. ψ_n^t is the incoming n-state wave function from the tip, and $\psi_m^s(\psi_{n'}^t)$ is the transmitted(reflected) wave functions to the $m(n')$-state of the sample(tip). E_{vac} is the vacuum energy, and $\epsilon_{F,t(s)}$ is the Fermi energy of the tip(sample).

There is a finite probability for a tip wave function, ψ_n, with an energy ϵ_n, between ϵ_F and $\epsilon_F - eV$, to tunnel to an empty state in the sample. If we assume that the potential barrier weight is equal to the average work function $\overline{\Phi} = (\Phi_s + \Phi_t)/2$, taking into account the applied bias, then $V_0 - \epsilon_n \approx \overline{\Phi} - \epsilon_n + (eV/2)$. Using the solution obtained in equation 2.4 we can obtain the tunnel probability as:

$$\omega(d,t) = |\psi_n(0,t)|^2 \, e^{-2\rho d} = |\psi_n(0,t)|^2 \, e^{-2d\sqrt{\frac{2m}{\hbar^2}\left(\overline{\Phi}+\frac{eV}{2}-\epsilon_n\right)}} \tag{2.18}$$

Where

$$T(\epsilon_n, d, V) = e^{-2d\sqrt{\frac{2m}{\hbar^2}\left(\overline{\Phi}+\frac{eV}{2}-\epsilon_n\right)}} \tag{2.19}$$

is the tunneling transmission probability for a trapezoidal barrier [38, 39] normally used in scanning tunneling spectroscopy (STS). Nevertheless, to evaluate the tunneling current in a general situation Bardeen proposed a perturbative method [40], where the tunneling current is viewed as the net effect of many independent scattering events that transfer electrons across the tunneling barrier. (The three wave functions draw in figure 2.3). In order to estimate the tunneling current through the tip-sample junction, Bardeen proposed to evaluate the tip and the sample separately. The isolated tip and surface Hamiltonian are [41, 42]:

$$H_s = -\frac{\hbar^2}{2m}\nabla^2 + \Phi_s \tag{2.20}$$

$$H_t = -\frac{\hbar^2}{2m}\nabla^2 + \Phi_t \tag{2.21}$$

where $t(s)$ is relative to the tip(surface). Instead of trying to solve the combined problem, Bardeen showed that electronic wave functions of the separate sample and tip subsystems (Φ_s and Φ_t, respectively) can be obtained by solving the stationary Schrödinger equation. The rate of electron transfer, that is, the tunnel current, can then be calculated by time-dependent perturbation theory. Assume us that the subindex α is relative to the perturbed system, then:

$$H_\alpha = -\frac{\hbar^2}{2m}\nabla^2 + V_\alpha\left(\vec{r}\right) \tag{2.22}$$

Since the electron is destroyed in the tip and generated on the surface, the electron wavefunction as a function of time can be written as:

$$\psi_\alpha(\vec{r},t) = \psi_n e^{-it\epsilon_n/\hbar} + \sum_s a_s(t)\phi_s \tag{2.23}$$

In the opposite case, i.e. an electron that is destroyed in the surface and generated in the tip, the electron wavefunction is:

$$\psi_\alpha(\vec{r},t) = \psi_s e^{-it\epsilon_s/\hbar} + \sum_n a_n(t)\phi_n \tag{2.24}$$

Now the real goal is to obtain the a_s and a_n coefficients using perturbation theory, but this is beyond the scope of this work. Bardeen showed that the tunneling matrix element, M_{mn}, is determined by the overlap of the surface wave functions of the two systems separated $d\mathring{A}$ and can be expressed as:

$$M_{mn} = -\frac{\hbar^2}{2m}\int_d (\psi_n^*\nabla\psi_m - \psi_m\nabla\psi_n^*)dS \tag{2.25}$$

where the integral is calculated over a surface lying in the vacuum region between the tip and surface. Later, Tersoff and hamann [43, 44], among other [42, 45–48] developed different ways to calculate Bardeen's matrix. In the Tersoff-Hamann approximation, the solution of the Schrödinger equation for a spherical potential were taken as tip wave functions, assuming that only the s-wave solution was important. At low voltages, eV is small enough so that the density of electronic states does not vary significantly at Fermi level, hence the tunneling current is proportional to the Fermi local density of states (LDOS) at the center of curvature of the tip. Hence, Tersoff-Hamann using the so-called s-wave approximation and the Bardeen matrix, obtained the probability, ω, of an electron to tunnel between a tip state ψ_m, and a sample state, ψ_n. A well known result from first-order time-dependent perturbation theory is Fermi's golden rule, which states that the transition rate for an electron to tunnel from an initial (tip) state, ψ_m, to a final (sample) state, ψ_n, is given by:

$$\omega_{m\to n} = \frac{2\pi}{\hbar}\sum_n |M_{mn}|^2\delta(E_m - E_n) \tag{2.26}$$

Where the delta function indicates that only elastic tunneling is considered, that is tunneling between states with the same energy at both sides of the gap. With Fermis golden rule in mind, the tunnel current from the tip to the sample, for a system with positive bias voltage, eV, on the sample, can be written as:

$$I_{t\to s} = \frac{4\pi e}{\hbar}\int_{-\infty}^{\infty} \rho_t(\epsilon) f(\epsilon) T(\epsilon) \rho_s(\epsilon + eV)\,[1 - f(\epsilon + eV)]\,d\epsilon \tag{2.27}$$

where the factor of 2 in front accounts for electron spin. $f(\epsilon) = [1 + Exp((\epsilon - \epsilon_F)/K_bT)]^{-1}$ is the Fermi distribution function of the electrons at temperature T and K_b is the Boltzmann's constant. $\rho_s(\rho_t)$ is the local density of states of the sample(tip). Since $K_bT < \Delta\epsilon$ and the Fermi function can be approximated by a step function, and since a small bias voltage is applied, the tunneling current can be calculate by summing over all the possible states:

$$I_{t\to s} \approx \frac{4\pi e}{\hbar}\int_{0}^{eV} [\rho_t(\epsilon_F - eV + \epsilon) T(\epsilon) \rho_s(\epsilon_F + \epsilon)]\,d\epsilon \tag{2.28}$$

This equation shows the tunneling current as the tip-surface convolution of the density of states. If the tunneling matrix element does not change appreciably as a function of energy, it can be separated out in which case the tunnel current can be expressed as a convolution of the surface and tip DOS. There are several approximation to obtain, first this LDOS, and second to obtain the Bardeen matrix. In this work, we have consider the Bardeen matrix as the tip-surface hopping matrix, and we have obtained it using Density Functional Theory (DFT) calculations.

Since

$$I = GV \;\rightarrow\; \frac{dI}{dV} = G \;\rightarrow\; I = \int G dV$$

$$E = qV \;\rightarrow\; \frac{dE}{dV} = q \;\rightarrow\; dV = \frac{dE}{q}$$

$$I = \int G dV \;\rightarrow\; I = \frac{1}{e}\int G dE$$

Where V is the voltage, G the conductance, E de energy, q the electron charge (e), and I the current. The conductance is:

$$G = \frac{e^2}{h}\sum_{nm} [\rho_m(\epsilon_F)\, M_{nm}\, \rho_n(\epsilon_F + eV)\, M^*_{nm}] \tag{2.29}$$

If we consider the ψ_m and ψ_n coupling states as a highway for which the electron can pass or cannot pass depending on the value of this coupling, we can

treat this states as orbital, in the local orbital basis formalism, or conduction channel, [46]. So, a bias zero, the tunnel conductance at Fermi level is related here to the product of the orbital-resolved LDOS of the electrodes. Notice that this result seems the conductance equation obtained by D. Jacob et.al. [49] using the Green's Functions formalism and the Landauer formula:

$$G = \frac{e^2}{h} T(\epsilon_F) = \frac{e^2}{h} \sum_n T_n (2.30)$$

Where T_n is the transmission functions writing as a function of the eigenchannel, n. In the Green's function formalism, we can obtain the transmission matrix from the Caroli's equation, [50].

$$T(E) = Tr \left[\hat{G}_c(E) \hat{\Gamma}_t(E) \hat{G}_c^+(E) \, \hat{\Gamma}_s(E) \right] \quad (2.31)$$

Where $\hat{G}_c(E)$ refers to the central region between electrodes and $\hat{\Gamma}_t(E)(\hat{\Gamma}_s(E))$ refers to the coupling matrix of the tip(sample) electrode. This is the Modus operandi of ALACANT code. [51] Aqui iría como se va del one-electron al many body en términos de transporte.

Chapter 3

The partition Methods.

The partition of the Hamiltonian of systems consisting of several parts of different nature and different physical relevance is particularly necessary when correlations are important in some of these parts and standard density functional theory (DFT) approximations do not capture the relevant physics there. DFT implementations as those found in commonly used codes[52, 53] usually make no distinction in the treatment of the different parts of a physical system (DFT+U corrections, being an exception). As regards the previous examples, an accurate calculation of the electronic structure of the contacted molecule is imperative, in particular of the HOMO-LUMO gap which is not correctly given by standard DFT approximations[54–58]. On the contrary, the electronic structure deep into the bulk electrodes, which are typically free-electron metals, needs little attention and even simple tight-binding models can account for it[22, 59, 60]. Following with the second example, in order to properly describe the Kondo effect electronic correlations need to be taken into consideration at the TM atom (for instance through DFT+DMFT schemes[27]) while the electronic structure of the organic ligands and substrate can be safely described by standard DFT.
In this regard one first needs to obtain an effective description of the active part. In other words, one looks for a non-Hermitian energy-dependent “Hamiltonian" which includes the effect of the rest of the system. Once this effective Hamiltonian has been obtained, one can try to improve the electronic description or add the necessary terms to it to account for the required physics. However, a preliminary step, with mathematical pitfalls easy to overlook, needs to be taken first. This step consists of finding a precise mathematical definition of the active region itself. This is done, in principle, through the selection of a subset of basis elements that expand the vector subspace associated to such region. For practical purposes many implementations of DFT make use of non-orthogonal basis sets (typically atomic orbitals) which makes this selection problematic due to the inherent ambiguity accompanying these subsets. In other words, the vector subspace expanded by a non-orthogonal basis subset is not orthogonal to the rest of the system from which we want it unambiguously separated.
An important effort to address these issues has been made with the development of Wannier functions [61–66] or localized molecular orbitals [67, 68]. While constructing orthogonal basis sets is a successful approach,

here we take an alternative route which does not require finding new basis sets. Instead, we show in detail how to address the partitioning problem while keeping the use of the original non-orthogonal basis sets on which the DFT code of interest is based on. Partitioning techniques usually rely on Green's functions formalism. We show here how to obtain effective Hamiltonians from reduced Green's functions by proper projection and reversal engineering operations in a general non-orthogonal metric. We calculate the projected or local density of states (LDOS) and projected or local charge in simple examples to illustrate the differences and the arbitrariness inherent to different ways of performing the *a priori* same physical partition. The conductance, instead, does not depend on the type of projection, as long as this removes parts of the electrodes which are sufficiently far away from each other. We also discuss, for completeness, the use of mixed basis set where direct and dual subspaces are employed[69].
While this work is mainly motivated by problems where standard DFT fails, the partitioning technique presented here can also be used in a variety of other situations such as constrained DFT methodologies[70–72] or when rigorous population analysis are needed. Some of the mathematical and conceptual issues discussed here have been previously addressed in the literature [73–81], but we believe that our approach to the problem may shed a new light on some of the unresolved or controversial points. We begin by revisiting some basic operator operations in a non-orthogonal metric in Sec. 3.1. In Sec. 3.2 we discuss the dual basis and its relevance to the inversion operation. Section 3.3 presents the essential definitions of projectors along with the different projections that can be carried out and in Sec. 3.4 the concept of non-integer dimension of a subspace is introduced. Section 3.5 revisits the block-orthogonal metrics introduced by Thygesen [69] along with the appropriate basis change transformations. In Sec. 3.6 we show how different projections of the Green's function give rise to different definitions of the local density of states (LDOS) and associated integrated charges, the popular Mulliken charges being one of them. In Sec. 3.7 we show how to carry out reversal engineering procedures to obtain effective Hamiltonians from the projected Green's function and, finally, in Sec. 3.8 we show how the conductance can be evaluated starting from any type of projection, being the result independent on the chosen one. A brief set of conclusions is presented at the end.

3.1 Operators in an arbitrary metric

We consider a vector space expanded by a finite and not necessarily orthogonal basis set $\{|i\rangle\}$ of dimension N. The inner product of its elements $\langle i|j\rangle = S_{ij}$ constitutes the overlap matrix, also called the *metric* of such basis set. We will assume, for simplicity, $\{|i\rangle\}$ to be real and normalized ($\langle i|i\rangle = 1 \; \forall \, i$) so that $\mathbf{S}$ is real symmetric. For the particular case of an orthogonal basis set the overlap matrix becomes the identity matrix $S_{ij} = \delta_{ij}$. The identity operator in terms of this generic basis set is given by the completeness (or closure) relation:

$$\hat{\mathbf{I}} = \sum_{ij} |i\rangle \, S^{-1}_{ij} \, \langle j|. \tag{3.1}$$

The representation of the identity operator in the basis set defining the metric is the overlap matrix itself, $\langle m|\,\hat{\mathbf{I}}\,|n\rangle = S_{mn} \equiv (\mathbf{S})_{mn}$. For simplicity, we will write S^{-1}_{ij} instead of the less ambiguous expression $(\mathbf{S}^{-1})_{ij}$ for the elements of the inverse matrix. (Unless deemed necessary, this will apply to any matrix inversion from now on).
In general, any one-body operator $\hat{\mathbf{A}}$ can be written or expressed in terms of the basis set defining the metric:

$$\hat{\mathbf{A}} = \sum_{ij} |i\rangle\, \tilde{A}_{ij}\, \langle j|, \tag{3.2}$$

where $\tilde{\mathbf{A}} = \mathbf{S^{-1}AS^{-1}}$ is the "nucleus" or "nuclear" matrix of the operator. One can easily obtain the matrix elements of the operator from the previous expression:

$$\begin{aligned}\langle m|\,\hat{\mathbf{A}}\,|n\rangle =& \sum_{ij} \langle m|i\rangle\, \tilde{A}_{ij}\, \langle j|n\rangle = \\ & \sum_{ij} S_{mi}\tilde{A}_{ij}S_{jn} = A_{mn}.\end{aligned} \tag{3.3}$$

Based on the generalized expression for an operator introduced in Eq. 3.2 one can check a basic property for the identity operator:

$$\begin{aligned}\hat{\mathbf{I}}\hat{\mathbf{A}} =& \sum_{ijkl} |i\rangle\, S^{-1}_{ij}\, \langle j|k\rangle\, \tilde{A}_{kl}\, \langle l| = \sum_{ijkl} |i\rangle\, S^{-1}_{ij} S_{jk}\tilde{A}_{kl}\, \langle l| = \\ & \sum_{ikl} |i\rangle\, \delta_{ik}\tilde{A}_{kl}\, \langle l| = \sum_{il} |i\rangle\, \tilde{A}_{il}\, \langle l| = \hat{\mathbf{A}}.\end{aligned} \tag{3.4}$$

More interesting is the following result for the product of two operators [73]:

$$\hat{\mathbf{B}}\hat{\mathbf{A}} = \sum_{ijkl} |i\rangle\, \tilde{B}_{ij}\, \langle j|k\rangle\, \tilde{A}_{kl}\, \langle l| = \sum_{ijkl} |i\rangle\, \tilde{B}_{ij} S_{jk}\tilde{A}_{kl}\, \langle l|, \tag{3.5}$$

expression from which the matrix elements of the product can be easily obtained

$$\begin{aligned}\langle m|\,\hat{\mathbf{B}}\hat{\mathbf{A}}\,|n\rangle =& \sum_{ijkl} \langle m|i\rangle\, \tilde{B}_{il}\, \langle l|k\rangle\, \tilde{A}_{kj}\, \langle j|n\rangle = \\ & \sum_{ijkl} S_{mi}\tilde{B}_{il}S_{lk}\tilde{A}_{kj}S_{jn} = \left(\mathbf{BS^{-1}A}\right)_{mn}.\end{aligned} \tag{3.6}$$

This result can be easily overlooked. In a general metric the product of operators is not simply the product of their matrix representations.

3.2 The dual basis

Given a general basis set with a metric $\mathbf{S}$ (hereon called the *direct* basis set), there exists a basis set *dual* to this with the property $\langle i|j^*\rangle = \delta_{ij}$. Only for

orthogonal basis sets both direct and dual sets coincide. In general, the nuclear matrix of any operator, $\tilde{\mathbf{A}}$, is the dual representation of this operator:

$$\langle k^*| \hat{\mathbf{A}} |l^*\rangle = \langle k^*| \left(\sum_{ij} |i\rangle \tilde{A}_{ij} \langle j| \right) |l^*\rangle = \tilde{A}_{kl}. \tag{3.7}$$

One can equally write or express any operator in terms of the dual basis set:

$$\hat{\mathbf{A}} = \sum_{ij} |i^*\rangle A_{ij} \langle j^*|, \tag{3.8}$$

where now the nuclear matrix is the representation of the operator in the direct basis itself $\mathbf{A}$. This can be easily proved by direct computation of the matrix elements or by noting that

$$|i\rangle = \sum_{j} S_{ij} |j^*\rangle , \tag{3.9}$$

or equivalently

$$|i^*\rangle = \sum_{j} S^{-1}_{ij} |j\rangle . \tag{3.10}$$

As an example, the identity operator can also be written as

$$\hat{\mathbf{I}} = \sum_{ij} |i^*\rangle S_{ij} \langle j^*| \tag{3.11}$$

and, for later use, one can also write the identity operator in the following "orthogonal" form:

$$\hat{\mathbf{I}} = \sum_{i} |i^*\rangle \langle i| = \sum_{i} |i\rangle \langle i^*|. \tag{3.12}$$

An interesting use of the dual basis concerns the inversion of an operator. The inversion operation consists of the inversion of the nuclear matrix along with the "dualization" of the basis in which this operator is written:

$$\hat{\mathbf{A}}^{-1} = \left[\sum_{ij} |i\rangle \tilde{A}_{ij} \langle j| \right]^{-1} = \sum_{ij} |j^*\rangle \tilde{A}^{-1}_{ji} \langle i^*|. \tag{3.13}$$

The validity of this expression can easily be checked by direct verification of $\hat{\mathbf{A}}^{-1}\hat{\mathbf{A}} = \hat{\mathbf{I}}$. The resulting matrix elements of the inverse operator thus become

$$\begin{aligned} \langle m| \hat{\mathbf{A}}^{-1} |n\rangle = & \sum_{ij} \langle m|j^*\rangle \tilde{A}^{-1}_{ji} \langle i^*|n\rangle = \\ & \sum_{ij} \delta_{mj} \tilde{A}^{-1}_{ji} \delta_{in} = \tilde{A}^{-1}_{mn}. \end{aligned} \tag{3.14}$$

Note that the inversion of an operator does not correspond to the inversion of its matrix representation, but to the inversion of its nuclear matrix.

3.3 Projection Operators: Basic considerations

For future use we now establish the basics concerning projection operations. We begin by considering in this section the expression of the operator for the projection onto a one-dimensional vector subspace expanded by a single element $|i\rangle$ of the direct basis set. Taking into account the definition of the identity operator in Eq. 3.1, it follows

$$\hat{\mathbf{P}}_i = \sum_j |i\rangle\, S_{ij}^{-1}\, \langle j| = |i\rangle\, \langle i^*| = \sum_j |j^*\rangle\, S_{ji}\, \langle i^*|, \tag{3.15}$$

where we have used the transformation between direct and dual basis, given in Eqs. 3.9 and 3.10, to obtain the three equivalent expressions. With a non-orthogonal basis set one can also write the adjoint of the previous operator:

$$\hat{\mathbf{P}}_i^\dagger = \sum_j |j\rangle\, S_{ji}^{-1}\, \langle i| = |i^*\rangle\, \langle i| = \sum_j |i^*\rangle\, S_{ij}\, \langle j^*|. \tag{3.16}$$

It is easy to show with the help of a generic element of the basis set, $|k\rangle$, that the projector operator is non-Hermitian by comparing

$$\hat{\mathbf{P}}_i\, |k\rangle = \sum_j |i\rangle\, S_{ij}^{-1}\, \langle j|k\rangle = \delta_{ik}\, |i\rangle \tag{3.17}$$

with

$$\langle k|\, \hat{\mathbf{P}}_i = \sum_j \langle k|i\rangle\, S_{ij}^{-1}\, \langle j| = \langle i^*|\, S_{ik}, \tag{3.18}$$

which are obviously not the dual of each other. The Hermitian-adjoint projector behaves similarly:

$$\langle k|\, \hat{\mathbf{P}}_i^\dagger = \sum_j \langle k|j\rangle\, S_{ji}^{-1}\, \langle i| = \langle i|\, \delta_{ik} \tag{3.19}$$

and

$$\hat{\mathbf{P}}_i^\dagger\, |k\rangle = \sum_j |j\rangle\, S_{ji}^{-1}\, \langle i|k\rangle = S_{ik}\, |i^*\rangle \tag{3.20}$$

are not dual of each other either. This result has important implications when we intend to project a generic operator $\hat{\mathbf{A}}$ onto the mono-dimensional vector subspace expanded by $|i\rangle$. One can perform what we call a Hermitian projection using both projectors (Eq. 3.15 and 3.16):

$$\begin{aligned} \hat{\mathbf{A}}_i \equiv & \hat{\mathbf{P}}_i^\dagger \hat{\mathbf{A}} \hat{\mathbf{P}}_i = \sum_{kl} |i^*\rangle\, \langle i|k\rangle\, \tilde{A}_{kl}\, \langle l|i\rangle\, \langle i^*| = \\ & |i^*\rangle\, A_{ii}\, \langle i^*|\,. \end{aligned} \tag{3.21}$$

Representing the resulting operator in the direct basis element one obtains

$$\langle i|\, \hat{\mathbf{P}}_i^\dagger \hat{\mathbf{A}} \hat{\mathbf{P}}_i\, |i\rangle = \langle i|i^*\rangle\, A_{ii}\, \langle i^*|i\rangle = A_{ii}. \tag{3.22}$$

This projection has taken us onto the corresponding subspace expanded by the dual basis element which gives the matrix element A_{ii} as the representation

in the direct basis element. There is an obvious alternative way of performing the above projection operation:

$$\begin{aligned}\hat{\mathbf{A}}_i^* \equiv &\hat{\mathbf{P}}_i\hat{\mathbf{A}}\hat{\mathbf{P}}_i^\dagger = \sum_{jklm} |i\rangle \langle i^*|k\rangle \tilde{A}_{kl} \langle l|i^*\rangle \langle i| = \\ &\sum_{klm} |i\rangle \delta_{ik}\tilde{A}_{kl}\delta_{li} \langle i| = |i\rangle \tilde{A}_{ii} \langle i| .\end{aligned} \tag{3.23}$$

Representing the resulting operator on the direct basis element one obtains

$$\langle i| \hat{\mathbf{P}}_i\hat{\mathbf{A}}\hat{\mathbf{P}}_i^\dagger |i\rangle = \langle i|i\rangle \tilde{A}_{ii} \langle i|i\rangle = \tilde{A}_{ii}. \tag{3.24}$$

Notice that the representation of this projection gives the corresponding element of the nuclear matrix and not of the matrix representation of the operator, A_{ii}. We call this a *dual* projection as opposed to the previous *direct* projection.
For future reference note that one can perform a non-Hermitian projection as

$$\begin{aligned}&\hat{\mathbf{P}}_i\hat{\mathbf{A}}\hat{\mathbf{P}}_i = \sum_{kl} |i\rangle \langle i^*|k\rangle \tilde{A}_{kl} \langle l|i\rangle \langle i^*| = \\ &\sum_{klm} |i\rangle \delta_{ik}\tilde{A}_{kl}S_{li}S^{-1}_{im} \langle m| = \sum_{lm} |i\rangle \tilde{A}_{il}S_{li}S^{-1}_{im} \langle m|,\end{aligned} \tag{3.25}$$

from which, when represented on the mono-dimensional direct subspace, one obtains

$$\langle i| \hat{\mathbf{P}}_i\hat{\mathbf{A}}\hat{\mathbf{P}}_i |i\rangle = \sum_{lm} \langle i|i\rangle \tilde{A}_{il}S_{li}S^{-1}_{im} \langle m|i\rangle = \left(\tilde{\mathbf{A}}\mathbf{S}\right)_i . \tag{3.26}$$

Note also that there is an alternative way of performing a non-Hermitian projection

$$\begin{aligned}&\hat{\mathbf{P}}_i^\dagger\hat{\mathbf{A}}\hat{\mathbf{P}}_i^\dagger = \sum_{kl} |i^*\rangle \langle i|k\rangle \tilde{A}_{kl} \langle l|i^*\rangle \langle i| = \\ &\sum_{klm} |m\rangle S^{-1}_{mi}S_{ik}\tilde{A}_{kl}\delta_{li} \langle i|\end{aligned} \tag{3.27}$$

with an associated representation given by

$$\left(\mathbf{S}\tilde{\mathbf{A}}\right)_i . \tag{3.28}$$

Finally, and also for future reference, a straightforward application of the inversion operation (Eq. 3.13) onto the projector operator gives

$$\left[\hat{\mathbf{P}}_i^\dagger\right]^{-1} = \left[\sum_j |j\rangle S^{-1}_{ji} \langle i|\right]^{-1} = \sum_j |i^*\rangle S_{ij} \langle j^*| = \hat{\mathbf{P}}_i^\dagger. \tag{3.29}$$

Since $\left[\hat{\mathbf{P}}_i^\dagger\right]^{-1}\hat{\mathbf{P}}_i^\dagger = \hat{\mathbf{P}}_i^\dagger\hat{\mathbf{P}}_i^\dagger \neq \hat{\mathbf{I}}$, the inversion of a projector operator is not a true inverse, but a generalized inverse which obeys the Penrose condition [**?**]:

$$\hat{\mathbf{P}}_i^\dagger \left[\hat{\mathbf{P}}_i^\dagger\right]^{-1}\hat{\mathbf{P}}_i^\dagger = \hat{\mathbf{P}}_i^\dagger. \tag{3.30}$$

3.4 Projection onto a subspace: Integer and non-integer dimension.

The projection onto a subspace of dimension bigger than one is now carried out by the generalized projectors

$$\begin{aligned}\hat{\mathbf{P}}_{\mathrm{M}} &= \sum_{m,i} |m\rangle\, S^{-1}_{mi}\, \langle i| = \sum_{m} |m\rangle\, \langle m^*|,\\ \hat{\mathbf{P}}^{\dagger}_{\mathrm{M}} &= \sum_{m,i} |i\rangle\, S^{-1}_{im}\, \langle m| = \sum_{m} |m^*\rangle\, \langle m|,\end{aligned} \tag{3.31}$$

where m runs now over a selected subset M consisting of $N_{\mathrm{M}}(< N)$ elements of the direct basis set. As can be seen in the right-hand expressions, this restricted summation also implies to run over the corresponding subset in the dual space. The letters i and j will always denote the elements of the full direct and dual spaces from now on. The remaining direct basis elements constitute the subset R such that

$$\hat{\mathbf{I}} = \hat{\mathbf{P}}_{\mathrm{M}} + \hat{\mathbf{P}}_{\mathrm{R}} = \hat{\mathbf{P}}^{\dagger}_{\mathrm{M}} + \hat{\mathbf{P}}^{\dagger}_{\mathrm{R}}. \tag{3.32}$$

We now propose to write our full vector space as

$$\begin{aligned}\hat{\mathbf{I}} &= (\hat{\mathbf{P}}_{\mathrm{M}} + \hat{\mathbf{P}}_{\mathrm{R}})\hat{\mathbf{I}}(\hat{\mathbf{P}}_{\mathrm{M}} + \hat{\mathbf{P}}_{\mathrm{R}}),\\ \hat{\mathbf{I}} &= (\hat{\mathbf{P}}^{\dagger}_{\mathrm{M}} + \hat{\mathbf{P}}^{\dagger}_{\mathrm{R}})\hat{\mathbf{I}}(\hat{\mathbf{P}}^{\dagger}_{\mathrm{M}} + \hat{\mathbf{P}}^{\dagger}_{\mathrm{R}}),\\ \hat{\mathbf{I}} &= (\hat{\mathbf{P}}_{\mathrm{M}} + \hat{\mathbf{P}}_{\mathrm{R}})\hat{\mathbf{I}}(\hat{\mathbf{P}}^{\dagger}_{\mathrm{M}} + \hat{\mathbf{P}}^{\dagger}_{\mathrm{R}}),\\ \hat{\mathbf{I}} &= (\hat{\mathbf{P}}^{\dagger}_{\mathrm{M}} + \hat{\mathbf{P}}^{\dagger}_{\mathrm{R}})\hat{\mathbf{I}}(\hat{\mathbf{P}}_{\mathrm{M}} + \hat{\mathbf{P}}_{\mathrm{R}}).\end{aligned} \tag{3.33}$$

The four equivalent expressions give rise to four different ways of partitioning the full vector space:

$$\hat{\mathbf{I}} = \hat{\mathbf{P}}_{\mathrm{M}}\hat{\mathbf{I}}\hat{\mathbf{P}}_{\mathrm{M}} + \hat{\mathbf{P}}_{\mathrm{R}}\hat{\mathbf{I}}\hat{\mathbf{P}}_{\mathrm{R}} \tag{3.34}$$

$$\hat{\mathbf{I}} = \hat{\mathbf{P}}^{\dagger}_{\mathrm{M}}\hat{\mathbf{I}}\hat{\mathbf{P}}^{\dagger}_{\mathrm{M}} + \hat{\mathbf{P}}^{\dagger}_{\mathrm{R}}\hat{\mathbf{I}}\hat{\mathbf{P}}^{\dagger}_{\mathrm{R}} \tag{3.35}$$

$$\hat{\mathbf{I}} = \hat{\mathbf{P}}_{\mathrm{M}}\hat{\mathbf{I}}\hat{\mathbf{P}}^{\dagger}_{\mathrm{M}} + \hat{\mathbf{P}}_{\mathrm{M}}\hat{\mathbf{I}}\hat{\mathbf{P}}^{\dagger}_{\mathrm{R}} + \hat{\mathbf{P}}_{\mathrm{R}}\hat{\mathbf{I}}\hat{\mathbf{P}}^{\dagger}_{\mathrm{M}} + \hat{\mathbf{P}}_{\mathrm{R}}\hat{\mathbf{I}}\hat{\mathbf{P}}^{\dagger}_{\mathrm{R}} \tag{3.36}$$

$$\hat{\mathbf{I}} = \hat{\mathbf{P}}^{\dagger}_{\mathrm{M}}\hat{\mathbf{I}}\hat{\mathbf{P}}_{\mathrm{M}} + \hat{\mathbf{P}}^{\dagger}_{\mathrm{M}}\hat{\mathbf{I}}\hat{\mathbf{P}}_{\mathrm{R}} + \hat{\mathbf{P}}^{\dagger}_{\mathrm{R}}\hat{\mathbf{I}}\hat{\mathbf{P}}_{\mathrm{M}} + \hat{\mathbf{P}}^{\dagger}_{\mathrm{R}}\hat{\mathbf{I}}\hat{\mathbf{P}}_{\mathrm{R}} \tag{3.37}$$

By leaving $\hat{\mathbf{I}}$ in between the projectors the meaning of each term as partial projections of the original full vector space becomes clear. Equations 3.34 and 3.35 contain what we have called non-Hermitian projections in previous section. There the full vector space has been partitioned into two complementary orthogonal subspaces (thereby the two cross projections are missing in the expressions). Equations 3.36 and 3.37 contain Hermitian projections. These, as we explain below, do not generate proper orthogonal vector spaces since the cross projections do not vanish. A graphical illustration of the different projection operations which will be useful in the ensuing discussion is shown in Fig. 3.1.

We will first consider the result of performing the direct Hermitian projection:

$$\begin{aligned}\hat{\mathbf{I}}_{\mathcal{M}} = \hat{\mathbf{P}}^{\dagger}_{\mathrm{M}}\hat{\mathbf{I}}\hat{\mathbf{P}}_{\mathrm{M}} = &\sum_{m,n} |m^*\rangle\, \langle m|\, \hat{\mathbf{I}}\, |n\rangle\, \langle n^*| =\\ &\sum_{m,n} |m^*\rangle\, S_{mn}\, \langle n^*|.\end{aligned} \tag{3.38}$$

The representation of this projection in the direct basis set is given by

$$\langle m|\,\hat{\mathbf{I}}_{\mathcal{M}}\,|n\rangle = S_{mn} \equiv \mathbf{S}_{\mathrm{M}}. \tag{3.39}$$

While this result was somewhat expected, it hides a pitfall since $\hat{\mathbf{I}}_{\mathcal{M}}$ is not idempotent (this is obvious by noticing that $\hat{\mathbf{I}}_{\mathcal{M}}\hat{\mathbf{I}}_{\mathcal{M}} \neq \hat{\mathbf{I}}_{\mathcal{M}}$). Therefore the partition it represents is not a proper vector subspace. This prompt us to introduce a quantity defined by the integration of the diagonal elements of a given projection represented in real space. For the full vector space we started with this one writes

$$D = \int \langle \vec{r}|\,\hat{\mathbf{I}}\,|\vec{r}\rangle\, d\vec{r}. \tag{3.40}$$

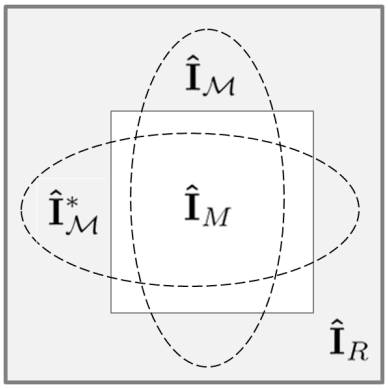

Fig. 3.1: Schematic representation of the two types of projections explained in the text and the resulting subspaces. Areas within the dashed lines represent subspaces with non-integer dimension, i.e., not orthogonal to the remaining area or subspace. The areas delimited by the solid line represent subspaces with integer dimensions, i.e., orthogonal to each other.

Explicitly evaluated one obtains

$$D = \int \sum_{i,j} \langle \vec{r}|i^*\rangle\, S_{ij}\, \langle j^*|\vec{r}\rangle d\vec{r} =$$

$$\sum_{i,j} S_{ij} \int \phi_i^* \phi_j^{*\dagger} d\vec{r} = \sum_{i,j} S_{ij} S^{-1}_{ji} = Tr\left[\mathbf{S}\mathbf{S}^{-\mathbf{1}}\right] = Tr\left[\mathbf{I}\right] = N, \tag{3.41}$$

which, obviously, is the number of elements of the full starting space, N. On the other hand, when one evaluates such quantity for $\hat{\mathbf{I}}_{\mathcal{M}}$ one obtains

$$D_{\mathcal{M}} = \int \langle \vec{r}|\,\hat{\mathbf{I}}_{\mathcal{M}}\,|\vec{r}\rangle\, d\vec{r} = Tr\left[\mathbf{S}_{\mathrm{M}}\mathbf{S}^{-1}_{\mathrm{M}}\right], \tag{3.42}$$

which is clearly $\neq N_{\mathrm{M}}$ and may be a non-integer value. This "subspace" with non-integer dimension is represented in Fig. 3.1 by the oval area within the dashed lines. Another manifestation of this non-integer dimension is given by the representation of $\hat{\mathbf{I}}_{\mathcal{M}}$ in the dual subspace

$$\langle m^*|\,\hat{\mathbf{I}}_{\mathcal{M}}\,|n^*\rangle = \mathbf{S}^{-1}_{\mathrm{M}}\mathbf{S}_{\mathrm{M}}\mathbf{S}^{-1}_{\mathrm{M}}. \tag{3.43}$$

which is not equal to $\mathbf{S}^{-1}_{\mathrm{M}}$, as naively expected.
The generalization of the direct Hermitian projection to any operator $\hat{\mathbf{A}}$ is given by

$$\hat{\mathbf{A}}_{\mathcal{M}} = \hat{\mathbf{P}}^{\dagger}_{\mathrm{M}}\hat{\mathbf{A}}\hat{\mathbf{P}}_{\mathrm{M}} = \sum_{m,n} |m^*\rangle\, A_{mn}\, \langle n^*|\,, \tag{3.44}$$

whose representation in the direct basis subset is

$$\langle m|\,\hat{\mathbf{A}}_{\mathcal{M}}\,|n\rangle = \mathbf{A}_{\mathrm{M}} \tag{3.45}$$

and in the dual basis subset is

$$\langle m^*|\,\hat{\mathbf{A}}_{\mathcal{M}}\,|n^*\rangle = \mathbf{S}^{-1}_{\mathrm{M}}\mathbf{A}_{\mathrm{M}}\mathbf{S}^{-1}_{\mathrm{M}}. \tag{3.46}$$

Likewise, the dual Hermitian projection, already introduced in the one-dimensional case, defines a new "subspace"

$$\hat{\mathbf{I}}^*_{\mathcal{M}} = \hat{\mathbf{P}}_{\mathrm{M}}\hat{\mathbf{I}}\hat{\mathbf{P}}^{\dagger}_{\mathrm{M}} = \sum_{m,n} |m\rangle \langle m^*| \hat{\mathbf{I}} |n^*\rangle \langle n| = \sum_{m,n} |m\rangle S^{-1}_{mn} \langle n| \tag{3.47}$$

with a non-integer dimension given by

$$D^*_{\mathcal{M}} = \int \langle \vec{r}| \hat{\mathbf{I}}^*_{\mathcal{M}} |\vec{r}\rangle \, d\vec{r} = Tr\left[\mathbf{S}^{-1}_{\mathrm{M}}\mathbf{S}_{\mathrm{M}}\right]. \tag{3.48}$$

which coincides with $D_{\mathcal{M}}$. Figure 3.1 depicts this subspace as a different oval area within dashed lines. Its representation in the dual subspace is the "expected" one

$$\langle m^*| \hat{\mathbf{I}}^*_{\mathcal{M}} |n^*\rangle = \mathbf{S}^{-1}_{\mathrm{M}}, \tag{3.49}$$

but its representation in the direct subspace is not

$$\langle m| \hat{\mathbf{I}}^*_{\mathcal{M}} |n\rangle = \mathbf{S}_{\mathrm{M}}\mathbf{S}^{-1}_{\mathrm{M}}\mathbf{S}_{\mathrm{M}}. \tag{3.50}$$

The generalized dual Hermitian projection to any operator $\hat{\mathbf{A}}$ is thus given by

$$\hat{\mathbf{A}}^*_{\mathcal{M}} = \hat{\mathbf{P}}_{\mathrm{M}}\hat{\mathbf{A}}\hat{\mathbf{P}}^{\dagger}_{\mathrm{M}} = \sum_{m,n} |m\rangle \tilde{A}_{mn} \langle n|, \tag{3.51}$$

whose representation in the direct basis subset is

$$\langle m| \hat{\mathbf{A}}^*_{\mathcal{M}} |n\rangle = \mathbf{S}_{\mathrm{M}}\tilde{\mathbf{A}}_{\mathrm{M}}\mathbf{S}_{\mathrm{M}}. \tag{3.52}$$

Notice that this matrix multiplication does not only involve matrices of reduced dimension since the evaluation of $\tilde{\mathbf{A}}$ requires matrix representations in the initial full vector space.

Lastly and for completeness we note that we can also perform non-Hermitian projections. These projections also generate new subspaces, which in this case have integer dimensions:

$$D_{\mathrm{M}} = \int \langle \vec{r}| \hat{\mathbf{P}}^{\dagger}_{\mathrm{M}}\hat{\mathbf{I}}\hat{\mathbf{P}}^{\dagger}_{\mathrm{M}} |\vec{r}\rangle \, d\vec{r} = \int \langle \vec{r}| \hat{\mathbf{P}}_{\mathrm{M}}\hat{\mathbf{I}}\hat{\mathbf{P}}_{\mathrm{M}} |\vec{r}\rangle \, d\vec{r} = \int \langle \vec{r}| \hat{\mathbf{I}}_{\mathrm{M}} |\vec{r}\rangle \, d\vec{r} = Tr\left[\mathbf{I}_{\mathrm{M}}\right] = N_{\mathrm{M}}. \tag{3.53}$$

The subspace represented by $\hat{\mathbf{I}}_{\mathrm{M}}$ is now orthogonal to the rest of the initial vector space. This is depicted by the square area within solid lines in Fig. 3.1. Operators projected in this manner can also be represented on the direct and the dual subspaces and we will make use of these representations in the following sections. It is, however, worth noting here that in order to recover the equivalent of the one-dimensional representations in Eqs. 3.26 and 3.28 one must represent at the same time on both direct and dual subsets which are orthogonal to each other:

$$\langle m^*| \hat{\mathbf{P}}_{\mathrm{M}}\hat{\mathbf{A}}\hat{\mathbf{P}}_{\mathrm{M}} |n\rangle = \left(\tilde{\mathbf{A}}\mathbf{S}\right)_{\mathrm{M}} \tag{3.54}$$

and similarly:

$$\langle m| \hat{\mathbf{P}}^{\dagger}_{\mathrm{M}}\hat{\mathbf{A}}\hat{\mathbf{P}}^{\dagger}_{\mathrm{M}} |n^*\rangle = \left(\mathbf{S}\tilde{\mathbf{A}}\right)_{\mathrm{M}}. \tag{3.55}$$

3.5 Block orthogonal metrics.

We revisit now, from a projection perspective, block-orthogonal metrics which were already introduced in Ref. Thygesen:prb:06. The projectors introduced in previous section can be used to build a new basis set:

$$\begin{aligned}&\{|i_\Delta\rangle\} = \hat{\mathbf{P}}_{\mathrm{M}}\{|i\rangle\} + \hat{\mathbf{P}}^{\dagger}_{\mathrm{R}}\{|i^*\rangle\} = \\ &\{\sum_{m,j,i} |m\rangle\, S^{-1}_{mj}\, \langle j|i\rangle\} + \{\sum_{r,j,i} |r^*\rangle\, S_{rj}\, \langle j^*|i^*\rangle\} = \{|m\rangle\} + \{|r^*\rangle\}.\end{aligned} \tag{3.56}$$

$$\begin{aligned}&\{|i_\nabla\rangle\} = \hat{\mathbf{P}}^{\dagger}_{\mathrm{M}}\{|i^*\rangle\} + \hat{\mathbf{P}}_{\mathrm{R}}\{|i\rangle\} = \\ &\{\sum_{m,j,i} |m^*\rangle\, S_{mj}\, \langle j^*|i^*\rangle\} + \{\sum_{r,j,i} |r\rangle\, S^{-1}_{rj}\, \langle j|i\rangle\} = \{|m^*\rangle\} + \{|r\rangle\}.\end{aligned} \tag{3.57}$$

Here the labels m and r run only over the subspace selected by the projector operators. The representation of the identity operator in the basis set $\{|i_\nabla\rangle\}$ is given by

$$\begin{aligned}\langle m|\,\hat{\mathbf{I}}\,|n\rangle &= \sum_{i,j} \langle m|i\rangle\, S^{-1}_{ij}\, \langle j|n\rangle = \mathbf{S}_{\mathrm{M}} \\ \langle r^*|\,\hat{\mathbf{I}}\,|s^*\rangle &= \sum_{i,j} \langle r^*|i\rangle\, S^{-1}_{ij}\, \langle j|s^*\rangle = \mathbf{S}^{-1}_{\mathrm{R}} \\ \langle m|\,\hat{\mathbf{I}}\,|r^*\rangle &= \sum_{i,j} \langle m|i\rangle\, S^{-1}_{ij}\, \langle j|r^*\rangle = 0 \\ \langle r^*|\,\hat{\mathbf{I}}\,|m\rangle &= \sum_{i,j} \langle r^*|i\rangle\, S^{-1}_{ij}\, \langle j|m\rangle = 0\end{aligned} \tag{3.58}$$

and similarly for the basis set $\{|i_\nabla\rangle\}$. Here the labels m, n and r, s run only over the subspaces M and R*, respectively. In matrix form the block-orthogonality becomes clear:

$$\mathbf{S}_\Delta = \begin{pmatrix} \mathbf{S}_{\mathrm{M}} & 0 \\ 0 & \mathbf{S}^{-1}_{\mathrm{R}} \end{pmatrix},\ \mathbf{S}_\nabla = \begin{pmatrix} \mathbf{S}^{-1}_{\mathrm{M}} & 0 \\ 0 & \mathbf{S}_{\mathrm{R}} \end{pmatrix}. \tag{3.59}$$

The full identity operator can now be re-expressed with the help of these new basis sets as

$$\begin{aligned}\hat{\mathbf{I}} = &\sum_{i,j} |i_\Delta\rangle \left(\tilde{\mathbf{S}}_\Delta\right)_{ij} \langle i_\Delta| = \\ &\sum_{m,n} |m\rangle \left(\tilde{\mathbf{S}}_\Delta\right)_{mn} \langle n| + \sum_{m,r} |m\rangle \left(\tilde{\mathbf{S}}_\Delta\right)_{mr} \langle r^*| + \\ &\sum_{r,m} |r^*\rangle \left(\tilde{\mathbf{S}}_\Delta\right)_{rm} \langle m| + \sum_{r,s} |r^*\rangle \left(\tilde{\mathbf{S}}_\Delta\right)_{rs} \langle s^*|\end{aligned} \tag{3.60}$$

or

$$\begin{aligned}\hat{\mathbf{I}} = &\sum_{i,j} |i_\nabla\rangle \left(\tilde{\mathbf{S}}_\nabla\right)_{ij} \langle i_\nabla| = \\ &\sum_{m,n} |m^*\rangle \left(\tilde{\mathbf{S}}_\nabla\right)_{mn} \langle n^*| + \sum_{m,r} |m^*\rangle \left(\tilde{\mathbf{S}}_\nabla\right)_{mr} \langle r| \\ &+ \sum_{r,m} |r\rangle \left(\tilde{\mathbf{S}}_\nabla\right)_{rm} \langle m^*| + \sum_{r,t} |r\rangle \left(\tilde{\mathbf{S}}_\nabla\right)_{rs} \langle s|.\end{aligned} \tag{3.61}$$

The $\tilde{\mathbf{S}}_\Delta$ and $\tilde{\mathbf{S}}_\nabla$ matrices are the dual form of the block-orthogonal metrics in Eq. 3.59 which are explicitly written as

$$\tilde{\mathbf{S}}_\Delta = \begin{pmatrix} [\mathbf{S}_{\rm M}]^{-1} & 0 \\ 0 & \mathbf{S}^*_{\rm R} \end{pmatrix}, \; \tilde{\mathbf{S}}_\nabla = \begin{pmatrix} \mathbf{S}^*_{\rm M} & 0 \\ 0 & [\mathbf{S}_{\rm R}]^{-1} \end{pmatrix}. \tag{3.62}$$

Notice that $\mathbf{S}^*_{\rm M(R)}$ stands for $[\mathbf{S}^{-1}_{\rm M(R)}]^{-1}$. The dual basis in these new metrics has no direct correspondence with the direct and dual original basis sets. Using, e.g., the metric Δ, we can now define new projector operators as

$$\begin{aligned} \hat{\mathbf{P}}^\Delta_{\rm M} = \hat{\mathbf{P}}^{\Delta\dagger}_{\rm M} &= \sum_{m,n} |m\rangle \, [\mathbf{S}_{\rm M}]^{-1} \, \langle n|, \\ \hat{\mathbf{P}}^\Delta_{\rm R} = \hat{\mathbf{P}}^{\Delta\dagger}_{\rm R} &= \sum_{r,s} |r^*\rangle \, \mathbf{S}^*_{\rm R} \, \langle s^*| \end{aligned} \tag{3.63}$$

which add up to the identity operator

$$\hat{\mathbf{I}} = \hat{\mathbf{P}}^\Delta_{\rm M} \hat{\mathbf{I}} \hat{\mathbf{P}}^\Delta_{\rm M} + \hat{\mathbf{P}}^\Delta_{\rm R} \hat{\mathbf{I}} \hat{\mathbf{P}}^\Delta_{\rm R}. \tag{3.64}$$

(In a similar manner one can define projectors associated with the other metric ∇.) The dimension of both partitions is now integer. For instance:

$$\begin{aligned} D = &\int \langle \vec{r}| \, \hat{\mathbf{P}}^\Delta_{\rm M} \hat{\mathbf{I}} \hat{\mathbf{P}}^\Delta_{\rm M} \, |\vec{r}\rangle \, d\vec{r} = \\ &\int \sum_{m,n} \langle \vec{r}|m\rangle \, [\mathbf{S}_{\rm M}]^{-1} \, \langle n|\vec{r}\rangle d\vec{r} = Tr\,[\mathbf{I}_{\rm M}] = N_{\rm M}. \end{aligned} \tag{3.65}$$

The generalized representation of any one-body operator in terms of these basis sets is given by

$$\mathbf{A}_\Delta = \begin{pmatrix} \mathbf{A}_{\rm M} & (\tilde{\mathbf{A}}\mathbf{S})_{\rm MR} \\ (\mathbf{S}\tilde{\mathbf{A}})_{\rm RM} & \tilde{\mathbf{A}}_{\rm R} \end{pmatrix} \tag{3.66}$$

which is not block-diagonal any more. The same obviously holds for the other metric ∇:

$$\mathbf{A}_\nabla = \begin{pmatrix} \tilde{\mathbf{A}}_{\rm M} & (\mathbf{S}\tilde{\mathbf{A}})_{\rm MR} \\ (\tilde{\mathbf{A}}\mathbf{S})_{\rm RM} & \mathbf{A}_{\rm R} \end{pmatrix}. \tag{3.67}$$

It is useful to propose matrix transformations connecting all the metrics we have presented so far:

$$\mathbf{\Pi}^\dagger_\Delta \mathbf{A} \mathbf{\Pi}_\Delta = \mathbf{A}_\Delta, \tag{3.68}$$

and

$$\mathbf{\Pi}^\dagger_\nabla \tilde{\mathbf{A}} \mathbf{\Pi}_\nabla = \mathbf{A}_\nabla. \tag{3.69}$$

The matrices $\mathbf{\Pi}_\nabla$ and $\mathbf{\Pi}_\nabla$ are defined by

$$\mathbf{\Pi}_\Delta = \begin{pmatrix} \mathbf{I} & \mathbf{S}^{-1}_{\rm MR} \\ 0 & \mathbf{S}^{-1}_{\rm R} \end{pmatrix}, \; \mathbf{\Pi}_\nabla = \begin{pmatrix} \mathbf{I} & \mathbf{S}_{\rm MR} \\ 0 & \mathbf{S}_{\rm R} \end{pmatrix}. \tag{3.70}$$

The $\mathbf{\Pi}$ matrices are overlap matrices between this new basis and the direct basis: $\langle i|i_\Delta\rangle = (\mathbf{\Pi}_\nabla)_{ii}$ and the dual one $\langle i^*|i_\Delta\rangle = (\mathbf{\Pi}_\Delta)_{ii}$. We can now write the relationships

$$|i\rangle = \sum_j \left(\Pi^{-1}_\nabla\right)_{ij} |j_\nabla\rangle \quad |i\rangle = \sum_j \left(\Pi^{-1}_\Delta\right)_{ij} |j_\Delta\rangle \tag{3.71}$$

3.6 The projected charge

A natural starting point for the evaluation of many physical quantities in infinite systems which are characterized by a one-body Hamiltonian $\hat{\mathbf{H}}$ is the Green's function operator:

$$\left[(\omega-\mu\pm i\delta)\,\hat{\mathbf{I}}-\hat{\mathbf{H}}\right]\hat{\mathbf{G}}^{(\pm)}(\omega)=\hat{\mathbf{I}}, \tag{3.72}$$

where μ and ω are the chemical potential and energy, respectively, and +(-) denotes advanced(retarded) Green's function. For all practical purposes the Hamiltonian must be restricted to a finite region which is connected to the rest of the world through an energy dependent self-energy operator $\hat{\mathbf{\Sigma}}(\omega)$:

$$\left[(\omega-\mu)\,\hat{\mathbf{I}}-\hat{\mathbf{H}}-\hat{\mathbf{\Sigma}}(\omega)\right]\hat{\mathbf{G}}(\omega)=\hat{\mathbf{I}}. \tag{3.73}$$

At this point the Hamiltonian is supposed to represent a large enough system and contain all possible physically relevant information. The particular form of the self-energy operator $\hat{\mathbf{\Sigma}}$ (the retarded one from now on) is assumed not to be relevant in what follows. Making use of Eq. 3.6, one can easily show that the representation of Eq. 3.73 in matrix form is

$$\mathbf{G}(\omega)=\mathbf{S}\left[(\omega-\mu)\,\mathbf{S}-\mathbf{H}-\mathbf{\Sigma}(\omega)\right]^{-1}\mathbf{S}. \tag{3.74}$$

For convenience this is usually written as

$$\tilde{\mathbf{G}}(\omega)=\left[(\omega-\mu)\,\mathbf{S}-\mathbf{H}-\mathbf{\Sigma}(\omega)\right]^{-1}, \tag{3.75}$$

which, according to Eq. 3.13, can be directly obtained from the matrix representation in the direct basis of the operator equation

$$\left[\hat{\mathbf{G}}(\omega)\right]^{-1}=(\omega-\mu)\,\hat{\mathbf{I}}-\hat{\mathbf{H}}-\hat{\mathbf{\Sigma}}(\omega). \tag{3.76}$$

The partial charge or partial electronic density associated to a part of the space or to a subset of atoms or orbitals[82–84] (what we have called subspace M in previous sections) can be obtained from integration of the LDOS:

$$\rho_{\mathcal{M}}=\int_{-\infty}^{0}D_{\mathcal{M}}(\omega)d\omega, \tag{3.77}$$

which, in turn, is computed through a projection of the Green's function operator. We begin by considering the direct Hermitian projection, as explained in Sec. 3.4. For simplicity's sake, we assume spin degeneracy from now on:

$$D_{\mathcal{M}}(\omega)=-\frac{2}{\pi}Im\left[\int\left\langle\vec{r}|\hat{\mathbf{P}}_{\mathrm{M}}^{\dagger}\hat{\mathbf{G}}(\omega)\hat{\mathbf{P}}_{\mathrm{M}}|\vec{r}\right\rangle d\vec{r}\right]. \tag{3.78}$$

We now carry out the volume integral:

$$\begin{aligned}&\int\left\langle\vec{r}|\hat{\mathbf{P}}_{\mathrm{M}}^{\dagger}\hat{\mathbf{G}}\hat{\mathbf{P}}_{\mathrm{M}}|\vec{r}\right\rangle d\vec{r}=\\&=\int\sum_{m,n}\langle\vec{r}|m^{*}\rangle\left\langle m|\hat{\mathbf{G}}|n\right\rangle\langle n^{*}|\vec{r}\rangle d\vec{r}=\\&=\sum_{m,n}\left\langle m|\hat{\mathbf{G}}|n\right\rangle\int\phi_{m}^{*}(\vec{r})\phi_{n}^{\dagger*}(\vec{r})d\vec{r}=\sum_{m,n}G_{mn}S_{nm}^{-1}.\end{aligned} \tag{3.79}$$

The LDOS associated with this projection is thus given by

$$D_{\mathcal{M}}(\omega) = -\frac{2}{\pi} Im \left\{ Tr \left[\mathbf{G}_{\mathrm{M}}(\omega) \mathbf{S}_{\mathrm{M}}^{-1} \right] \right\}. \tag{3.80}$$

Notice that when one integrates Eq. 7.4 up to ∞ one gets what we have previously defined as dimension of the projected subspace $D_{\mathcal{M}}$. (We will use the same letter for the ω-dependent quantity and the integrated one from now on).
In the case of the dual Hermitian projection the partial electron density is given by

$$\begin{aligned} \rho^*_{\mathcal{M}} &= -\frac{2}{\pi} \int_{-\infty}^{0} Im \left[\int \left\langle \vec{r} | \hat{\mathbf{P}}_{\mathrm{M}} \hat{\mathbf{G}}(\omega) \hat{\mathbf{P}}^{\dagger}_{\mathrm{M}} | \vec{r} \right\rangle d\vec{r} \right] d\omega = \\ &= -\frac{2}{\pi} \int_{-\infty}^{0} Im \left\{ Tr \left[\tilde{\mathbf{G}}_{\mathrm{M}}(\omega) \mathbf{S}_{\mathrm{M}} \right] \right\} d\omega. \end{aligned} \tag{3.81}$$

We therefore may define

$$D^*_{\mathcal{M}}(\omega) = -\frac{2}{\pi} Im \left\{ Tr \left[\tilde{\mathbf{G}}_{\mathrm{M}}(\omega) \mathbf{S}_{\mathrm{M}} \right] \right\}. \tag{3.82}$$

The non-Hermitian projections give the well-known result known as Mulliken population analysis[85]:

$$\begin{aligned} \rho_{\mathrm{M}} &= \int_{-\infty}^{0} D_{\mathrm{M}}(\omega) d\omega = \\ &= -\frac{2}{\pi} \int_{-\infty}^{0} Im \left[\int \left\langle \vec{r} | \hat{\mathbf{P}}_{\mathrm{M}} \hat{\mathbf{G}}(\omega) \hat{\mathbf{P}}_{\mathrm{M}} | \vec{r} \right\rangle d\vec{r} \right] d\omega = \\ &= -\frac{2}{\pi} \int_{-\infty}^{0} Im \left[\int \left\langle \vec{r} | \hat{\mathbf{P}}^{\dagger}_{\mathrm{M}} \hat{\mathbf{G}}(\omega) \hat{\mathbf{P}}^{\dagger}_{\mathrm{M}} | \vec{r} \right\rangle d\vec{r} \right] d\omega = \\ &= -\frac{2}{\pi} \int_{-\infty}^{0} Im \left\{ Tr \left[\tilde{\mathbf{G}}(\omega) \mathbf{S} \right]_{\mathrm{M}} \right\} d\omega. \end{aligned} \tag{3.83}$$

Finally, one can also evaluate the charge using the block-orthogonal metric Δ discussed in Sec. 3.5:

$$\rho^{\Delta}_{\mathrm{M}} = \int_{-\infty}^{0} D^{\Delta}_{\mathrm{M}}(\omega) d\omega. \tag{3.84}$$

where the LDOS is given by

$$D^{\Delta}_{\mathrm{M}}(\omega) = -\frac{2}{\pi} Im \left[\int \left\langle \vec{r} | \hat{\mathbf{P}}^{\Delta}_{\mathrm{M}} \hat{\mathbf{G}}(\omega) \hat{\mathbf{P}}^{\Delta}_{\mathrm{M}} | \vec{r} \right\rangle d\vec{r} \right]. \tag{3.85}$$

Performing the projection and volume integration one obtains

$$\begin{aligned} &\int \left\langle \vec{r} | \hat{\mathbf{P}}^{\Delta}_{\mathrm{M}} \hat{\mathbf{G}} \hat{\mathbf{P}}^{\Delta}_{\mathrm{M}} | \vec{r} \right\rangle d\vec{r} = \\ &\int \sum_{k,l} \langle \vec{r} | k^* \rangle \left\langle k | \hat{\mathbf{G}} | l \right\rangle \langle l^* | \vec{r} \rangle d\vec{r} = \\ &\sum_{k,l} \left\langle k | \hat{\mathbf{G}} | l \right\rangle \int \phi^*_k(\vec{r}) \phi^{\dagger *}_l(\vec{r}) d\vec{r} = \sum_{k,l} G_{lk} [\mathbf{S}_{\mathrm{M}}]^{-1}_{kl}. \end{aligned} \tag{3.86}$$

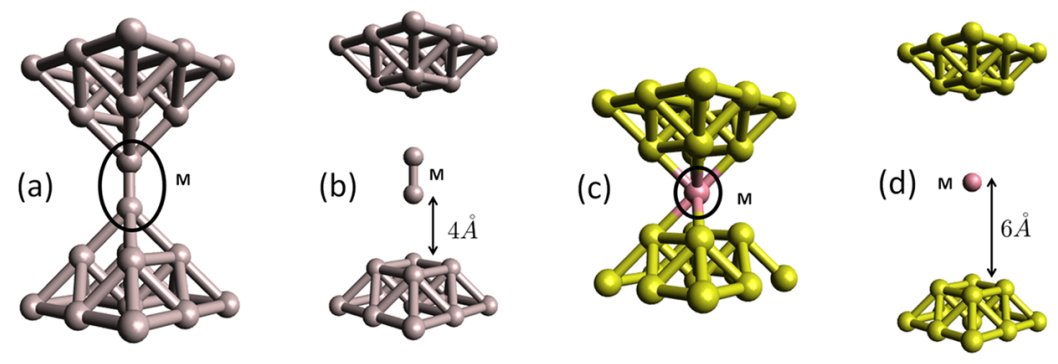

Fig. 3.2: (a-b) View of an aluminum nanocontact for two different connections between the central region M and the electrodes. (c-d) The same for a gold nanocontact with a cobalt atom embedded.

The LDOS is thus given by

$$D_{\mathrm{M}}^{\Delta}(\omega) = -\frac{2}{\pi} Im\left\{Tr\left[\mathbf{G}_{\mathrm{M}}(\omega)[\mathbf{S}_{\mathrm{M}}]^{-1}\right]\right\}. \tag{3.87}$$

Notice that Eq. 3.87 is different from Eq. 3.80. Likewise, for the alternative block-orthogonal metric ∇ one gets

$$\rho_{\mathrm{M}}^{\nabla} = -\frac{2}{\pi}\int_{-\infty}^{0} Im\left\{Tr\left[\tilde{\mathbf{G}}_{\mathrm{M}}(\omega)\mathbf{S}_{\mathrm{M}}^{*}\right]\right\} d\omega, \tag{3.88}$$

from which we may define

$$D_{\mathrm{M}}^{\nabla}(\omega) = -\frac{2}{\pi} Im\left\{Tr\left[\tilde{\mathbf{G}}_{\mathrm{M}}(\omega)\mathbf{S}_{\mathrm{M}}^{*}\right]\right\}. \tag{3.89}$$

To illustrate the different results obtained from the different projections and the different basis sets (direct and block- orthogonal) we have considered two simple models of metallic nanocontacts. The first one is an Al nanocontact with two slightly different atomic structures as shown in Figs. 3.2(a) and (b). They differ in how strongly coupled the two central atoms are to the rest of the system. The other model is a Au nanocontact with a Co atom in the middle [Figs. 3.2(c) and (d)]. Again, two slightly different geometries with different overlaps between the central atom and the electrodes are considered.
The selected region or subspace for projection, M, is indicated in both figures. The DFT calculations have been performed with our ANT.G code [59] which is based on the non-equilibrium Green's function formalism and interfaces with GAUSSIAN [53]. We have chosen a standard exchange-correlation functional in the generalized gradient approximation[33, 35] for all calculations and various basis sets explained in the caption of Table 3.1.
Table 3.1 shows the results for the charges associated to the different projections along with the dimension of the projected subspace. As a reference, the charge Q of the isolated M subspaces (when they are infinitely far apart from the electrodes and therefore neutral) is also shown (second column). As can be appreciated, the projected charges lie in a wide range of values. The first result worth noticing is that the values of D_{M} increase to insanely large number as the basis set dimension increases. This is particularly notorious for

	Q	ρ_{M}	$\rho_{\mathrm{M}}^{\nabla}$	$\rho_{\mathrm{M}}^{\Delta}$	D_{M}	$\rho_{\mathcal{M}}^{*}$	$\rho_{\mathcal{M}}$	$D_{\mathcal{M}}$
Al(1)	6	6.38	2.89	11.39	16	6.03	34.94	45.16
Al(2)	26	24.03	22.52	26.87	36	23.52	30.44	41.86
Al(3)	26	23.20	22.76	35.10	72	25.83	410.49	495.00
Co(1)	17	12.96	15.26	24.66	44	22.82	753.18	1043.58
Co(2)	27	26.61	23.95	29.26	36	26.04	57.64	72.34
Co(3)	27	22.73	25.04	33.24	68	33.31	678.84	865.62
Al(4)	26	24.68	24.47	24.89	36	24.57	25.00	36.24
Co(4)	17	15.94	16.26	19.02	44	18.05	58.12	123.36
Co(5)	17	16.95	16.26	17.27	44	17.06	17.87	50.56

Table 3.1: Partial electronic charge in the central region (M) for four different systems, different basis sets, and the different projections discussed in the text (the metric dimension of these is also shown). For all atoms which are not part of the M region we have considered a minimal basis set (*sp*)[86]. For the Al nanocontacts, cases (1), (2), and (3) correspond to Fig. 3.2(a) with the same minimal basis set for the M region, the STO-3G basis set, and the 6-31G** basis set, respectively. Case (4) corresponds to Fig. 3.2(b) and the STO-3G basis set for the M region. For the Au-Co nanocontacts we consider the LANL2DZ pseudopotentials basis set [(1)], the STO-3G basis set [(2)], and the 6-31G** basis set [(3)] for the Co atom in the geometry shown in Fig. 3.2(c). Cases (4) and (5) correspond to Fig. 3.2(d) (two different distances, but only (5) shown) and the basis set LANL2DZ. Spin-polarized calculations are performed in all last five cases, but only the sum of spin-up and spin-down charges is shown.

the Al(3), Co(1), and Co(3) cases. This translates into unrealistic values of $\rho_{\mathcal{M}}$. Interestingly, the values of $\rho_{\mathcal{M}}^{*}$ are very reasonable. The other three values for the charge, ρ_{M}, $\rho_{\mathrm{M}}^{\Delta}$ and $\rho_{\mathrm{M}}^{\nabla}$, are all within acceptable limits, although still present a large dispersion. In the case of nanocontacts with a single element (Al) these values can be directly compared to the values of Q since we do not expect a significant charge transfer between the electrodes and the M subspace. It is worth noticing that the Mulliken value for the charge, ρ_{M}, generally lies in between the other two values obtained from the two different block orthogonal metrics Δ and ∇. The last three rows present results where the M region has been separated from the electrodes, reducing thus the overlap. The differences between all values are consequently reduced as well, including $\rho_{\mathcal{M}}$. For Co a larger distance than for Al is required to get similar values for all types of projections.

3.7 Reduced Green's functions and effective Hamiltonians

We are now fully equipped to obtain the effective Hamiltonian associated to the M subspace, i.e, what we have called in the introduction the active region. Our first aim is to obtain an expression similar to the one in Eq. 3.76, but projected onto this region. Then one could read out the Hamiltonian and the associated self-energy from it. The dual Hermitian projection of the Green's function operator onto this subspace, as defined in Eq. 3.51, is

$$\hat{\mathbf{P}}_{\mathrm{M}}\hat{\mathbf{G}}\hat{\mathbf{P}}_{\mathrm{M}}^{\dagger} = \hat{\mathbf{P}}_{\mathrm{M}}\left[(\omega-\mu)\,\hat{\mathbf{I}} - \hat{\mathbf{H}} - \hat{\mathbf{\Sigma}}\right]^{-1}\hat{\mathbf{P}}_{\mathrm{M}}^{\dagger} \tag{3.90}$$

or equivalently

$$\left[\hat{\mathbf{P}}_{\mathrm{M}}\hat{\mathbf{G}}\hat{\mathbf{P}}_{\mathrm{M}}^{\dagger}\right]^{-1} = \left[\hat{\mathbf{P}}_{\mathrm{M}}\left[(\omega-\mu)\,\hat{\mathbf{I}} - \hat{\mathbf{H}} - \hat{\mathbf{\Sigma}}\right]^{-1}\hat{\mathbf{P}}_{\mathrm{M}}^{\dagger}\right]^{-1}. \tag{3.91}$$

Notice that

$$\left[\hat{\mathbf{P}}_{\mathrm{M}}\hat{\mathbf{G}}\hat{\mathbf{P}}_{\mathrm{M}}^{\dagger}\right]^{-1} \neq \hat{\mathbf{P}}_{\mathrm{M}}^{\dagger}\left[\hat{\mathbf{G}}\right]^{-1}\hat{\mathbf{P}}_{\mathrm{M}}, \tag{3.92}$$

but we can always write

$$\left[\hat{\mathbf{P}}_{\mathrm{M}}\hat{\mathbf{G}}\hat{\mathbf{P}}_{\mathrm{M}}^{\dagger}\right]^{-1} = (\omega-\mu)\,\hat{\mathbf{I}}_{\mathcal{M}} - \hat{\mathbf{H}}_{\mathcal{M}} - \hat{\mathbf{\Sigma}}_{\mathcal{M}}, \tag{3.93}$$

where the first two terms on the right-hand side are now direct projections

$$\hat{\mathbf{I}}_{\mathcal{M}} = \hat{\mathbf{P}}_{\mathrm{M}}^{\dagger}\hat{\mathbf{I}}\hat{\mathbf{P}}_{\mathrm{M}} \tag{3.94}$$

$$\hat{\mathbf{H}}_{\mathcal{M}} = \hat{\mathbf{P}}_{\mathrm{M}}^{\dagger}\hat{\mathbf{H}}\hat{\mathbf{P}}_{\mathrm{M}} \tag{3.95}$$

while the third one is given by

$$\hat{\mathbf{\Sigma}}_{\mathcal{M}} = \hat{\mathbf{P}}_{\mathrm{M}}^{\dagger}\hat{\mathbf{\Sigma}}\hat{\mathbf{P}}_{\mathrm{M}} + \hat{\mathbf{\Sigma}}'_{\mathcal{M}}. \tag{3.96}$$

We need a new term added to the projected self-energy operator which is thus defined by

$$\hat{\mathbf{\Sigma}}'_{\mathcal{M}} = \left[\hat{\mathbf{P}}_{\mathrm{M}}\hat{\mathbf{G}}\hat{\mathbf{P}}_{\mathrm{M}}^{\dagger}\right]^{-1} - \hat{\mathbf{P}}_{\mathrm{M}}^{\dagger}\left[\hat{\mathbf{G}}\right]^{-1}\hat{\mathbf{P}}_{\mathrm{M}}. \tag{3.97}$$

where both direct and dual projections appear in the definition. Making use now of the definition of inverse, we carry out the projection and inversion in the left-hand side of Eq. 3.93:

$$\begin{aligned}\left[\hat{\mathbf{P}}_{\mathrm{M}}\hat{\mathbf{G}}\hat{\mathbf{P}}_{\mathrm{M}}^{\dagger}\right]^{-1} = \left[\sum_{m,n}|m\rangle\,\tilde{G}_{mn}\,\langle n|\right]^{-1} = \\ \sum_{m,n}|m^{*}\rangle\,[\tilde{\mathbf{G}}_{\mathrm{M}}]^{-1}_{mn}\,\langle n^{*}|\,,\end{aligned} \tag{3.98}$$

so that Eq. 3.93 becomes

$$[\tilde{\mathbf{G}}_{\mathrm{M}}]^{-1} = (\omega-\mu)\,\mathbf{S}_{\mathrm{M}} - \mathbf{H}_{\mathrm{M}} - \mathbf{\Sigma}_{\mathrm{M}} \tag{3.99}$$

when represented in the direct basis. Finally we can obtain the self-energy matrix:

$$\mathbf{\Sigma}_{\mathrm{M}} = (\omega-\mu)\,\mathbf{S}_{\mathrm{M}} - \mathbf{H}_{\mathrm{M}} - [\tilde{\mathbf{G}}_{\mathrm{M}}]^{-1}. \tag{3.100}$$

If required, we can also obtain $\mathbf{\Sigma}'_{\mathrm{M}}$ from Eq. 3.97. This way of obtaining the self-energy associated to any subspace is often called "reversal engineering" [76]. Notice that Eq. 3.100 is somewhat expected by looking at Eq. 3.75, but our projector theory gives us a rigorous way of obtaining it. Following Eq. 3.44 one could also apply the alternative projection $\hat{\mathbf{P}}_{\mathrm{M}}^{\dagger}\hat{\mathbf{G}}\hat{\mathbf{P}}_{\mathrm{M}}$ and arrive at the following representation in direct space

$$[\mathbf{G}_{\mathrm{M}}]^{-1} = (\omega-\mu)\,\mathbf{S}_{\mathrm{M}}^{-1} - \tilde{\mathbf{H}}_{\mathrm{M}} - \tilde{\mathbf{\Sigma}}_{\mathrm{M}} \tag{3.101}$$

from which we obtain another expression for the self-energy matrix:

$$\tilde{\mathbf{\Sigma}}_{\mathrm{M}} = (\omega - \mu)\,\mathbf{S}_{\mathrm{M}}^{-1} - \tilde{\mathbf{H}}_{\mathrm{M}} - [\mathbf{G}_{\mathrm{M}}]^{-1}. \tag{3.102}$$

Finally, the self-energy matrix in the case of the two introduced block orthogonal metrics should be defined by

$$\mathbf{\Sigma}_{\mathrm{M}}^{\Delta} = (\omega - \mu)\,\mathbf{S}_{\mathrm{M}} - \mathbf{H}_{\mathrm{M}} - \mathbf{S}_{\mathrm{M}}[\mathbf{G}_{\mathrm{M}}]^{-1}\mathbf{S}_{\mathrm{M}}, \tag{3.103}$$

and

$$\mathbf{\Sigma}_{\mathrm{M}}^{\nabla} = (\omega - \mu)\,\mathbf{S}_{\mathrm{M}}^{-1} - \tilde{\mathbf{H}}_{\mathrm{M}} - \mathbf{S}_{\mathrm{M}}^{-1}[\tilde{\mathbf{G}}_{\mathrm{M}}]^{-1}\mathbf{S}_{\mathrm{M}}^{-1}. \tag{3.104}$$

Notice that the expressions for the self-energy in Eqs. 3.100, 3.102, 7.1, and 3.104 are all different. In conclusion, the choice of projection for a fully non-orthogonal basis set (direct or dual) or the choice of the block-orthogonal basis set (Δ or ∇) determines both a Hamiltonian and an associated self-energy. These two must go together for the evaluation of, e.g., conductance as next section shows.

3.8 The transmission function from a reduced Green's function

The transmission function T, which enters Landauer's formalism to compute the conductance, $G = \frac{2e^2}{h}T$, is given by:

$$T = Tr\left[\mathbf{t}^{\dagger}\mathbf{t}\right] \tag{3.105}$$

where $\mathbf{t} = \mathbf{\Gamma}_{\mathrm{R}}^{1/2}\tilde{\mathbf{G}}^{(+)}\mathbf{\Gamma}_{\mathrm{L}}^{1/2}$ and $\mathbf{t}^{\dagger} = \mathbf{\Gamma}_{\mathrm{L}}^{1/2}\tilde{\mathbf{G}}^{(-)}\mathbf{\Gamma}_{\mathrm{R}}^{1/2}$ are transmission matrices defined in terms of retarded (+) and advanced (-) Green's functions and coupling matrices to the right (R) and left (L) electrodes. We are assuming here that there is no direct electronic coupling between electrodes and that the self-energy $\mathbf{\Sigma}$ that appears in the Green's function (see Eq. 3.75) is known and equal to $\mathbf{\Sigma}_{\mathrm{R}} + \mathbf{\Sigma}_{\mathrm{L}}$. The coupling matrices are defined as usual: $\mathbf{\Gamma} = i(\mathbf{\Sigma}^{(+)} - \mathbf{\Sigma}^{(-)})$. The transmission matrices $\mathbf{t}^{\dagger}$ and $\mathbf{t}$ contain information about transmission amplitudes between orbitals or basis elements at the entrance and exit of the scattering region. By using the cyclic property of the trace, the transmission function can thus be written in its most popular form:

$$T = Tr\left[\mathbf{\Gamma}_{\mathrm{L}}\tilde{\mathbf{G}}^{(-)}\mathbf{\Gamma}_{\mathrm{R}}\tilde{\mathbf{G}}^{(+)}\right], \tag{3.106}$$

Notice that the final product of four matrices *is not* simply the result of representing the product of operators

$$\hat{\mathbf{\Gamma}}_{\mathrm{L}}\hat{\mathbf{G}}^{(-)}\hat{\mathbf{\Gamma}}_{\mathrm{R}}\hat{\mathbf{G}}^{(+)}, \tag{3.107}$$

in a non-orthogonal basis set (see Sec. 3.1) .
We are now interested in expressing the transmission function in terms of Green's functions and coupling matrices reduced or projected to a central

scattering region. As an example we will compute the conductance of the Al nanocontact studied in Sec. 3.6 where the central region M is the same used to analyse the projection of the charge [see Figs. 3.2 (a) and (b)]. First, to obtain the self-energy representing the left electrode, we can perform a projection onto the rest of the system:

$$\hat{\mathbf{P}}_{\mathrm{r}}\hat{\mathbf{G}}\hat{\mathbf{P}}_{\mathrm{r}}^{\dagger} = \hat{\mathbf{P}}_{\mathrm{r}}\left[(\omega-\mu)\,\hat{\mathbf{I}} - \hat{\mathbf{H}} - \hat{\mathbf{\Sigma}}_{\mathrm{L}} - \hat{\mathbf{\Sigma}}_{\mathrm{R}}\right]^{-1}\hat{\mathbf{P}}_{\mathrm{r}}^{\dagger}. \tag{3.108}$$

Following Eq. 3.100 we obtain a new left self-energy

$$\mathbf{\Sigma}_{\mathrm{L|r}} = (\omega-\mu)\,\mathbf{S}_{\mathrm{r}} - \mathbf{H}_{\mathrm{r}} - \mathbf{\Sigma}_{\mathrm{R|r}} - [\tilde{\mathbf{G}}_{\mathrm{r}}]^{-1}, \tag{3.109}$$

where $\hat{\mathbf{P}}_{\mathrm{r}}^{\dagger}\hat{\mathbf{\Sigma}}_{\mathrm{R}}\hat{\mathbf{P}}_{\mathrm{r}} := \mathbf{\Sigma}_{\mathrm{R|r}}$. Then, by performing a new projection onto the selected subspace M we obtain the new self-energy associated to the new right electrode:

$$\begin{aligned}&\hat{\mathbf{P}}_{\mathrm{M}}\hat{\mathbf{G}}_{\mathrm{r}}\hat{\mathbf{P}}_{\mathrm{M}}^{\dagger} = \\ &\hat{\mathbf{P}}_{\mathrm{M}}\left[(\omega-\mu)\,\hat{\mathbf{I}}_{\mathrm{r}} - \hat{\mathbf{H}}_{\mathrm{r}} - \hat{\mathbf{\Sigma}}_{\mathrm{R|r}} - \hat{\mathbf{\Sigma}}_{\mathrm{L|r}}\right]^{-1}\hat{\mathbf{P}}_{\mathrm{M}}^{\dagger},\end{aligned} \tag{3.110}$$

$$\mathbf{\Sigma}_{\mathrm{R|M}} = (\omega-\mu)\,\mathbf{S}_{\mathrm{M}} - \mathbf{H}_{\mathrm{M}} - \mathbf{\Sigma}_{\mathrm{L|M}} - [\tilde{\mathbf{G}}_{\mathrm{M}}]^{-1}, \tag{3.111}$$

where $\hat{\mathbf{\Sigma}}_{\mathrm{L|M}} = \hat{\mathbf{P}}_{\mathrm{M}}^{\dagger}\hat{\mathbf{\Sigma}}_{\mathrm{L|r}}\hat{\mathbf{P}}_{\mathrm{M}}$. Now the newly obtained $\tilde{\mathbf{G}}_{\mathrm{M}}$, $\hat{\mathbf{\Sigma}}_{\mathrm{L|M}}$, and $\hat{\mathbf{\Sigma}}_{\mathrm{R|M}}$ enter Eq. 3.106. This double-projection procedure has been illustrated through the dual Hermitian projection, but the same operations can be carried out with the other projections and with the block-orthogonal basis sets, as explained in previous section. In Figs. 3.3 (a) and (c) we plot the transmission function obtained for the systems shown in Fig. 3.2 (a) and (b). We also show the transmission for the same system with an intermediate distance [$d = 3$Å, Fig. 3.3 (b)] between the central region and the electrodes. The same basis set has been used in the panels (a-c). Panel (d) shows the transmission with a larger basis set for the structure in Fig. 3.2(a). Three different projections have been used in all cases, as described by Eq. 3.100, 7.1, and 3.104. The reduced Green's functions and coupling matrices in Eq. 3.106 have been chosen accordingly. When the central region is separated from the electrodes [see Fig. 3.3 (c)], the direct tunnelling between electrodes is negligible and the reduction operation is expected to be exact. In fact, the three projections give identical results and equal to the transmission obtained from the full Green's function (black solid line). This corroborates the mathematical procedure of reduction explained in previous section. On the other hand, when direct tunnelling between electrodes is finite, differences are expected between the full transmission and the ones obtained after reduction. This can be clearly seen in Figs. 3.3 (a), (b), and (d).

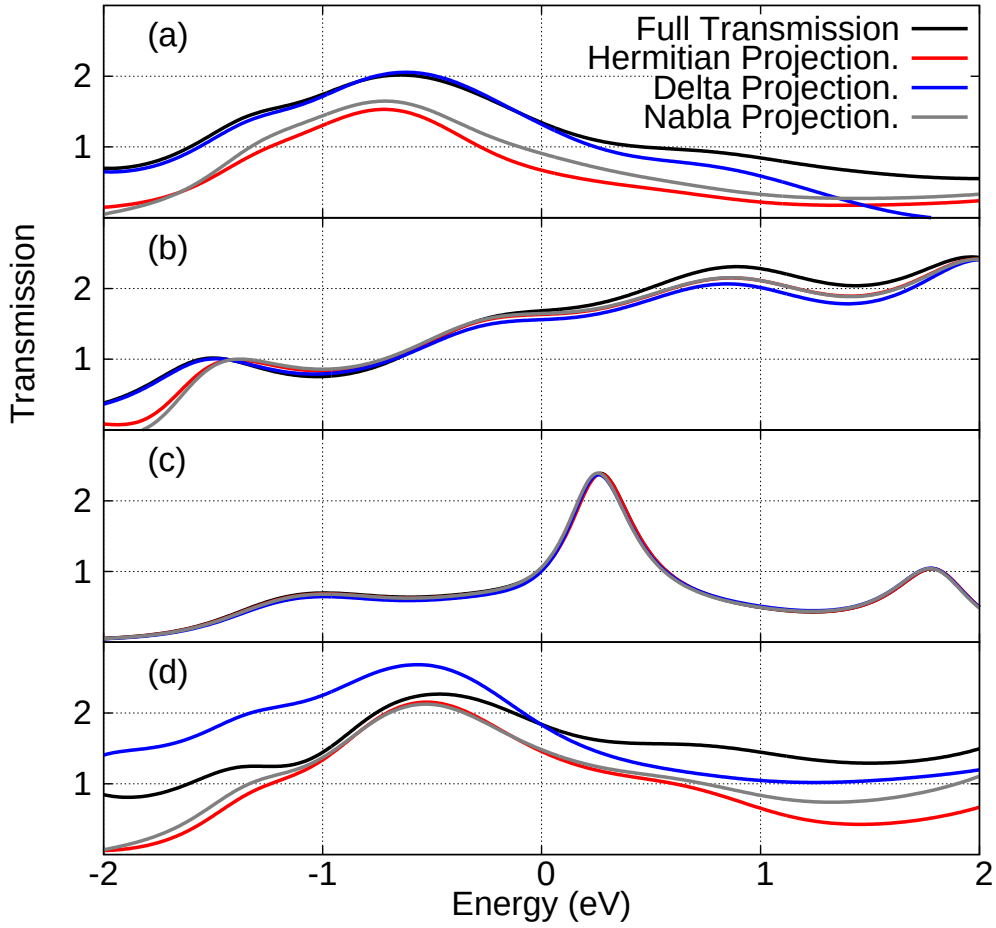

Fig. 3.3: Transmission function for an Al nanocontact as obtained from the full Green's function (black solid line) and from reduced Green's functions with three different projections. Results obtained with the STO-3G** basis set for all atoms are shown in panels (a-c) while results obtained using the 631-G** basis set in the central region are shown in panel (d). The distance between the electrodes increases from (a) [see Fig. 3.2 (a)] to (c) [see Fig. 3.2 (b)] while the atomic structure corresponding to panel (d) is the same as for panel (a).

Part II

II Part: Kondo effect in organic molecules.

Chapter 4

Introduction

4.1 Kondo effect. Brief history.

In 1934, Haas, de Boer and van den Berg observed an anomalous behavior of the resistivity measuring gold metal at low temperatures[15].

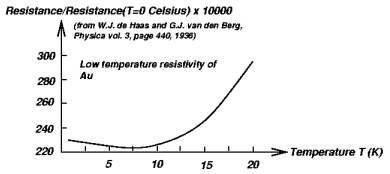

Fig. 4.1: Electric resistance variation with the temperature. Figure taken from [15].

A pure metal exhibits a residual value of the resistivity at low temperature because the electrical resistance usually drops as the temperature decays since the scattering of the electrons, due to the electron-phonon interaction, is reduced when the vibrations of the atoms are small and the electrons travel more easily through the metallic crystal. But gold showed an unexpected increase of the resistivity as we can see in fig. 4.1. This experiment was the first experimental observation of the nowadays well-known Kondo effect, and it is the original historical motivation for studying this problem.

The origin of this anomalous behavior was in the presence of magnetic impurities in the gold studied, as it was experimentally demonstrated in 1962 by Clogson et.al [87] and in 1964 by Sarachik et. al. [88]. These experimental observations had already been predicted by different theorists since the early 50's.

In 1950 Zener proposed the first model describing magnetic impurities in metallic hosts [89]. The essence of this model is that an exchange interaction, J. exists between the spin of the local magnetic impurity and the conduction electrons. This model was followed by Owen [90] and Yoshida [91] between others. In the 1958's Friedel introduced the revolutionary idea at that time that the impurities in a nonmagnetic metal can be described as scattering processes, [92].

Three years after, Anderson proposed his famous model where the impurity was treated as a localized state in the metal, [93]. In the scattering-theory is missed the local electron-electron interactions. But if one considers the fact that a very localized magnetic impurity can act as an atomic level, which induces a narrow resonance around itself due to the hybridization with the conduction electrons of the metal host, it becomes necessary to introduce a Hubbard repulsion term that limits the number of electrons that can hold the

said impurity. In other words the resonance would actually behave like a local moment. To overcome this difficulty, Anderson had the idea to represent the resonance as an additional electronic level inside the conduction band,

$$H = \sum_{\sigma} \epsilon_d \hat{\mathbf{d}}^{\dagger}_{\sigma} \hat{\mathbf{d}}_{\sigma} + \sum_{\mathbf{k}\sigma} \epsilon_{\mathbf{k}} \hat{\mathbf{c}}^{\dagger}_{\mathbf{k}\sigma} \hat{\mathbf{c}}_{\mathbf{k}\sigma} + \sum_{\mathbf{k},\sigma} (V_{\mathbf{k}} \hat{\mathbf{d}}^{\dagger}_{\sigma} \hat{\mathbf{d}}_{\mathbf{k}\sigma} + V^{*}_{\mathbf{k}} \hat{\mathbf{c}}^{\dagger}_{\mathbf{k}\sigma} \hat{\mathbf{d}}_{\sigma}) + U \hat{\mathbf{d}}^{\dagger}_{\sigma} \hat{\mathbf{d}}_{\sigma} \hat{\mathbf{d}}^{\dagger}_{-\sigma} \hat{\mathbf{d}}_{-\sigma} \tag{4.1}$$

Here $\hat{\mathbf{d}}^{\dagger}$, $\hat{\mathbf{d}}$, $\hat{\mathbf{c}}^{\dagger}$ and $\hat{\mathbf{c}}$ are the impurity (d) and conduction electrons creation and annihilation operators respectively. The first and second terms in the above equation are the kinetic energy of the impurity level and the conduction electrons. The last one is a two-level term with a on-site Coulomb repulsion that models the impurity energy levels, and in the middle we can find a hybridization term that couples the conduction electrons with the impurity orbitals.
In this model the Hubbard U, usually called the charging energy, is large and it can impose that there be only one electron occupying the impurity orbital, i.e. $\epsilon_d < \epsilon_F$ and then $\epsilon_d + U > \epsilon_F$. Thus one can find a magnetic moment localized on the impurity. In the mean-field theory, the impurity spectral function, $A_{\sigma}(\omega)$, is described by its Green's Function $G_{\sigma}(\omega) = [\omega - \epsilon_d - \Sigma(\omega)]^{-1}$ as

$$A_{\sigma}(\omega) = -\frac{1}{\pi} \mathrm{Im} G_{\sigma}(\omega), \tag{4.2}$$

where the self energy, $\Sigma(\omega)$, is described by

$$\Sigma(\omega) = \sum_{\mathbf{k}} \frac{|V_{\mathbf{k}}|^2}{\omega - \epsilon_{\mathbf{k}} + i\delta}. \tag{4.3}$$

In the Anderson model, the real part of the Self-energy is omitted because only induces a shift of the impurity level.
Finally in 1964, J. Kondo published his model which gives name to this effect [94]. The goal of Jun Kondo was to consider the scattering from a magnetic impurity that interacts with the spins of the conducting electrons. This scattering induces a spin flip in conduction electrons, anti-ferromagnetically being coupled with the impurity, which come from the hybridization between an orbital with strong on-site repulsion of the impurity and the conduction states, instead by Coulomb exchange. The consequence of this spin fluctuation is the screening of the local spin moment (effectively vanishing), which is a correlated effect that can be written as $U[\hat{\mathbf{n}}_{\sigma} - \langle \hat{\mathbf{n}}_{\sigma} \rangle][\hat{\mathbf{n}}_{-\sigma} - \langle \hat{\mathbf{n}}_{-\sigma} \rangle]$. This screening allows the emergence of a narrow peak at Fermi level in the spectral function, which is the signature of the many-body Kondo ground state. In figure 4.2 we have represented the spectral function in the case of the Anderson model and in the case where the Kondo resonance is presented.
The connection between the Anderson and the Kondo model was exposed by Schrieffer and Wolff in 1966, [95]. The Schrieffer-Wolff transformation is a unitary transformation enabling one to obtain effective low energy physics

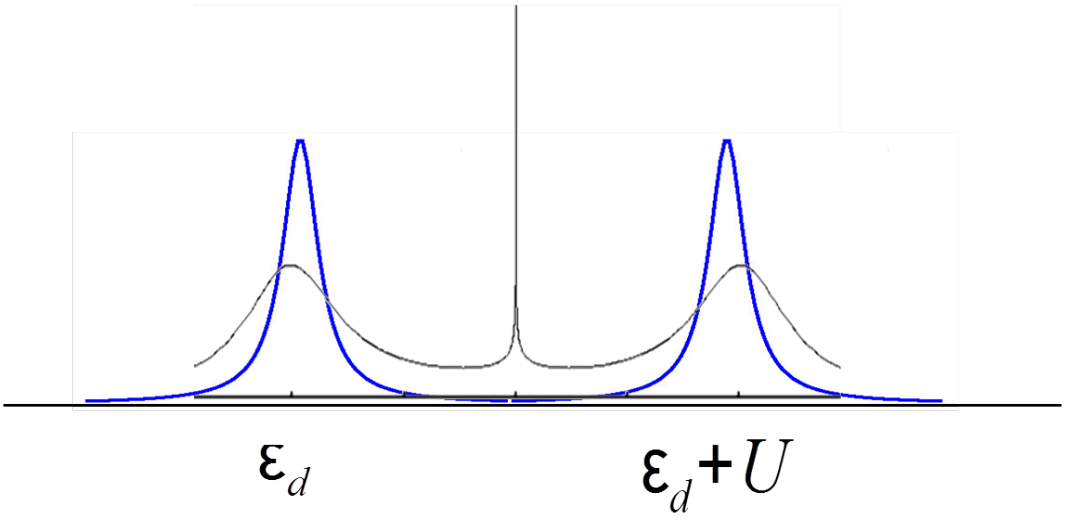

Fig. 4.2: (a) Spectral function of one level Anderson impurity level.

from a given interacting and non-interacting Hamiltonians.

4.2 The Multichannel Anderson model.

The multichannel Anderson impurity model can be written as

$$H = \sum_{d\sigma} \epsilon_d \hat{\mathbf{d}}^\dagger_\sigma \hat{\mathbf{d}}_\sigma + \sum_{\mathbf{k}\sigma} \epsilon_{\mathbf{k}} \hat{\mathbf{c}}^\dagger_{\mathbf{k}\sigma} \hat{\mathbf{c}}_{\mathbf{k}\sigma} + \sum_{\mathbf{k},\sigma} (V_{\mathbf{k}} \hat{\mathbf{d}}^\dagger_\sigma \hat{\mathbf{d}}_{\mathbf{k}\sigma} + V^*_{\mathbf{k}} \hat{\mathbf{c}}^\dagger_{\mathbf{k}\sigma} \hat{\mathbf{d}}_\sigma) + U \hat{\mathbf{d}}^\dagger_\sigma \hat{\mathbf{d}}_\sigma \hat{\mathbf{d}}^\dagger_{-\sigma} \hat{\mathbf{d}}_{-\sigma}. \tag{4.4}$$

This model is solved by both, the non crossing aproximation (NCA) and the one crossing aproximation (OCA) through an expansion in the hybridization strength around the atomic limit. The starting point is an exact diagonalization of the impurity subspace including the Hubbard-type interaction term,

$$H_d = \sum_{d\sigma} \epsilon_d \hat{\mathbf{d}}^\dagger_\sigma \hat{\mathbf{d}}_\sigma + U \hat{\mathbf{d}}^\dagger_\sigma \hat{\mathbf{d}}_\sigma \hat{\mathbf{d}}^\dagger_{-\sigma} \hat{\mathbf{d}}_{-\sigma}. \tag{4.5}$$

The exact diagonalization of the above Hamiltonian gives a collection of many-body states characterized by their energy, E_m. One now introduces auxiliary fields $\hat{\mathbf{a}}_m$ and $\hat{\mathbf{a}}^\dagger_m$ (called pseudo-particles) such that each impurity state is represented by a corresponding pseudo-particle: $\hat{\mathbf{a}}^\dagger_m |PPV\rangle \equiv |m\rangle$ and PPV stands by the pseudo-particle vacuum. The completeness of the impurity eigenstates imposes the following constraint

$$Q \equiv \sum_m \hat{\mathbf{a}}^\dagger_m \hat{\mathbf{a}}_m = 1 \tag{4.6}$$

The physical electron operators $\hat{\mathbf{d}}^\dagger_{d\sigma}$ can now be expressed by the pseudo-particle (PP) operators as

$$\hat{\mathbf{d}}^\dagger_{d\sigma} = \sum_{m,n} (F^{\hat{\mathbf{a}}^\dagger})_{m,n} \hat{\mathbf{a}}^\dagger_n \hat{\mathbf{a}}_m \tag{4.7}$$

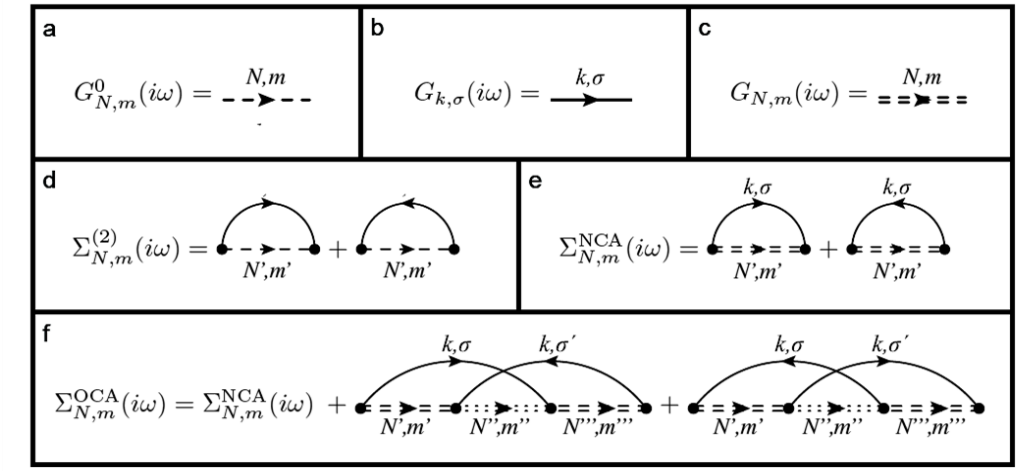

Fig. 4.3: Diagrams for pseudo-particle self-energies in the NCA and OCA for some pseudo-particle m.

where $(F^{\hat{\mathbf{a}}^\dagger})_{m,n} \equiv \left\langle n|\hat{\mathbf{d}}^\dagger_{d\sigma}|m\right\rangle$ are the matrix elements of the impurity-electron creation operator. For later convenience we also de?ne the corresponding matrix elements of the impurity-electron destruction operator as: $(F^{\hat{\mathbf{a}}^\dagger})_{m,n} \equiv \left\langle n|\hat{\mathbf{d}}^\dagger_{d\sigma}|m\right\rangle$. The anti-commutation rules for the physical electron operators then require that the PP $\hat{\mathbf{d}}_m$ is a boson (fermion) if the corresponding state $|m\rangle$ contains an even (odd) number of electrons. In the PP representation we can now rewrite the Hamiltonian of the generalized Anderson impurity model as follows:

$$\begin{aligned} H = &\sum_m E_m \hat{\mathbf{a}}^\dagger_m \hat{\mathbf{a}}_m + \sum_{\mathbf{k}\nu} \epsilon_{\mathbf{k}\nu} \hat{\mathbf{c}}^\dagger_{\mathbf{k}\nu} \hat{\mathbf{c}}_{\mathbf{k}\nu} + \\ &\sum_{\mathbf{k}\nu,m,n} V_{\mathbf{k}\nu d} \hat{\mathbf{c}}^\dagger_{\mathbf{k}\nu} \hat{\mathbf{a}}^\dagger_m (F^d)_{m,n} \hat{\mathbf{a}}_n \hat{\mathbf{d}}_\sigma + H.c. \end{aligned} \tag{4.8}$$

where we have included the constraint $Q \equiv 1$ into the Hamiltonian.
The NCA diagrams describe processes where a single electron (hole) jumps from the bath to the impurity and back thereby temporarily creating a PP with $N+1$ ($N-1$) electrons. The NCA equations correspond to a self-consistent perturbation expansion to lowest order in the hybridization function. Since the fermionic self-energies depend on the dressed bosonic propagators, and vice versa, the NCA equations have to be solved self-consistently. Once the NCA equations are solved the physical quantities can be calculated from the PP self-energies. The OCA takes into account second order diagrams where two bath electron lines cross as shown in Figure 4.3. The self-energies for the PP's again depend on the full propagators of other PP's, and hence the OCA equations also have to be solved self-consistently.

4.3 Molecular Kondo Model from first principle calculations

In this section we will introduce the molecular Kondo model developed in this thesis. To undertake this we will use a toy model of few levels to explain the most important and complex aspects of our approach.

The first thing to keep in mind to try this model is that we go to work with complex systems. These systems are molecules that are either adsorbed on a metal surface, and are observed using an STM tip, or they are contacted through a pair of metal electrodes.

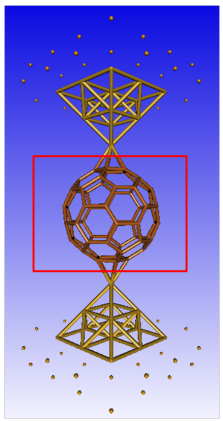

Fig. 4.4: Picture C60 molecule attached to gold electrodes. Floating points represent the Bethe lattice.

Our first approach is to do a DFT calculation of the system to obtain the ground state. This calculation is performed by solving the Kohn-Sham Hamiltonian with our ANT.G code [59]. The way of working of ANT.G is as follows. We built a cluster that integrates both the molecule and a representative portion of the metal or electrodes. This cluster is then embedded in a tight-binding network to simulate a semi-infinite system, usually called the Bethe lattice. In Figure 4.4 we show a model representation of this cluster, including the Bethe lattice. This system is solved with a DFT level of theory thanks to the ANT interface with Gaussian [53]. The Bethe lattice is attached to the cluster via a self-energy. The effective Hamiltonian of the full system is thus defined by

$$\mathbf{H}^{eff} = \mathbf{H}^{KS} + \mathbf{\Sigma}_{tb,R} + \mathbf{\Sigma}_{tb,L}. \tag{4.9}$$

Here $\mathbf{H}^{KS}$ is the Kohn-Sham Hamiltonian obtained from Gaussian, $\mathbf{\Sigma}_{tb,R}$ and $\mathbf{\Sigma}_{tb,L}$ are the self-energy due to the Bethe lattice in one and another electrode (right and left). As we have emphasized in the figure 4.4 with a red box, the molecule is confined spatially. In first approximation, all the atoms that are part of the molecule of interest constitute the active space, and hence our first step always is to project the above described effective Hamiltonian onto the cited molecular space. To do this we use partitioning techniques through projectors operators that we have developed in this thesis and explained in chapter 3.

Projecting onto the molecular sub-space gives us a reduced effective Hamiltonian,

$$\mathbf{H}^{\Delta}_{M} = \mathbf{H}^{KS}_{M} + \mathbf{\Sigma}^{\Delta}_{M}, \tag{4.10}$$

where $\mathbf{H}^{\Delta}_{M}$ is the representation of $\hat{\mathbf{P}}^{\dagger}_{M}\hat{\mathbf{H}}\hat{\mathbf{P}}_{M}$ in the block orthogonal metric described in section 3.5, and $\mathbf{\Sigma}^{\Delta}_{M}$ is the self-energy defined in Eq. 7.1 as

$$\mathbf{\Sigma}^{\Delta}_{\mathrm{M}} = (\omega - \mu)\,\mathbf{S}_{\mathrm{M}} - \mathbf{H}_{\mathrm{M}} - \mathbf{S}_{\mathrm{M}}[\mathbf{G}_{\mathrm{M}}]^{-1}\mathbf{S}_{\mathrm{M}}. \tag{4.11}$$

To obtain the energies of the molecular levels, ϵ, we need to solve the generalized eigenvalue equation $\mathbf{H}^{\Delta}_{M}\mathbf{X} = \epsilon\mathbf{S}^{\Delta}_{M}\mathbf{X}$, where $\mathbf{S}^{\Delta}_{M}$ is the

representation of the projection onto the molecular sub-space of the identity operator in the block-diagonal metric. The transformation matrix, $\mathbf{X}$, is the matrix of the eigenvectors. The molecular wave functions, ψ, are thus described by

$$\psi_\alpha = \sum_i X_{\alpha i}\phi_i, \tag{4.12}$$

which obey $\langle\psi_\alpha|\psi_\beta\rangle = \delta_{\alpha\beta}$, i.e. the molecular representation is an orthogonal basis set. Here ϕ are the atomic orbitals. Notice that the eigenvectors matrix is a overlap matrix between the molecular and the atomic orbitals which can be represented as $X_{\alpha i} = \langle\psi_\alpha|\phi_i\rangle$. Hence we can rewrite the molecular Hamiltonian in the eigenvalue basis set of the Hamiltonian by performing a basis change in the self-energy,

$$\mathbf{\Sigma}^{\psi}_{\mathrm{M}} = \mathbf{X}^{\dagger}\mathbf{\Sigma}^{\Delta}_{\mathrm{M}}\mathbf{X}^{\dagger}. \tag{4.13}$$

And then, the molecular Hamiltonian is finally described by

$$\mathbf{H}^{\psi}_{M} = \epsilon^{KS}_{M} + \mathbf{\Sigma}^{\psi}_{M}. \tag{4.14}$$

Note that although ϵ^{KS}_{M} is diagonal, $\mathbf{\Sigma}^{\psi}_{M}$ is not. We can advance that the imaginary part of this molecular self-energy is the molecular hybridization, which plays an important role in the Kondo physics.

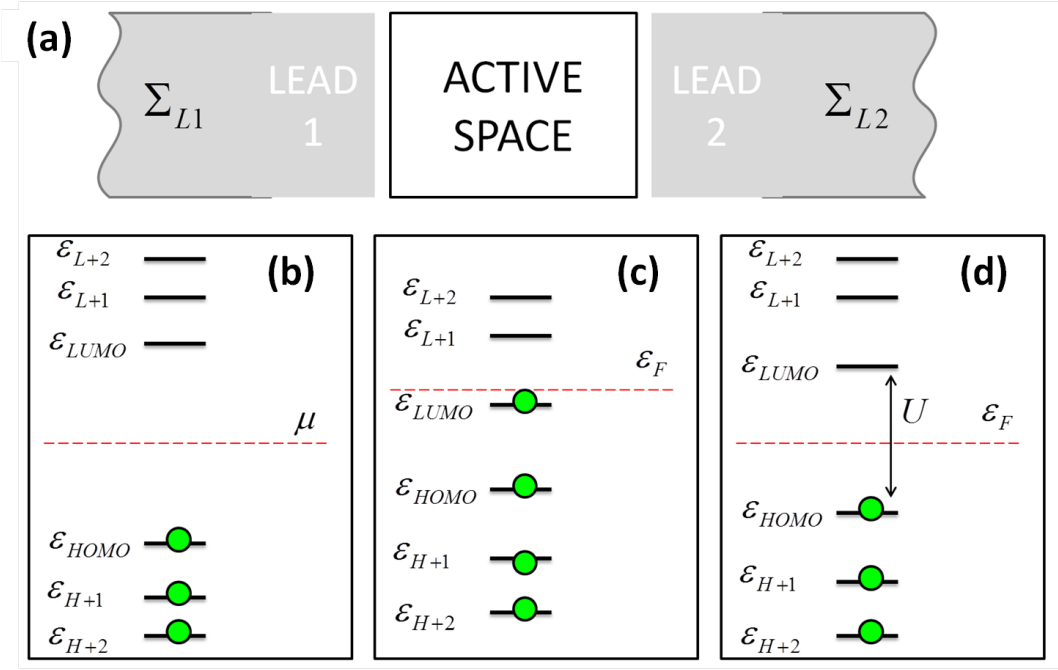

Fig. 4.5: (a) Schematic picture of a molecule embedded in a metal host. (b-d) Toy model of Molecular electronic levels. (b) The normal isolated molecular spectrum. (c) Typical molecular spectrum contacted with or absorbed on a metal host. Notice that we are representing a situation in which the molecule received charge from the metal. (d) Resulted molecular spectrum after treatment.

In figure 4.5 (a) we have represented a Schematic representation of this active space. One problem after diagonalized the Hamiltonian is that we can find a lot of molecular orbitals, as many as basis functions has the molecule. So determining the physically relevant active space to the Kondo problem can be a real headache, which is further complicated if we have also broken the spin

symmetry to include the magnetic moment.
If we have an apparently simple system where the ground state of the isolated molecule is non-magnetic, the determination of the active space can be made very easily selecting the molecular levels around the Fermi level of the metal host. For example, in figure 4.5 (b) we have represented the eigenvalues of an isolated molecule. The eigenvalues are the energy of the molecular levels. In figure 4.5 (c) we have plotted the same in the case that the molecule is attached or embedded in a metal host. As shown by the fact that the LUMO is below the Fermi level of the metal, we are assuming a charge transfer from the metal host to the molecule. In this toy example, the active space interesting for the Kondo problem could be in itself this orbital, the LUMO, which would constitute the impurity level. From now, we will reduce the active space to this unique orbital, since it is the only relevant molecular level. Notice that the partition is immediate because the eigenvalues basis set of the Hamiltonian is diagonal.
To solve the Kondo problem we need to include three fundamental quantities that will be used as input in our impurity solver. These are the hybridization, advanced in Eq. 4.13, the energy of impurity level and the electron-electron interactions. Our objective is to obtain these quantities from a DFT calculation, but we must bear in mind that the first step of the impurity solver is an exact diagonalization which aimed firstly to correctly enter the Coulomb interactions, and secondly to generate the pseudoparticles basis set, described in Section 4.2. So considering that the first objective of the exact diagonalization is the introduction of interactions, our next step should be to eliminate themselves that we have introduced in the density functional through the Hartree potential. This is what is known as the double counting correction. The simplest approach to the double counting correction is

$$\mathbf{H}_{dc} = \sum_i \frac{U}{2} n_i(n_i - 1) - \sum_i \frac{J}{2}(n_i^{\sigma}(n_i^{\sigma} - 1) + n_i^{-\sigma}(n_i^{-\sigma} - 1)). \tag{4.15}$$

Here n_i is the number of electrons in the active space. However, this equation is not useful for molecular systems, (or in general any equations derivatives thereof), since the parameters U and J are unknown. For this reason we have proposed to use CDFT techniques to empty the active space, and thus eliminate the electronic interaction of these molecular levels. In our model this functional is given by

$$\begin{aligned} E[n(\mathbf{r}), V_{\mathrm{M}}, \mu] = E[n(\mathbf{r})] + V_{\mathrm{M}} \left(\int \omega_{\mathrm{M}}(\mathbf{r}) n(\mathbf{r}) d\mathbf{r} - N_{\mathrm{M}} \right) + \\ \mu \left(\int (1 - \omega_{\mathrm{M}}(\mathbf{r}) n^0(\mathbf{r}) d\mathbf{r} + \int \omega_{\mathrm{M}}(\mathbf{r}) n(\mathbf{r}) d\mathbf{r} - Q \right). \end{aligned} \tag{4.16}$$

The weighting factor ω_{M}, in the simplest case, is 1 in the volumetric region of the molecule and 0 elsewhere, N_{M} is the charge in the molecule (constrained to be integer), and V_{M} the Lagrange multiplier or potential that ultimately controls this charge. For completeness of notation we have included the term that controls the overall charge of the system, Q. This number is chosen in such a way that the charge in the electrodes remains the same as that of the

ground state calculation. As we will explain in detail in Chapter 7, we choose to freeze the electron density of the electrodes (thereof the presence of $n^0(\mathbf{r})$ in Eq. 4.16) and find in a self-consistent manner only the projected density of the molecule $n(\mathbf{r})_{\mathrm{M}}$ and the projected constrained Hamiltonian $\mathbf{H}_{\mathrm{M}}^{-}$ to have $N_{\mathrm{M}}(< Q_{\mathrm{M}})$ electrons.
In figure 4.5 (d) we have schematically represented the screened molecular gap due to the metal host, and the result of diagonalize $\mathbf{H}_{\mathrm{M}}^{-}$. It is a well known problem that the Kohn-Sham eigenvalues underestimate the gap, and these values must be corrected to obtain the actual value of the charging energy. In the next section we discuss this phenomenon.
Finally we will discuss how to select the molecular level when the molecule is magnetic.

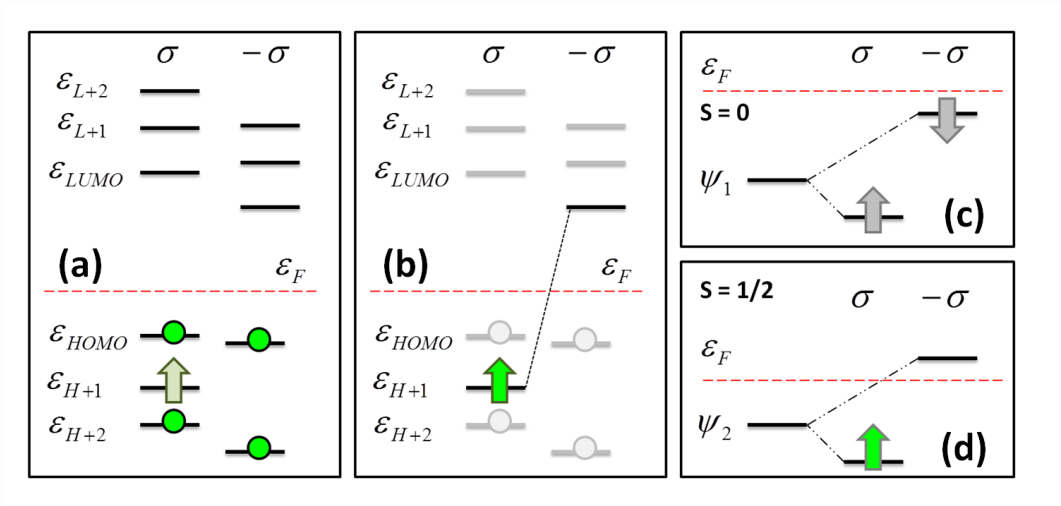

Fig. 4.6: Toy model of the electronic molecular levels in the case of magnetic molecules. (a) Schematic picture of a magnetic molecule embedded in a metal host. (b) Connection between the σ and $-\sigma$ levels by the inner product. (c-d) A way to understand the magnetic molecular levels by the inner product. (c) non-magnetic case, (d) magnetic case.

When the molecule has a magnetic ground state, the determination of the relevant molecular orbitals is complicated. First, as shown in the figure 4.6 we have double molecular levels due to the spin broken symmetry. Unrestricted DFT calculations compute the different spin orientations independently, so that the dimension of our space is doubled. The magnetic moment can be readily determined by the difference between the occupancy of spin in one direction and the other, $S = n_\sigma - n_{-\sigma}$, but is more difficult to find the original molecular orbitals, without spin broken symmetry, which have led to this magnetic moment.
In an unrestricted DFT calculation the original wave function ψ_i is split into to different spin dependent wave functions ψ_j^σ and $\psi_k^{-\sigma}$. The problem is that the eigenvalues are also split, and does not exit a direct relationship between the sub-index i,j and k, i.e $i \neq j \neq k$. However we can establish a relationship between these subscripts through the inner product of the spin dependent wave functions, $\langle \psi_j^\sigma | \psi_k^{-\sigma} \rangle$. By definition,

$$\langle \psi_j^\sigma | \psi_k^{-\sigma} \rangle = 1, \tag{4.17}$$

if j and k come from the same wave function i, and

$$\left\langle \psi_j^{\sigma} | \psi_k^{-\sigma} \right\rangle = 0, \tag{4.18}$$

otherwise. This is schematically represented in figure 4.6 (b). An additional problem is that after the self-consistent processes the atomic contribution of the spin dependent molecular orbital can change. As a result, we can find several molecular levels that are a mix of original wave functions, allowing them to appear at different energies, so in many cases the value of the inner product is < 1, which complicates the search. In this case, one must also make a careful analysis of the contribution of the atomic orbitals to the wave function, as discussed in the following chapters.
Once found the spin dependent wave functions pairs, determining the magnetic molecular orbital is trivial. As is shown in Figure 4.6 (c), if the eigenvalues of both spin components of the same wave function are below the Fermi level, the resulting molecular orbital is non-magnetic, and may be considered doubly occupied. In contrast, if both are above the Fermi level, the molecular orbital can be considered empty. Finally, if the spin dependent wave functions pairs are located crossing the Fermi level as is shown in the figure 4.6 (d), we can consider that we have a magnetic moment derived from this orbital.

4.4 The concept of charging Energy

Whenever we have a Kohn-Sham Hamiltonian of a semiconductor, such as an organic molecule, we have a problem in their eigenvalues due to the discontinuity derivative problem, i.e. we underestimate the gap (or the band-gap) of the system whose origin is in the dependence of the exact energy functional upon the number of electrons; in addition to the inherent self-interaction problem due to the uncompensated Coulomb interaction. So it is hard not to consider how will we use these eigenvalues for our model? In this section we propose a self-consistent correction implemented in our ANT.G code [59] to correct this problem.
The energy functional described in chapter 1 gives the next value of total energy:

$$E = \sum_{i}^{N} \epsilon_i - V_H[n(\mathbf{r})] + E_{XC}[n(\mathbf{r})] - \int \frac{\delta E_{XC}[n(\mathbf{r})]}{\delta n(\mathbf{r})} n(\mathbf{r}) d\mathbf{r}. \tag{4.19}$$

This energy evolves in a continuous quadratic form with the total charge of the system. This is shown in Figure 4.7 (a) [96]. The problem is precisely the continuity, since the derivative of the energy with respect to the charge must be discontinuous for every integer value, as is also shown in Figure 4.7 (a) in red [96]. In other words, the derivative of the functional energy must be constant for any fractional value of charge between two consecutive integers. The origin of this error lies precisely in the construction of the density functional, because while this discontinuity is introduced into the kinetic term, resulting in the infamous Kohn-Sham gap, i.e. $E_g^{KS} = \epsilon_{LUMO} - \epsilon_{HOMO}$, not

done properly in the exchange-correlation term. (The remaining terms, do not present discontinuity and may be excluded from this analysis).

$$E_g = \left|\frac{\delta T}{\delta n(\mathbf{r})}\right|_{N+\delta} - \left|\frac{\delta T}{\delta n(\mathbf{r})}\right|_{N-\delta} + \left|\frac{\delta E_{xc}}{\delta n(\mathbf{r})}\right|_{N+\delta} - \left|\frac{\delta E_{xc}}{\delta n(\mathbf{r})}\right|_{N-\delta} = E_g^{KS} + E_g^{xc} \quad (4.20)$$

The charging energy is a correction to the functional that allows us to enter the discontinuity in the derivative of the energy functional due to exchange term. This is shown in figure 4.7 (b).

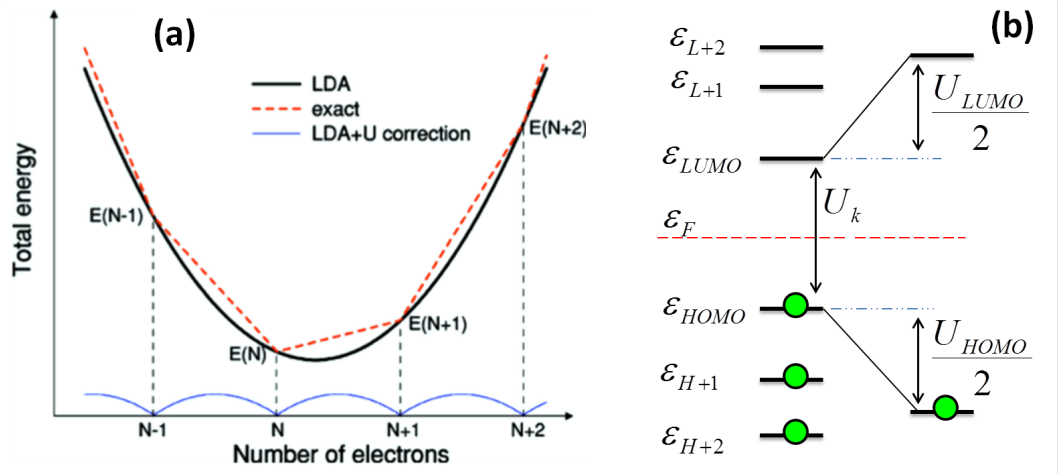

Fig. 4.7: (a) Sketch of the total energy profile as a function of number of electrons in a generic atomic system in contact with a reservoir. The bottom curve is simply the difference between the other two (the LDA energy and the âexactâ result for an open system). Picture taken from [96]. (b) Sketch picture of the gap problem and the Janak's theorem correction [58, 97].

Inspired by the Cococcioni and Louie works between others [58, 96], we decided to make a correction on our functional using the DFT+U theory. So, taking advantage of the fact that we are emptying our system to eliminate the double counting, we decided to compute the charging energy through the Cococcioni's definition [96] via the Lagrange multiplier introduced in the constrained-DFT.

$$U = \frac{\delta V_M^0}{\delta n} - \frac{\delta V_M}{\delta n} = (\chi_o)^{-1} - (\chi)^{-1}. \quad (4.21)$$

Here V_M^0 is the Lagrange multiplier on the Hamiltonian of the ground state after empty the active space. This term is easily obtained from the first iteration cycle in the emptying calculation. The screening by the metal host can be obtained as the inverse of the former term in the above equation, χ_o. This screening does not include the effects in the hybridization changes. These effects are included in the second term which is the Lagrange multiplier after the self-consistent process. Note that since we are blocking the metal host density this screening arises only from the ground state of the metal host, and not include any response due to the change in the charge of the active space. The correction in the density functional is also a cuadratic term which can be written as

$$E[n(\mathbf{r})] = E^{DFT}[n(\mathbf{r})] + \frac{U}{2} n(1-n). \quad (4.22)$$

The derivative of this functional is

$$\frac{\delta E[n(\mathbf{r})]}{\delta n} = \frac{\delta E^{DFT}[n(\mathbf{r})]}{\delta n} + \frac{U}{2} - Un, \tag{4.23}$$

which obeys that

$$\frac{\delta^2 E[n(\mathbf{r})]}{\delta n^2} = 0, \tag{4.24}$$

and hence

$$\frac{\delta^2 E^{DFT}[n(\mathbf{r})]}{\delta n^2} = U. \tag{4.25}$$

By the Janak's theorem [97] we can rewrite this equation in terms of the eigenvalues of the Kohn-Sham Hamiltonian which allows us to correct our eigenvalues in the following way

$$\epsilon_i = \epsilon_i^{KS} - \frac{U}{2} n_i^e + \frac{U}{2} n_i^h. \tag{4.26}$$

Here n_i^e is the number of electrons in the i-orbital, and n_i^h is the number of holes, ($n_i^h = 1 - n_i^e$). Thus, the above expression takes into account a correction to any orbital by it charge density. In the limit, for example, of completely full HOMO or completely empty LUMO, this equation gets the correction proposed by Louie [58],

$$\epsilon_{HOMO} = \epsilon_{HOMO}^{KS} - \frac{U}{2}, \tag{4.27}$$

$$\epsilon_{LUMO} = \epsilon_{LUMO}^{KS} + \frac{U}{2}. \tag{4.28}$$

We have implemented this procedure self-consistent in ANT.G following

$$U_{SCF} = \frac{\delta V_M^{i=1}}{\delta n} - \frac{\delta V_M^{i>1}(U_{i-1})}{\delta n} = (\chi_o)^{-1} - (\chi)^{-1}, \tag{4.29}$$

where we have obtained the final correction computing the U in each cycle of the calculation until convergence of the energy. Here i stand by the number of cycles. We have plotted an schematic picture of that in figure 4.7 (b), where $U_k = E_g^{KS}$.

Chapter 5

The Kondo effect in Manganese Phthalocyanine on Bi(110).

5.1 The Manganese Phthalocyanine.

The phthalocyanines are organic molecules with a metal transition atom in the center of its structure. The unique planar structure of these molecules, with a number of carbon atoms where electrons are confined and delocalized at the same time, gives them amazing electronic properties. Because of this, they have attracted much attention in recent years due to their potential applications in the field of molecular electronics and organic photovoltaics. In addition, the metal atom in the center of the structure gives them a magnetic moment, making therefore also interesting for molecular spintronics. This magnetic moment depends on which is the central atom.

In this thesis we are interested in the Manganese Phthalocyanine (MnPc), showed in figure 5.1, which has the highest magnetic moment of the more studied range of the first transition series, with $S = 3/2$. It is followed by the FePc ($S = 1$), the CoPc ($S = 1/2$), the NiPc ($S = 0$) and finally, by the CuPc ($S = 1/2$). In all of these molecules have been observed the Kondo effect over the last decade [25, 26, 98–101]. (citar todos los papers pertinentes, y comentar los más relevantes). But what makes it really interesting from a theoretical point of view is the versatility of magnetic states of high and low spin that may arise, and the fact that this spin state can change when they are deposited on a metal surface. Especially since these systems allow studying different kind of Kondo physics such as ligand Kondo, orbital Kondo, mixed valenced regimen or the underscreened Kondo effect.

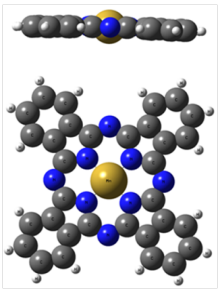

Fig. 5.1: Picture of the Manganese Phthalocyanine. In gray carbon atoms; in blue Nitrogen atoms; in yellow central manganese atom and in white hydrogen atoms.

The MnPc is a coordination complex with manganese center. The exchange-induced magnetic moment of the Mn atom can be as high as $S = 5/2$, but the strong coupling to the organic ligand usually quenches the spin into lower values [102]. The MnPc has three unpaired electrons localized on the d-orbitals

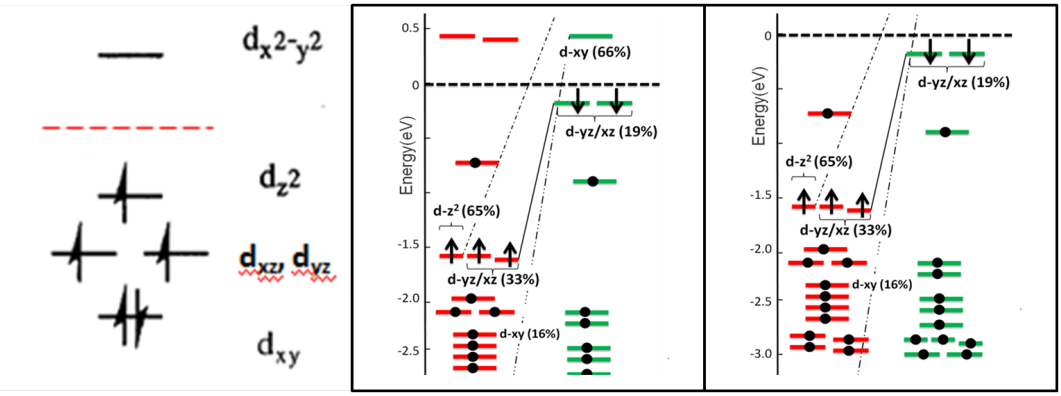

Fig. 5.2: (a) Schematic diagram of the MnPc d-orbitals energy levels due to the crystal field. (b) The MnPc molecular orbitals around the chemical potential computed with DFT using a simple basis set. (c) The same in (b) but with a double basis set.

of the central manganese atom with a $S = 3/2$ total magnetic moment. The simplest image of the distribution of these electrons in the d-orbitals is given by the splitting due to the crystal field. (See figure 5.2 (a)). This image is also known as point charge approximation [103, 104]. Moreover this simplified picture of the d-orbitals, embedded in an organic ligand, is not enough to capture the nature of the molecular orbitals in these kind of molecules, as we can see in the DFT spectrum showed in figure 5.2 (b) and (c). The d-orbitals of the manganese atom are hybridized with the orbitals of the organic ligand, forming a complex network of molecular orbitals. Hence, identifying the d-orbitals such as molecular orbitals is not realistic at all.

The electronic structure of MnPc showed in figure 5.2(b,c) has been computed in the framework of DFT via our ANT.G code [59] which interfaces with GAUSSIAN [53]. We have used a standard exchange-correlation functional in the generalized gradient approximation[33, 35]. We have employed a minimal STO-3G basis set in the case (b) and a LANL2DZ double basis set in the case (c). In this kind of calculations the molecular orbitals are described as a linear combination of atomic orbital (LCAO approximation, equation: 1.26), which directly are the eigenvectors of the Hamiltonian in the non-orthogonal basis set. In the picture we have plotted the eigenvalue of the Hamiltonian in the molecular representation described in section 4.3.

As shown in figure 5.2 (b) the high occupied molecular orbital (HOMO) of up electrons is an extended molecular orbital formed by the p-orbitals of the organic ligand of the phthalocyanine (C and N atoms). In contrast, the HOMO of down electrons belongs to d-orbital of manganese atom in a 36 %. These two molecular orbitals show the complexity of study the electronic structure of this molecule. In figure 5.3 we have written the partial electronic charge of the d-orbitals and its spin state. We have used the Mulliken partition explained in chapter 3.

It is well known that a minimal basis set DFT calculation is not always enough accurate to compute the electronic structure of this kind of systems. Because of this, we wanted to compare a calculation with minimal basis with one double base, to highlight the complexity of the problem with the growth of the base.

Orbitals	Occupation	Magnetic moment
d_{z^2}	1.03	**0.90**
d_{xz}	1.47	**0.46**
d_{yz}	1.13	**0.82**
$d_{x^2-y^2}$	0.83	0.14
d_{xy}	1.07	**0.90**

Fig. 5.3: Partial electronic charge and spin state in the d-orbital of the Manganese atom

5.2 Experimental Motivation.

Although we studied the electronic and magnetic properties of phthalocyanines on surfaces, the experimental motivation of this part of this thesis is the Berlin J.I. Pascual's group experiments [26], with who we had the pleasure of collaborate.

The first experimental observation of Kondo effect in the MnPc was in 2007 [99] by Fu et.al. (fig. 5.4), where the molecule was deposited on a Pb(111) surface. The measure of Kondo-type resonances in this experiment is indisputable, but the origin of this resonance was incorrectly assigned to a one-half spin state. In 2011, Kranke et.al. [25] measured this system again, already considering, the origin of the Kondo-type resonance at a high spin state of the MnPc. We will discuss this system in the next chapter.

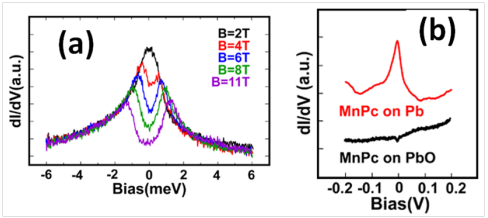

Fig. 5.4: Experimental observation of Kondo resonance in MnPc on lead surface (a) and (b) images are taken from [99]. .

Metal-phthalocyanines usually present a local reactive site in the metal atom of their structures because this atom is unsaturated (can accept more bonds). Because control over the magnetic moment of molecules and its interaction with a substrate is a key issue in the emerging field of molecular spintronics [105], the axial coordination, for example, of small molecules like CO, NO or O_2 to this center is very interesting since it can enable them act such as sensors [106, 107]. From a experimental point of view, that opens a unique possibility of controlling the magnetic moment in-situ by external chemical stimuli [108–114].

When we started this collaboration, previous studied had shown how, for example, that the attachment of NO molecule to a cobalt-tetraphenylporphyrin (CoTPP) quenches its spin due to the oxidation process [112]. However the general picture is more complicated, as the chemical bond to the reactant molecule causes the redistribution of charge in the *d*-orbitals of the metal center and modifies the ligand field of the metal ion. This has critical consequences for the magnetic ground state of the complex [113, 114].

On metal surfaces, the formation of a new ligand bond may additionally alter the hybridization of molecular and substrate states, thus affecting the electronic and magnetic coupling of the metal ion to the substrate [109–111]. Understanding the response of these effects to the change in chemical coordination

is crucial to gain the full control over the functionality of the magnetic system. Pursuing this goal, few years ago, A. Stróżecka and J.I. Pascual measured zero bias anomalies in a MnPc and a CO-MnPc molecules deposited on a Bismuth surface. Notice that although now it has already been observed in repeated occasions [25, 26, 98, 99], at that time was not expected to get Kondo effect in systems such as MnPc due precisely to its high magnetic moment. Furthermore, it should to take into account that bismuth has the highest spin-orbit interaction of the periodic table, and today understanding the interaction of a magnetic impurity in the presence of a strong spin-orbit field remains challenging.

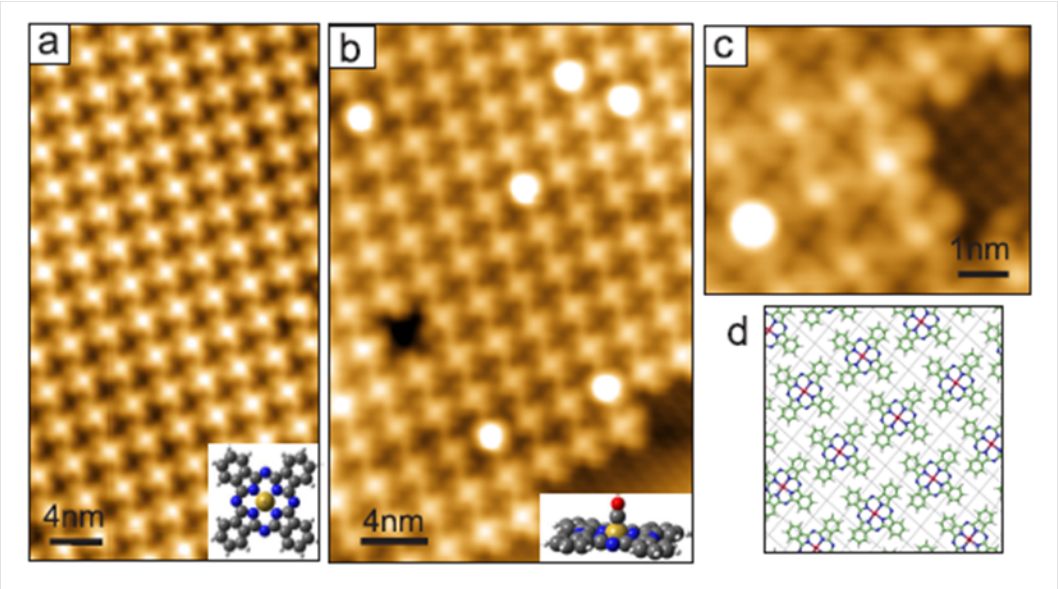

Fig. 5.5: Adsorption of MnPc and CO-MnPc on Bi(110). (a) STM image of highly ordered MnPc island (I=0.2 nA, V=250 mV). (b) MnPc island after exposure to CO (I=0.1 nA, V=180 mV). CO-coordinated molecules can be distinguished by different apparent height. Inset images in (a) and (b) show schematic pictures of the chemical structure of MnPc and CO-MnPc. (c) High resolution STM image of bare and CO-ligated MnPc (I=0.1 nA, V=-250 mV). (d) Adsorption model of MnPc on Bi(110).

The experiments were performed in a custom-made scanning tunneling microscope working in ultrahigh vacuum at low temperature (5 K). Atomically clean Bi(110) single crystal surface was exposed at room temperature to a flux of MnPc molecules (Sigma-Aldrich) thermally sublimed from a crucible. As shown in Figure 5.5 (a), on this surface MnPc molecules self-assemble in densely packed islands [115]. Each of MnPc molecules appears as a clove-like protrusion, its bright center corresponding to the metal ion. Exact adsorption configuration could be established by resolving simultaneously intramolecular structure of MnPc and atomic structure of the underlying substrate (see e.g. Fig. 5.5 (c)). Bi(110) is a pseudocubic surface of a bilayer-structure, with an almost square unit cell containing two atoms [116]. One of the atoms binds to the underlying layer; the other atom presents a dangling bond which is resolved in the STM images. As shown schematically in Fig. 5.5 (d), MnPc adsorbs on Bi(110) so that Mn ion is located directly above the dangling bond of the substrate. This specific adsorption configuration indicates that the bonding between MnPc and Bi(110) is dominated by the direct interaction between the

metal atom and the dangling bond of the bismuth atom.
The MnPc covered sample was subsequently cooled down to 130 K and exposed to CO gas partial pressure of 10^{-7} mbar for 90 s. After CO exposure the structure of the molecular islands remains unchanged, but several molecules (∼10%) exhibit now larger apparent height (Fig. 5.5 (b)). We identify these new molecules as CO-ligated MnPc. Figure 5.5 (c) shows a high resolution STM image of the new species embedded in the MnPc island. Similarly to MnPc, the CO-coordinated molecules exhibit fourfold symmetry, with a central protrusion appearing 0.8 Å higher than in case of MnPc, indicating that a single CO molecule bonds directly to the transition metal ion. We find only singly coordinated CO-MnPc, contrary to previously studied doubly coordinated porphyrin molecules [117, 118].

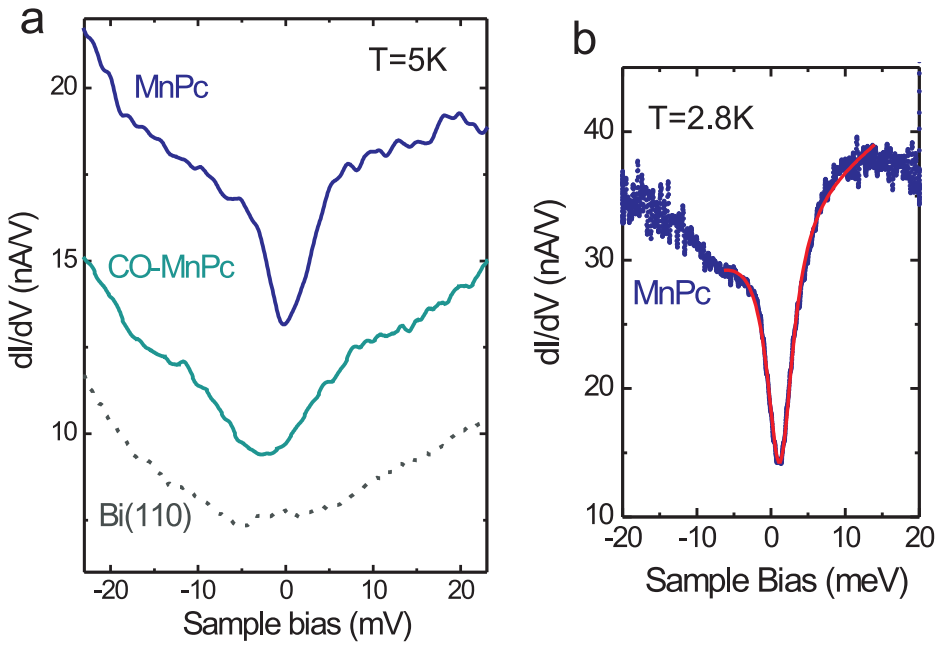

Fig. 5.6: (a) dI/dV spectra of MnPc and CO-coordinated MnPc in the bias range close to E_F, showing the zero bias anomaly. The dotted spectrum is the reference curve on bare Bi surface. (b) Zero-bias feature of MnPc measured at reduced temperature T=2.8 K. The feature exhibits clear Fano line shape. Continuous line (red) corresponds to the fit by Fano equation.

The differential conductance spectra (dI/dV) measured close to E_F reveals a pronounced anomaly at zero bias with a dip-like line shape on MnPc (Fig. 5.6 (a)). We interpreted it as a fingerprint of the Kondo effect, as it was observed before for MnPc and FePc on metal surfaces [25, 99, 119]. The zero-bias features exhibit a clear Fano line shape (Fig. 5.6 (a) and (b)), commonly observed for Kondo ground states of magnetic adsorbates [120]. Other possible effects which could cause this anomaly, as e.g. inelastic spin flip excitation, were carefully excluded by studying the temperature dependence of the line shape. A Kondo temperature of $T_K^{MnPc} = 22 \pm 6$ K can be approximated from a fit to the anomaly's line shape, (Fitting by Fano equation. Thermal and instrumental broadening was removed).
When similar spectra were measured on CO-MnPc molecules, the anomaly appears much broader, with a slightly different lineshape (Fig. 5.6 (a)). The

broadening of the Fano resonance indicates that coordination of CO modifies the magnetic state of the molecule. This modification is reversible and can be controlled by selective removal of CO molecules using STM tips. In order to detach an individual CO from its site, the STM tip was placed over CO-MnPc molecule, feedback loop was opened and the sample bias was ramped. A resulting current-voltage characteristics is shown in Fig. 5.7 (a). A sudden drop of the tunneling current at a certain threshold voltage indicates the detachment of the CO molecule from its coordination site (in the most cases to a new site in a neighbor MnPc molecule). The resulting species recovers the usual clove-like shape and a narrower zero bias anomaly characteristic of a bare MnPc molecule (Fig. 5.7 (c)). To establish the underlying mechanism of CO detachment the experimentalists noted that the threshold voltage increases linearly with the distance between the tip and the molecule, as shown in Fig. 5.7 (b). This behavior indicates that the desorption of CO is induced by the electric field at the tunnel junction. The critical value of electric field, $\varepsilon \cong 1\,\mathrm{V/nm}$ can be extracted from the slope of the line.

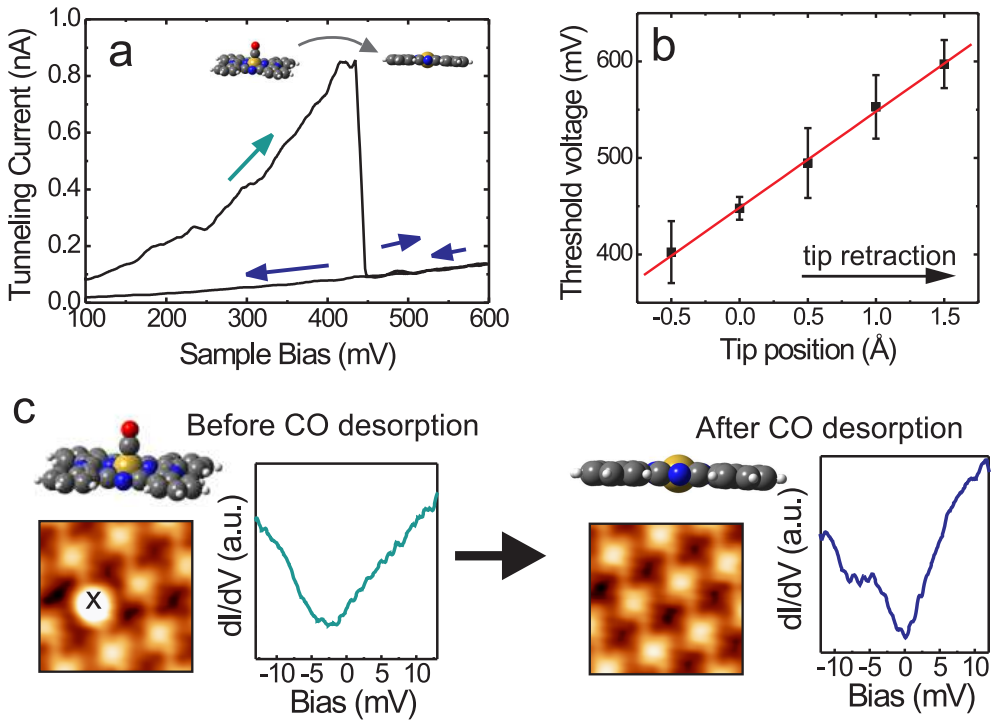

Fig. 5.7: Desorption of CO molecules from MnPc islands. (a) I-V characteristics recorded during desorption of CO. A sudden drop in current in observed marks the threshold voltage for CO detachment. (b) Threshold voltage plot versus tip-sample distance. *Zero* position of the tip corresponds to the feedback parameters V_f=100 mV and I_f=100 pA. Each point is an average of over 30 measurements. Linear fit of the data indicates that the process is driven by electric field of 1 V/nm. (c) STM image and dI/dV spectrum of the molecule before and after controlled CO desorption.

The origin of the zero-bias anomaly on the CO-MnPc molecules cannot be deduced directly from the experiments. As a first approach, one could associate it to a fingerprint of a Kondo ground state with a larger Kondo temperature ($T_K^{CO-MnPc}$ about $50 \pm 10\,\mathrm{K}$ can be fitted). However, an increase of Kondo temperature upon coordination to CO is unexpected.

5.3 Electronic structure of CO-MnPc.

A carbon monoxide (CO) molecule can react with a MnPc through the central manganese atom. To study the electronic and magnetic properties of this new molecule, we computed a DFT calculation using the ANT.G code [59]. As we did in the case of the MnPc, we have used a standard exchange-correlation functional in the generalized gradient approximation[33, 35] and a LANL2DZ double basis set.

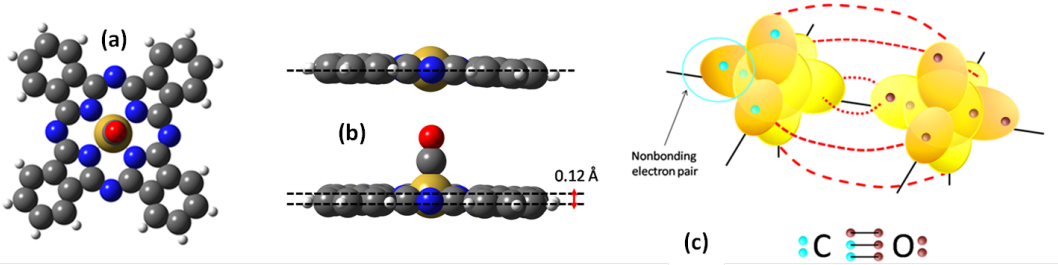

Fig. 5.8: (a) Picture of the COMnPc, frontal view. (b) horizontal view of the MnPc and COMnPc molecule, before optimization. (c) Picture of the atomic orbitals in the CO molecule.

As shown in figure 5.8 (a-b), the CO is anchored parallel to the z-axis direction, perpendicular to the plane of the molecule. When the CO molecule is attached onto the MnPc, the molecule undergoes a small conformational change (see figure 5.8 (b)). Thanks to the non-bonding electron pair in the CO molecule showed in figure 5.8 (c), the coupling is preformed via a complex coordination bond called π^*-back-bonding. This chemical bond drastically changes the magnetic moment of the MnPc from $S = 3/2$ before the bonding to $S = 1/2$ after a CO bonded. Following the section 5.1 we show in table 5.1 the charge and spin states of Mn d-orbitals in the case of the COMnPc molecule.

	N	N_{up}	N_{down}	$Spin$
d_{z^2}	6	6.38	2.89	11.39
d_{xz}	26	24.03	22.52	26.87
d_{yz}	26	23.20	22.76	35.10
$d_{x^2-y^2}$	17	12.96	15.26	24.66
d_{xy}	27	26.61	23.95	29.26

Table 5.1: Partial electronic charge and spin state in the d-orbital of the Manganese atom for the COMnPc molecule. N is the total number of electrons in the d-shell. $N_{up}(N_{down})$ is the number of electrons oriented in one or another of both spin directions. The d-orbital spin state (spin) is computed by the difference between the number of electrons in both spin directions.

The π^*-back-bonding bond is formed by three different interactions between the p-orbitals of the carbon monoxide and the d-orbitals of the Mn atom of the Phthalocyanine. We have pictured these interactions in figure 5.9.

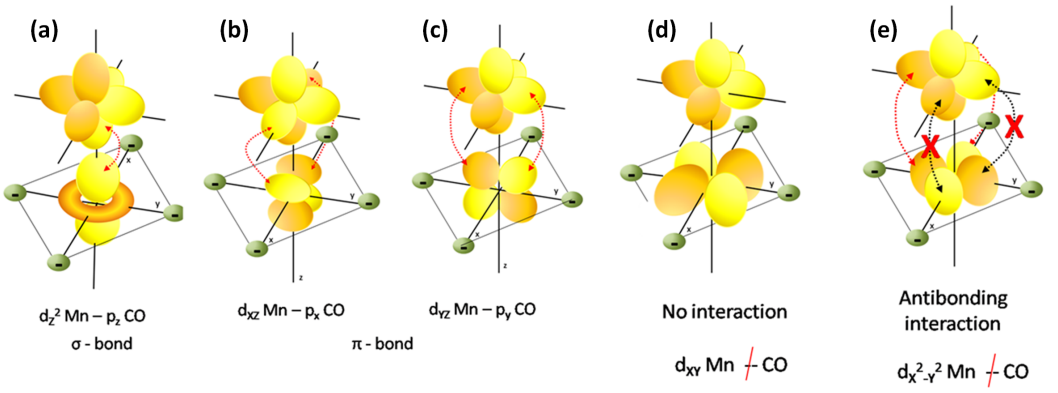

Fig. 5.9: Interaction between the p-orbitals of the CO molecule and the d-orbitals of the MnPc. From (a) to (e) : d_{z^2}, d_{xz}, d_{yz}, $d_{x^2-y^2}$, d_{xy}.

As we can see in this figure, the first interaction is performed between the non-bonding electrons pair of the carbon monoxide and the manganese d_{z^2}-orbital. A sigma bond arises from overlap of these orbitals. The other two interactions are performed between the p_z and p_y orbitals from the CO to the d_{xz} and d_{yz} orbitals of the Mn respectively. In this case a π-bond arises from the overlap of these orbitals.
The π^*-back-bonding involves a synergic process consisting of the donation of the non-bonding electron pair from the filled p-orbital of the Carbon monoxide to another anti-bonding orbital, empty in this case, of the Mn atom. The result of this bond is the quenching of the magnetic moment before located on the d_{z^2} and the $d_{xz/yz}$ orbitals of the MnPc. The last two pictures in figure 5.9 (d,e) show the no interacting cases of the $d_{x^2-y^2}$ and d_{xy} orbitals with the CO molecule, which allows them to allocated the one half spin state of the COMnPc molecule.

5.4 Electronic structure of MnPc and COMnPc on Bismuth.

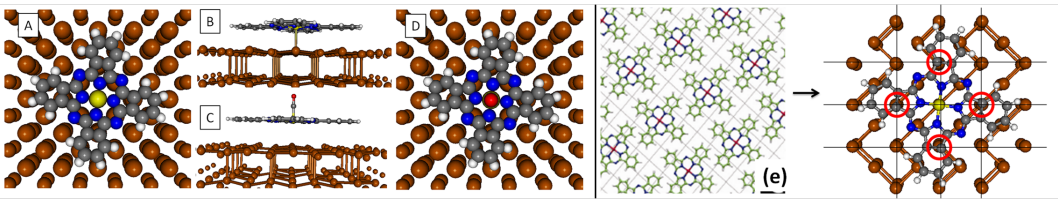

Fig. 5.10: (a) Schematic diagram of the MnPc and CO-MnPc absorbed on Bismuth(110).

To rationalize the experimental results we performed density functional theory (DFT) calculations of free and adsorbed MnPc and CO-MnPc molecules. All calculations were performed using the Green's function formalism implemented in the ANT.G code, based on the Gaussian03/09 commercial code [53, 59]. We used a general gradient approximation (GGA) with the Becke and Perdew-Becke Ernzerhof exchange-correlation functional [33, 35] in combination with

a common double local basis set LANL2DZ Different views of the computed system are shown in Fig. 5.10. The Bi(110) surface was described using two bilayers embedded on a tight-binding Bethe lattice.
Following the experimental results (Fig. 5.5), MnPc and CO-MnPc molecules were placed with the manganese atom directly on top of a Bi atom with an optimized distance to the surface. The molecule is rotated seven degrees with respect to the high symmetry axis of the Bi(110) surface, so that four carbon atoms of the phthalocyanine cycle and the central Mn ion are in direct contact with Bi(110) dangling bonds.
A free MnPc has a spin state $S = 3/2$ due to three unpaired electrons localized

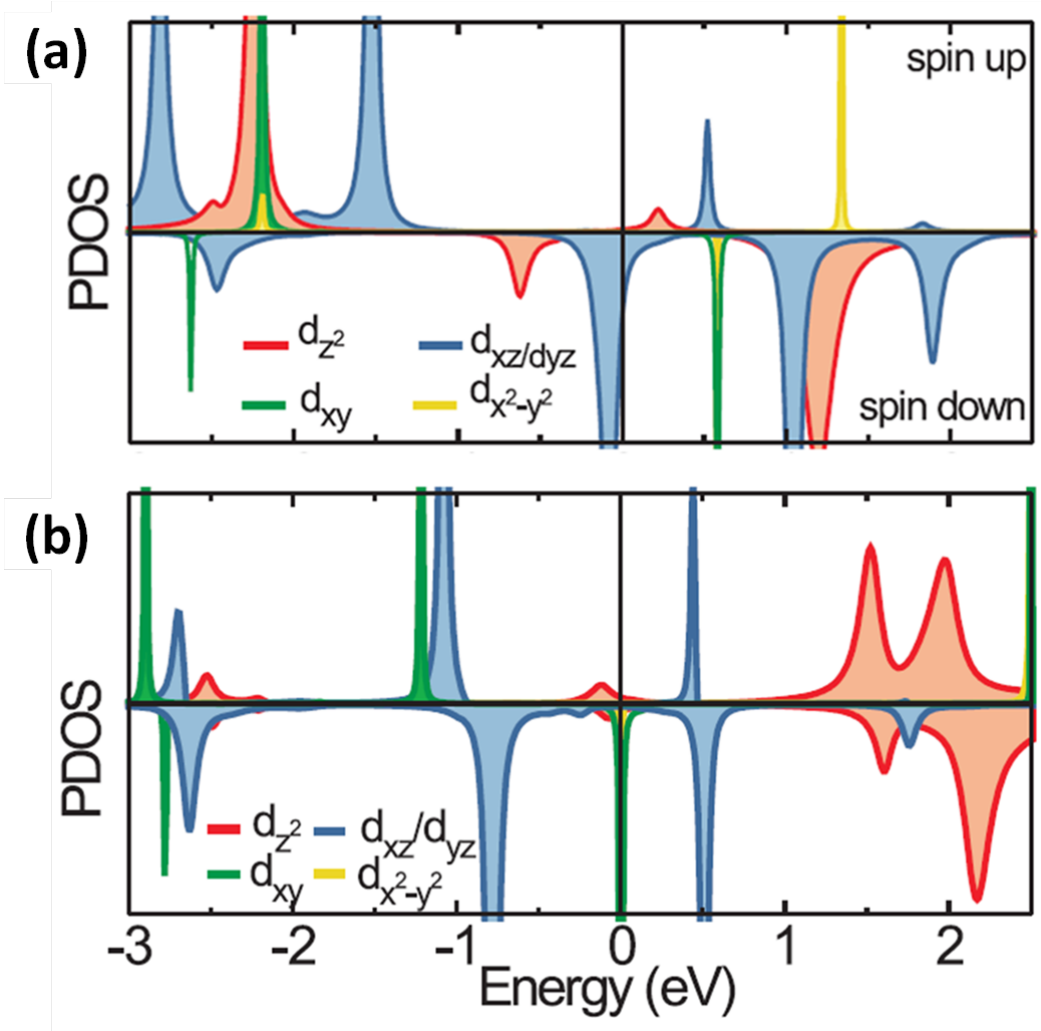

Fig. 5.11: (a) Local density of states. MnPc/Bi(110) (b) Local density of states. CO-MnPc/Bi(110)

on the manganese orbitals d_{xz}/d_{yz}, d_{z^2} and d_{xy}. The d_{xz}/d_{yz} orbitals, hosting three electrons, are strongly hybridized with the phthalocyanine ring of the molecule, masking the atomic character of its localized spin. The d_{xy} orbital is the deepest in energy and hosts the most localized unpaired electron. On the Bi(110) surface, MnPc keeps two unpaired electrons in the d-orbitals, as we find after an analysis of the molecular orbitals of the coupled molecule. The net spin density in the d_{xz} and d_{yz} orbitals is reduced and results now from four occupied molecular orbitals with different atomic contribution depending

on the spin orientation (Fig.5.11). In addition, a spin polarization arises in the ligands, opposite to that in the Mn core. Thus, the total spin is reduced to $S = 1$, with two identifiable and localized unpaired electrons in the d_{z^2} and d_{xy} orbitals (Fig.5.11).
Next, we perform a similar analysis for the CO-MnPC molecular complex. The CO molecule stays perpendicular to the MnPc molecular plane (Fig. 5.11). It is anchored to the manganese ion via its carbon atom through a synergic π^*-back-bonding. As a result, the population of the Mn d-orbitals strongly changes. The d_{z^2} and the d_{xz}/d_{yz} orbitals loose their magnetic moment: the former is emptied due to the overlap with a nonbonding orbital of CO and the latter is fully occupied due to the bond with the p_x and the p_y orbitals of CO. The total spin of the MnPc-CO complex is therefore reduced to $S = 1/2$, steaming from the unpaired electron remaining localized in the d_{xy} orbital. On the Bi(110) surface, this spin state is maintained in a molecular orbital with strong atomic d_{xy}-orbital character but a finite contribution from the phthalocyanine cycle (see Fig. 5.12(c)). In addition the CO coordination reduces significantly the spin density induced in the phthalocyanine ring.

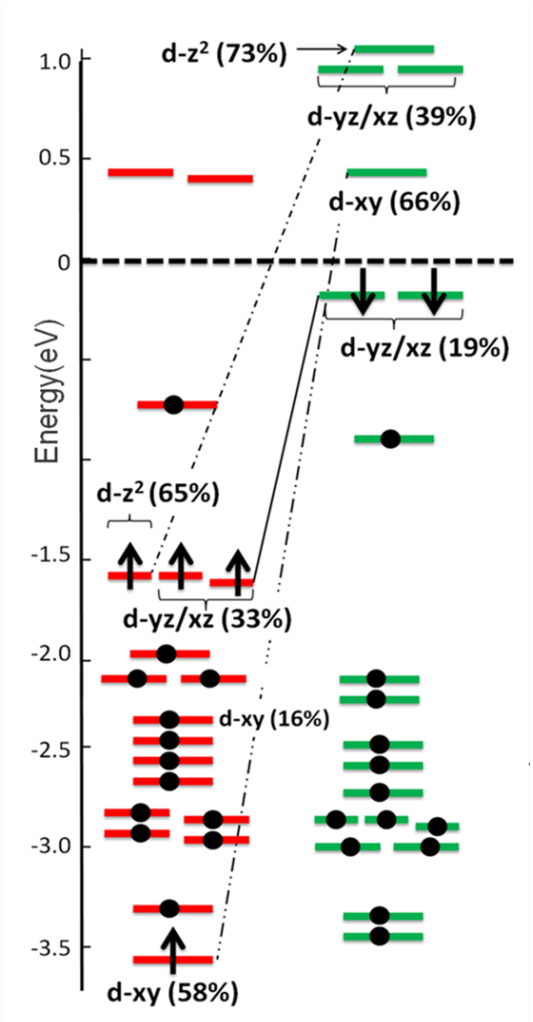

Fig. 5.12: (a) Schematic diagram of the MnPc d-orbitals energy levels deposited on Bi(110).

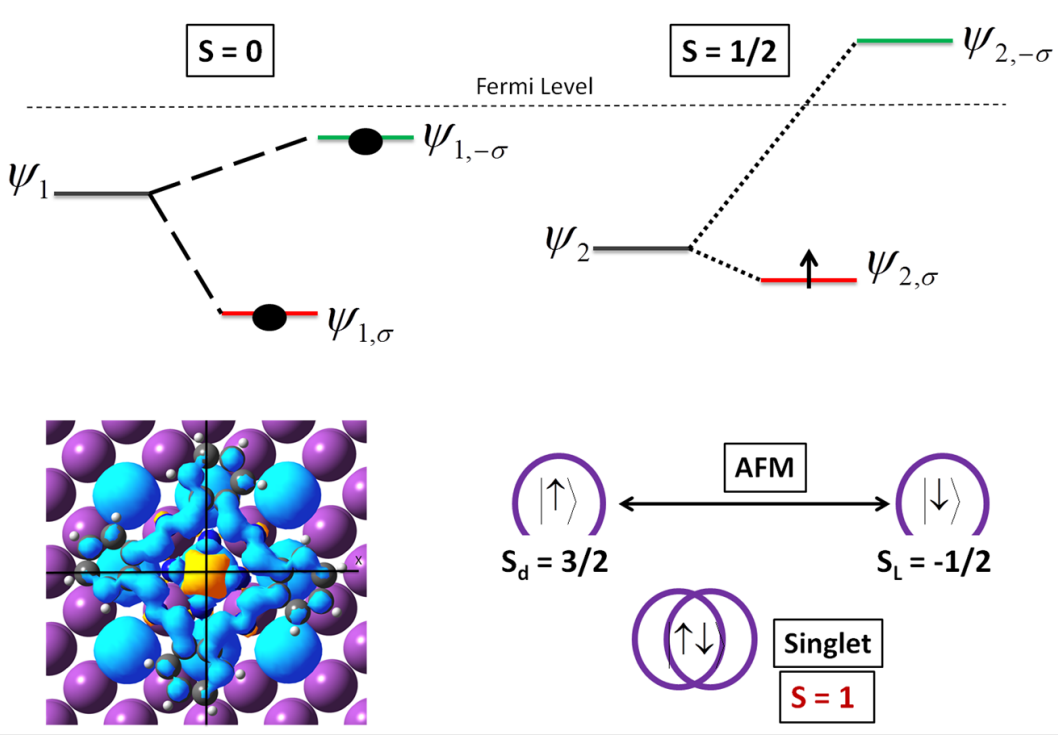

Fig. 5.13: Schematic representation of the molecular orbitals and the spin state in the case of MnPc/Bi(110).

5.5 Kondo effect in MnPc and CO-MnPc.

However, an increase of Kondo temperature upon coordination to CO is unexpected.

The strength of a Kondo screening channel depends, to a first approximation, on its hybridization with the substrate. For MnPc on Bi(110), the spin-polarized local density of states **(LDOS)** projected on the Mn-d orbitals shows that each orbital hosting an unpair electron interacts differently with surface (Fig.5.15 (a)). The Mn-d_{z^2} orbital hybridizes with a dangling bond of Bi, which leads to its substantial broadening. The d_{xy} orbital, due to the absence of z-component, remains highly decoupled and accordingly appears as narrow peaks in the PDOS spectrum. In such system each unpaired spin is screened via a separate Kondo screening channel, characterized by a different energy scale and thus different Kondo temperature [25]. Such scheme may lead to an underscreened spin, if the experimental temperature is larger than one of the Kondo temperatures.

In the DFT framework, the orbital-substrate coupling is represented by a hybridization function Δ which allows for a qualitative analysis of the feasible Kondo channels [60, 76].

Specifically, the prerequisite for the Kondo effect of the host orbital having a finite coupling to the electron bath, is equivalent to having non-zero value of the hybridization function Δ at the Fermi level [27, 121]. The value of Δ calculated for different Mn d-orbitals of adsorbed MnPc is shown in Fig. 5.15. The d_{z^2} orbital shows a peak in the hybridization function at the Fermi level indicating that this orbital is strongly screened by the substrate. On the contrary, the hybridization function of the d_{xy}-orbital has a zero value in a

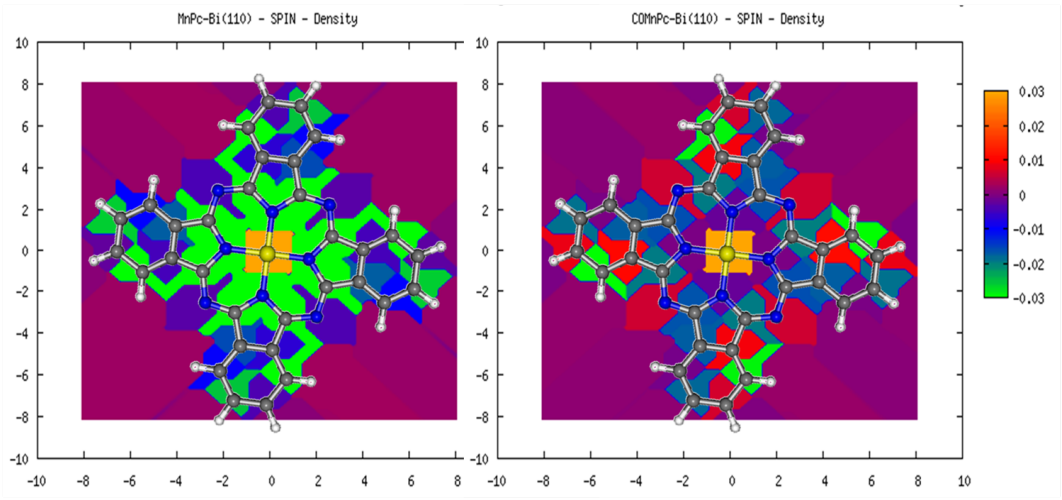

Fig. 5.14: Spin density distribution to the MnPc/Bi(110) and the CO-MnPc/Bi(110).

broad energy window in the vicinity of the Fermi level. These results suggest that the Fano resonance in the spectra of the MnPc molecule is a fingerprint of a Kondo channel opened to screen the d_{z^2} orbital. The unpaired spin of the d_{xy}-orbital is decoupled from the electron bath and this Kondo channel is closed. On the basis of these simulations, we conclude that the spin of the MnPc is underscreened.

It thus appears clear that the modification of the experimentally observed Kondo resonance upon CO coordination is a direct consequence of the redistribution of the d-electrons of the Mn atom. The spin-resolved LDOS of the adsorbed CO-MnPc projected on the Mn d-orbitals (Fig.5.15) confirms that the spin-polarization of the d_{z^2} and d_{xz}/d_{yz} orbitals is reduced. Only the d_{xy}-orbital appears to be relevant for the magnetism of the complex. However, this level is very localized and, as seen in Fig. 5.15, its corresponding hybridization function is zero in the vicinity of the Fermi level. This means that we expect no Kondo effect mediated by this orbital.

This apparent inconsistency with the experimental observations can be bypassed by noting that the PDOS on the d_{xy}-orbital shows a highly localized branch pinned at the Fermi level. This state thus belongs to the lowest unoccupied orbital of the molecule (LUMO), and is the only responsible for the chemical potential line-up between the molecule and the substrate.In these circumstances, charge fluctuations are expected to occur at the d_{xy}-orbital. When electronic correlations are considered, a mixed-valence regime is likely to emerge, as it is known for the f-electron compounds [121]. In this situation, one expects a resonance to appear at the Fermi level, similar as in the Kondo regime but characterized by a larger width.

Finally, we comment on the possible role of the surface states in the screening process on Bi(110). As a semimetal, bismuth is characterized by a low density of bulk states at the Fermi level; its surfaces are however strongly metallic due to the presence of the surface states. Therefore, the Kondo effect on bismuth can be expected to involve surface states rather than bulk states. However, strong spin-orbit coupling induces the spin polarization of the surface states through the Rahsba effect [116]; the concept of screening in such system is

not straightforward. The Kondo effect involving the chiral spin-states has been recently intensively discussed in the context of topological insulators and can be understood assuming a complex structure of the Kondo cloud with a nontrivial spatial and spin dependence.

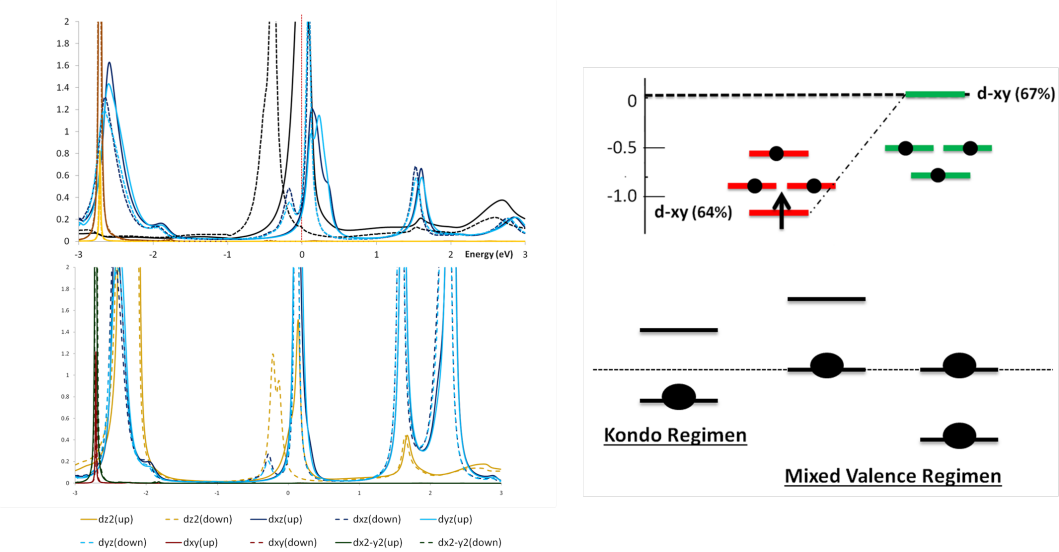

Fig. 5.15: (a) Hybridization function of MnPc/Bi(110) (b) Hybridization function of CO-MnPc/Bi(110) (c) Molecular orbitals of COMnPc.

In summary, we have shown through experiments and theory that the coordination of a CO molecule to a manganese phthalocyanine on Bi(110) changes its magnetic ground state. The attachment of CO molecule to the Mn ion, causes a charge redistribution in the d-orbitals and a reduction of the spin of the complex from $S = 1$ to $S = 1/2$. Our calculations suggest that CO coordination drives the complex from the Kondo screening regime into mixed-valence regime, where the charge fluctuation are likely to occur. The change of the magnetic ground state is reversible and can be controlled by selective desorption of individual CO molecules. Such chemical control over the molecular spin opens the possibility of tuning $in - situ$ of the magnetic properties of molecular systems.

Chapter 6

The Kondo effect in Manganese Phthalocyanine on Pb(111).

6.1 Initial Motivation.

As we announced in the previous chapter, herein we will focus on the MnPc/Pb(111) system measured by Fu et.al. [99] and Franke et.al [25] (shown in figure 6.1).

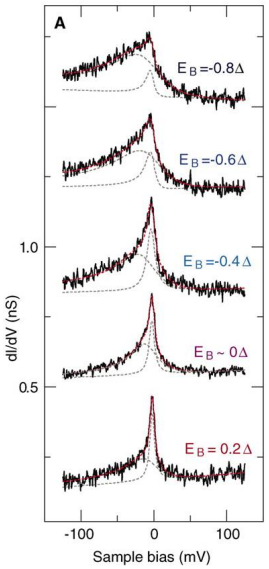

Fig. 6.1: Experimental observation of Kondo resonance in MnPc on lead surface. The image is taken from [25].

Whenever a magnetic atom or magnetic molecule is coupled to metallic electrodes the conduction electrons are likely to screen its magnetic moment through the Kondo effect [94, 121] which is signaled by Fano-Kondo lineshapes in the conductance spectra [122–126]. Atomic precision experimental control offers the possibility to study a wide range of electron correlation phenomena related to the Kondo effect. For example, the atomic-scale control of atoms or molecules adsorbed on metal surfaces or anchored to nanoscopic electrodes allows for a direct manipulation of the orbital hybridization and for a controlled tuning from the so-called underscreened to the overscreened Kondo effects, both regimes showing interesting non-Fermi liquid behavior [127].

Recently, underscreened Kondo effects have been reported for a C_{60} quantum dot molecule coupled to metal leads [128] and for a $Co(tpy\text{-}SH)_2$ complex coupled to Au nanocontacts [129]. The overscreened Kondo effect, on the other hand, has been very recently predicted to occur in Au nanocontacts hosting a single Co atom [130].

Although this work has a great experimental motivation in the works mentioned above, as well as other experiment of phthalocyanines derived molecules [98–101], the real motivation of this work is theoretical. Our goal was and is to contribute to understanding, from an atomistic point of view, of the Kondo effect in molecular complex systems where we can find high spin states. The

latter makes the determination of the nature of the Kondo-like resonances observed experimentally, thereof, their shape and evolution with temperature, bias, gate and other parameters, is not trivial, nor is unclear at present.
Furthermore, since the MnPc is a coordination complex containing a transition metal (TM) center where the strong coupling to the organic ligand quenches the spin into a relative lower value of $S = 3/2$ [102], both one-body quenching and many-body screening processes can coexist, when the molecule is deposited on a metal surface. The separation of these two contributions from the experimental signals is very difficult [131]. These two phenomena are very difficult to disentangle their respective contributions to the experimental signatures.
Here, by treating both screening and quenching on the same footing we elucidate the relevant mechanisms behind the experimental observations in a single MnPc absorbed on the Pb(111) surface in the normal (i.e., not superconducting) phase [25, 99]. This and similar systems have been studied both experimentally and theoretically by different authors [25, 26, 99, 119, 132]. In contrast to previous theoretical work [26, 132–134] our approach fully takes into account the electronic correlations and hybridization of the entire Mn $3d$-shell from two different approaches, the atomic and the molecular. This allows us to get the first complete picture of the Kondo effect and molecular quenching processes in a high-spin complex.

6.2 MnPc on Pb(111). Electronic Structure.

We considered a single MnPc adsorbed at the top site of a Pb(111) surface as shown in Figure 6.2 (a). We first relaxed the atomic structure, orientation, and distance of the molecule to the substrate which was represented by a cluster consisting of five atomic layers. This is done through the common Kohn-Sham (KS) approach to DFT using a standard GGA functional [35]) as implemented in the Gaussian09 package [53]. Next we embed the cluster consisting of the substrate and molecule (hereon called region C) into an effective semi-infinite bulk electrode model as implemented in the code ANT.G [59, 60] which interfaces Gaussian09. The KS Green's function (GF) of the system C can now be obtained as

$$G^0_{\rm C}(\omega) = (\omega + \mu - H^0_{\rm C} - \Sigma_{\rm S}(\omega))^{-1} \tag{6.1}$$

where $H^0_{\rm C}$ is the self-consistent KS Hamiltonian re-evaluated considering now $\Sigma_{\rm S}(\omega)$, which is the embedding self-energy describing the semi-infinite bulk electrode.
The spin polarized KS spectrum of all molecular orbitals close to the Fermi energy is shown in Fig. 6.2 (b) along with their Mn $3d$ orbital character. The ones depicted in gray do not have any Mn atomic character at all, being completely localized on the organic ligand. A strong localization in the $d_{x^2-y^2}$, d_{xy} and d_{z^2} atomic orbitals is apparent, being signaled by a single molecular orbital (per spin with strong atomic character. The $d_{x^2-y^2}$ appears as an empty molecular orbital, well above the Fermi level, the charge density in this orbital (see Table I being only due to the contribution of many molecular orbitals with negligible participation of the atomic orbital. The other two

have a localized unpaired electron each. The third unpaired electron is shared between the $d_{xz/yz}$ orbitals. The localized character of this spin is masked due to the strong hybridization of these orbitals with the ligand, there being four molecular orbitals (per spin) with significant $d_{xz/yz}$ atomic character.

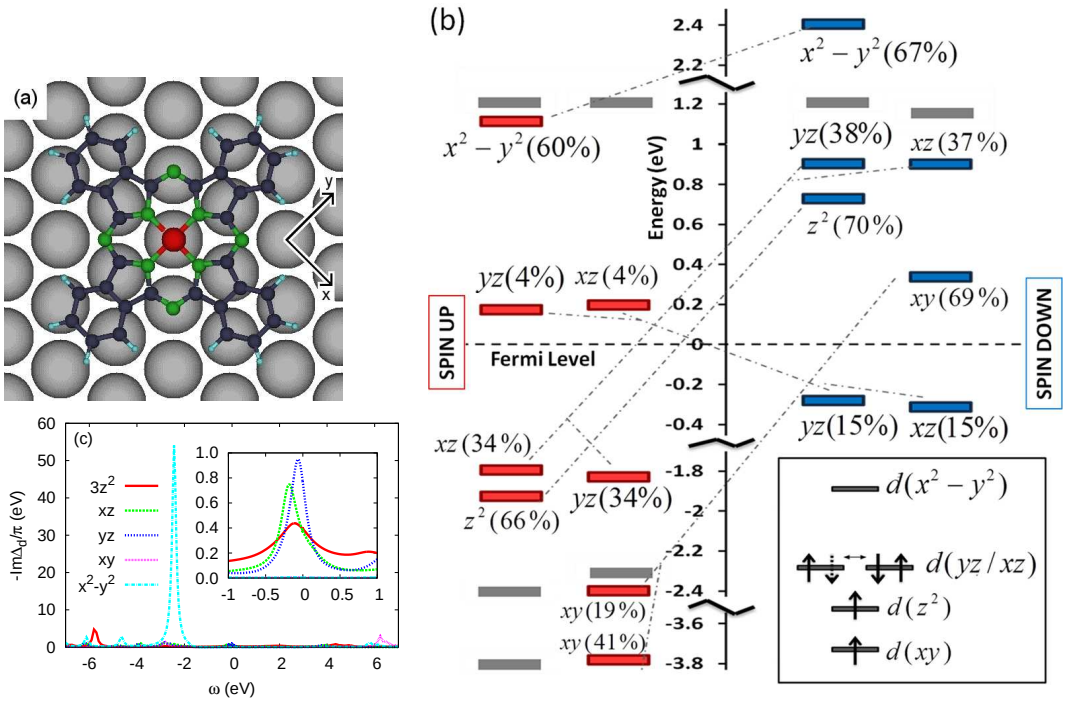

Fig. 6.2: (a) Top view of a PcMn adsorbed on a Pb(111) surface in its more stable configuration. (b) Molecular orbital energy diagram as obtained from the projected spin-polarized KS Hamiltonian of the adsorbed molecule. The Mn 3*d* orbital character (percentage) of each molecular orbital is shown. The inset shows the schematics of the Mn 3*d* orbital energies and associated spins as considered in the OCA calculations. (c) Orbital resolved imaginary part of the hybridization function for the Mn 3*d* orbitals as obtained from the GGA non-magnetic electronic structure calculation.

In Fig. 6.2 (c) we show the imaginary part of the hybridization function $\Delta(\omega)$ which describes the broadening of the Mn 3*d*-levels due to the coupling to the substrate and to the organic part of the molecule. We see that within an energy window of ± 1.0 eV around the Fermi level, only three out of the five 3*d*-levels are actually broadened ($d_{3z^2,xz,yz}$). The d_{xy} and $d_{x^2-y^2}$ orbitals, which are parallel to the surface, show no hybridization at all in this energy window. Outside this window, however, while the d_{xy} orbital still does not show any significant coupling, the $d_{x^2-y^2}$ orbital presents a very large peak at -2.4 eV (and many small peaks) which indicates a strong coupling to the organic ligand. This is actually a manifestation of what crystal-field theory anticipates and the DFT calculation shows, as described in the previous paragraph.

Since the $d_{x^2-y^2}$ orbital is virtually empty and shifted to high energies, we exclude this orbital from the AIM model from now on. The $3d_{z^2}$, d_{xz}, and d_{yz} orbitals, being the only ones showing hybridization around the Fermi level, are also the only ones susceptible to Kondo screening. All three orbitals feature a strong peak in the hybridization function around the Fermi energy which stem from coupling to molecular orbitals in the organic ligand which, in turn, couple to the substrate. Note that due to symmetry reasons the direct coupling of

the d_{xz} and d_{yz} orbitals in the top position is strongly suppressed. In contrast, the $3d_{z^2}$ orbital also couples to the substrate directly, resulting in a flatter hybridization function.

6.3 MnPc on Pb(111). The atomic Model to the Kondo Problem.

In order to capture many-body effects beyond the DFT level, we have applied the DFT+impurity solver method for nanoscopic conductors developed by one of us in earlier work [76, 135]. To this end the mean-field KS Hamiltonian is augmented by a Hubbard-like interaction term $\hat{\mathcal{H}}_U = \sum_{\alpha\beta\gamma\delta\sigma\sigma'} U_{\alpha\beta\gamma\delta}\, d^\dagger_{\alpha\sigma} d^\dagger_{\beta\sigma'} d_{\delta\sigma'} d_{\gamma\sigma}$ which accounts for the strongly interacting electrons of the Mn $3d$-shell. These are different from the bare interactions due to screening processes. The screened Coulomb interaction within the Mn $3d$-shell, $U_{\alpha\beta\gamma\delta}$, has been determined using the constrained RPA approach [136]. We find that the matrix elements $U_{\alpha\beta\gamma\delta}$ are somewhat anisotropic with variations of up to 10% between different orbitals. For the *intra*-orbital Coulomb repulsion $U_{\alpha\alpha\alpha\alpha}$ we have a mean value of 5.4 eV and for the *inter*-orbital Coulomb repulsion $U_{\alpha\beta\alpha\beta}\,(\alpha \neq \beta)$ a mean value of 4.1 eV. The orbital anisotropy of the direct repulsion will be fully taken into account in our calculations. The exchange matrix elements $U_{\alpha\beta\beta\alpha}$, which give rise to the Hund's rule coupling J_H, also become somewhat orbital-dependent. But here we simply set J_H to the orbital-averaged exchange interaction $J_H \equiv \langle U_{\alpha\beta\beta\alpha}\rangle$ for which we find 0.65 eV.

The interacting Mn $3d$ shell coupled to the rest of the system (organic scaffold + surface) thus constitutes a so-called Anderson impurity model (AIM). The AIM is completely defined by the interaction matrix elements $U_{\alpha\beta\gamma\delta}$, the energy levels ϵ_d of the $3d$-orbitals and the so-called hybridization function $\Delta_d(\omega)$. The latter describes the (dynamic) coupling of the Mn $3d$-shell to the rest of the system and can be obtained from the KS GF [135] as $\Delta_d(\omega) = \omega + \mu - \epsilon^0_d - [G^0_d(\omega)]^{-1}$ where μ is the chemical potential, ϵ^0_d are the KS energy levels of the $3d$-orbitals and $G^0_d(\omega)$ is the KS GF projected onto the $3d$-subspace. The energy levels ϵ_d are obtained from the KS levels, $\epsilon_d = \epsilon^0_d - E_{dc}$ where, as usual in DFT++ approaches [137], a double counting correction (DCC) has to be subtracted to compensate for the overcounting of interaction terms. Here we employ the so-called fully localized or atomic limit DCC [138], but generalized to the case of an anisotropic Coulomb repulsion: $E^\alpha_{dc} = \sum_\beta U_{\alpha\beta\alpha\beta} \cdot \left(n_\beta - \frac{1}{2M}\right) - J_H\,(N_{3d} - 1)\,/2$, where n_α is the DFT occupation of orbital α, N_{3d} the total occupation of the Mn $3d$-shell, and M, the number of correlated orbitals.

The AIM problem is now solved using the one-crossing approximation (OCA) [139]. This yields the electronic self-energy $\Sigma_d(\omega)$ which accounts for the electronic correlations of the $3d$-electrons due to strong electron-electron interactions. The *correlated* $3d$ GF is then given by $G_d = ([G^0_d]^{-1} - \Sigma_d + E_{dc})^{-1}$. Correspondingly, the *correlated* GF for C is given by $G_{\mathrm{C}} = ([G^0_{\mathrm{C}}]^{-1} - \Sigma_d + E_{dc})^{-1}$ where Σ_d and E_{dc} only act within the $3d$ subspace. From G_{C} we can calculate the transmission function $T(\omega) = \mathrm{Tr}[\Gamma_{\mathrm{T}}\, G^\dagger_{\mathrm{C}}\, \Gamma_{\mathrm{S}}\, G_{\mathrm{C}}]$ where $\Gamma_\alpha \equiv i(\Sigma_\alpha - \Sigma^\dagger_\alpha)$

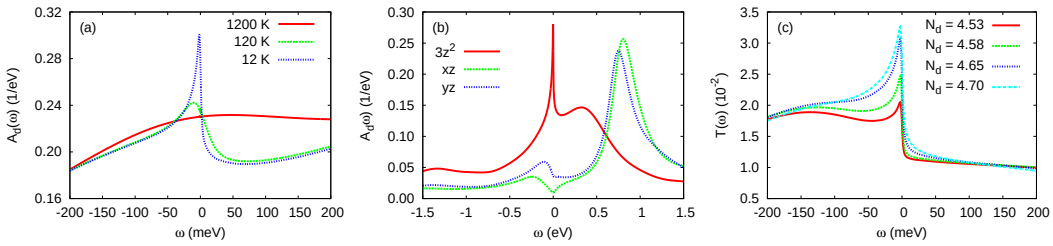

Fig. 6.3: (a) Total spectral function of the Mn 3*d*-shell near the Fermi level for different temperatures. (b) Orbital resolved spectral function of the Mn 3*d*-shell at low temperature ($T \sim 12$ K) in a larger energy window than in (a). (c) Transmission function for different filling N_d of the four Mn 3*d*-orbitals taken into account in the OCA calculation at low temperature ($T \sim 12$ K).

	$3z^2$	xz	yz	xy	x^2-y^2	tot.
GGA	1.19	1.18	1.19	1.04	0.67	5.27
GGA+OCA	1.32	1.13	1.16	1.04	(0.67)	5.32

Table 6.1: Orbital occupations of Mn 3*d*-shell as calculated with DFT on the level of GGA and with OCA. Note that the x^2-y^2-orbital was not taken into account in the OCA calculation (see text).

for $\alpha = T, S$ describes the coupling of C to the STM tip (T) and to the semi-infinite Pb surface (S). Since the (small) voltage mainly drops between tip and molecule, the transmission directly yields the differential conductance: $\mathcal{G}(V) = (2e^2/h)T(eV)$.

Let us now turn to the results of the OCA calculation for solving the generalized AIM problem. We find that, except for the xy orbital, the orbitals of the Mn 3*d*-shell are in a mixed-valence state. There are strong fluctuations between a five-fold degenerate atomic configuration with $N_d = 4$ electrons and maximal spin $S_d = 2$ where all orbitals are singly occupied and three four-fold degenerate atomic configurations with $N_d = 5$ electrons and $S = 3/2$ where one of the $3z^2$, xz and yz orbitals is doubly occupied. This results in an average occupation of the four Mn 3*d*-levels of $N_d \approx 4.6$ electrons and an average total spin $\langle S_d \rangle \approx 1.6$ close to 3/2. The extra half-electron stems from the emptied $x^2 - y^2$ orbital and is shared among the $3z^2$, xz, or yz orbitals. This leads to strong charge fluctuations in these orbitals (see Tab. I) and thus quenching of their spin from 3/2 to ~ 1. The xy orbital on the other hand is essentially singly occupied, thus carrying a spin 1/2. Note that the individual orbital channels are not in a mixed-valence situation as the individual occupations are clearly below 1.5 and therefore the Kondo effect in individual orbitals is possible despite the Mn 3*d*-shell as a whole being in a mixed-valence state [127]. Although $\langle S_d \rangle$ is finite, the expectation value for any of its projections is zero, since all states with $S_d^z = -S_d \ldots + S_d$ contribute equally. Also note that $\langle S_d \rangle \sim 3/2$ *is not* the expectation value of the total spin of the system but only of the Mn 3*d*-shell. The spin of the whole system is lower due to screening by the Kondo effect with the conduction electrons of the substrate and the organic rest of the molecule as we will see below.

Fig. 2a shows the spectral function of the Mn 3*d*-shell for different temperatures. We see a sharp Kondo-peak developing right at the Fermi level when the temperature is lowered. As can be seen from Fig. 2b where we show

the orbital-resolved spectral function on a larger energy scale than in Fig. 2a, the Kondo peak stems from the $3z^2$ orbital, the only orbital directly coupling to the substrate near the Fermi energy. Notice that in the existing literature this orbital is considered to be quenched [99] and is excluded from correlated models [140]. The Kondo temperature for this orbital is $T_K \sim 100$ K. The xz and yz orbitals, on the other hand, each feature small bumps just below the Fermi level with a much larger width (~ 0.5 eV) than the Kondo peak in the $3z^2$ orbital. We interpret these pronounced peaks in the hybridization function for the xz- and yz-orbitals as a result of these orbitals only coupling *via the organic ligands* to the substrate. In other words, these bumps suggests the formation of a many-body singlet state between the Mn $3d$-level and a molecular orbital in the organic rest of the molecule as in the zero-bandwidth Anderson impurity model (see e.g. App. of ref. [121]). In this model the formation of the total spin-singlet state between the strongly interacting impurity level and a *single* non-interacting bath level gives rise to two strongly renormalized resonances below and above the Fermi level. These resonances are precursors of the Kondo peak which develops as more and more bath levels are added to the model. Therefore we can think of the spin in the xz and yz orbitals as being screened due to the formation of a many-body singlet state by strong coupling with the organic ligand. The spin 1/2 in the xy orbital, on the other hand, remains unscreened due to lack of hybridization with the substrate or molecule near the Fermi level. This is in contrast to existing claims where this orbital is considered to be screened and responsible for high-energy Kondo features Ref. [99].

Therefore we are dealing here with a $S = 3/2$ *underscreened* Kondo effect where only the spin $S \approx 1$ within the $3z^2$, xz and yz orbitals is screened, leaving a residual spin 1/2 in the Mn xy orbital which may lead to so-called singular Fermi-liquid behavior [141]. Only the screening of the spin within the $3z^2$ orbital gives rise to a Kondo resonance while no significant low-bias experimental signatures are expected from the strongly coupled spin in the xz/yz orbitals. Since the Kondo temperature of the $3z^2$ channel is too high, it is not unrealistic to attribute the Shiba peaks in Ref. [25] to a low-energy scale Kondo screening of the xy orbital in a lower symmetry experimental situation [140].

The Kondo resonance appearing in the spectral function of the Mn $3d$-shell for low temperatures is somewhat asymmetric. This is mainly a result of two effects: On the one hand charge fluctuations in the $3z^2$ orbital make the Kondo peak asymmetric due to the proximity of the upper Hubbard peak. On the other hand the modulation of the hybridization function due to the coupling to the organic ligands near the Fermi level further enhances this asymmetry. The bumps in the spectral function of the xz and yz orbitals on the other hand do not have a significant contribution to the asymmetry of the Kondo peak due to their small spectral weight. This asymmetry of the Kondo peak in the spectral function is even more enhanced in the tunnelling spectra as can be seen in Fig. 2c where we show the tunnel transmission $T(\omega)$ calculated for a Pb tip positioned above the Mn atom in a distance of 5 Å. The reason for this further enhancement is the modulation of the Mn $3d$ spectral function by the DOS of the Pb tip and the Pb substrate. For a Au tip we actually find that

the tunnel spectra (not shown) are a little bit less asymmetric. Therefore the peak in the tunnel spectra just stems from the Kondo peak in the $3z^2$ orbital. In fact, a sharp Kondo peak in either of the xz or yz channel would rather give rise to a dip in the tunnelling, but not to a peak since the direct tunnel matrix elements between the tip and these two orbitals vanish for symmetry reasons.

Charge fluctuations usually have a strong effect on the Kondo screening. In Fig. 2(c) we show the effect of altering the occupation of the Mn 3d-shell on the tunneling spectra by shifting the Mn 3d-levels by a few decimal eV. We see that the shape of the Kondo resonance and in particular its width is strongly affected by the slight changes in the occupation of the Mn 3d-shell. In fact our calculated lineshapes reproduce very well the variation of lineshapes measured in recent experiments. Hence we conclude that the experimentally observed variation in lineshapes for different PcMn molecules on the Pb(111) surface [25, 99] is likely due to slight changes in the occupation of the Mn 3d-shell induced by slight variations in the structure or environment of the molecule in the experiments.

In summary, we have studied the correlated electronic structure of a MnPc adsorbed on the Pb(111) surface, fully taking into account the strong electronic correlations originating from the Mn 3d-shell. Our results show that the adsorption does not essentially modify the total spin $S = 3/2$ of the molecule, being distributed among four of the five 3d-orbitals. This finding is in stark contrast to previous works which assume/find a spin 1 [140] or even a spin-1/2 state due to strong quenching with the substrate and organic ligand [99]. We further find that the experimentally observed asymmetric Kondo resonance in this system [25, 99] is due to an underscreened Kondo effect where a spin 1/2 in the Mn 3d-shell remains unscreened. The Kondo resonance in the tunnel spectra actually stems from only one of the Kondo-screened orbitals. Its peculiar lineshape arises from the modulation of the hybridization function due to a strong coupling to the organic ligand, not being necessary to invoke the superposition of two Kondo peaks with different Kondo temperatures as done in Ref. [25].

Chapter 7

Kondo effect in pure carbon molecules.

We present a fully first-principles approach to the Kondo problem in purely carbon-based molecules or organic radicals in proximity to metal electrodes. In these molecules the screened spin may be an unpaired π electron delocalized over many atoms or even the entire molecule. Our starting point is a projection of the full Kohn-Sham Hamiltonian onto the molecule followed by a selection of the active space, e.g., a selection of the relevant molecular orbitals. A constrained density functional calculation allows us to avoid the double- counting correction problem. Once obtained the appropriate single-particle levels along with the hybridization function, the spectral density and transmission function is computed through a DMFT impurity solvent. We apply this technique to a C_{60} molecule contacted by Au electrodes. By gating the system we study the zero-bias features arising in the mixed-valence, the spin 1/2 Kondo, and the underscreened spin 1 Kondo regimes. This parameter-free theory is successfully tested against a variety of experimental results.

7.1 Experimental Motivation

Kondo-like zero-bias resonances in transport experiments arise when spins or unpaired electrons interact with the current-carrying metallic environment. This traditional many-body problem has been increasingly investigated in the past decade in a variety of systems, still being today a subject of great interest because of its physical wealth, both from a fundamental point of view and for their potential applications in the field of spintronics. The Kondo resonance was first observed in semiconductor quantum dots [143]. Later, a variety of systems such as carbon nanotubes [144], magnetic atoms and molecules deposited on surfaces [145, 146], and spin impurities in graphene, among others, have served as a playground for further studies of this many-body phenomenon.

Regardless of the nature and complexity of the system at hand, the basic theoretical model that is routinely used to gain insight into the Kondo effect is the Anderson model, where a few parameters are fitted as needed. The solutions to this model and variants of it are essentially well understood.

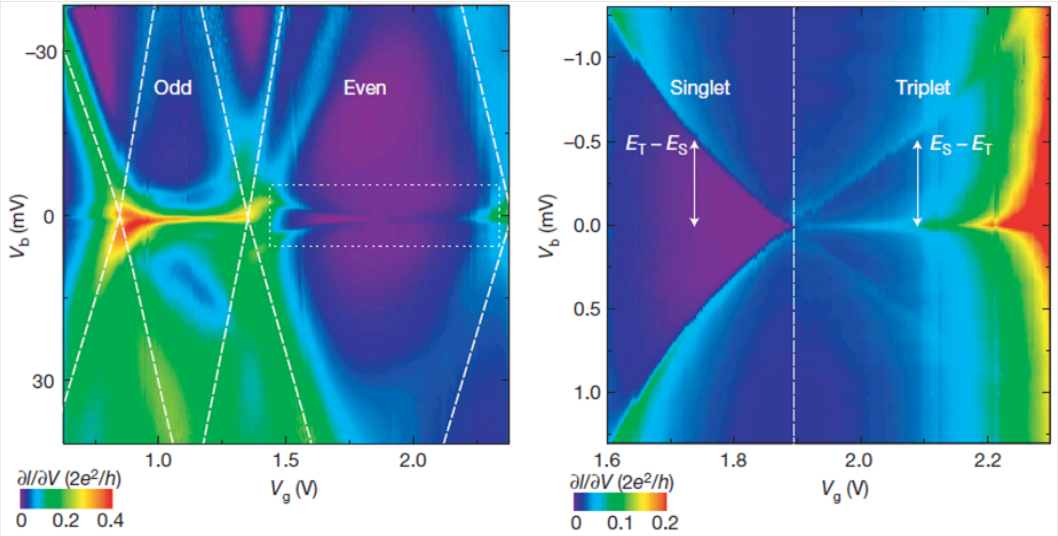

Fig. 7.1: Quantum phase transition. (left) Color map over two Coulomb diamonds of the differential conductance dI/dV (in units of $2e^2/h$, where h denotes Planck's constant) as a function of bias voltage V_b and gate voltage V_g at $T = 535$mK and $B = 50$. (right) Detail of the differential conductance in the dotted white rectangle in (left), showing the singlet to triplet spin transition. Image taken from [142].

However, while Anderson impurity models describe in essence the phenomenon, they may ignore important aspects of the nature of real systems, particularly when it comes to a quantitative description. In this direction, a great effort has been made to develop more sophisticated models and to find solutions to these, among which one finds a combination of density functional theory (DFT) with sophisticated many-body techniques such as numerical renormalization group (NRG), time continuous Quantum Monte Carlo methods, and dynamical mean field theory (DMFT) [135, 147, 148].
However, to the best of our knowledge, all these first-principles efforts have been directed towards systems where the Kondo effect originates in magnetic atoms with d- or f-type open shells and ultimately rely on atomic parameters. These approaches are relatively successful in cases such as coordination complexes, a primary example being transition metal phthalocyanines [27], but are unable to treat purely carbon-based systems such as C_{60}, carbon nanotubes, other graphene derivatives, and organic radicals where the Kondo effect is due to unpaired π electrons delocalized over many atoms or even the entire molecule. In the case of organic radicals, for instance, which have recently been stabilized and measured on metallic surfaces, the observed Kondo effect does not count with theoretical support.

7.2 The theoretical model

Here we present a novel theoretical approach to the Kondo problem based on the combination of DFT calculations and a DMFT impurity solver. Our general goal is to describe *with no parameters* the experimental observations of the Kondo effect on systems (mostly molecules) where the screened spin(s) is not localized on a single magnetic atom, but is itinerant, typically an unpaired π electron(s). We first rely on a DFT calculation to obtain the

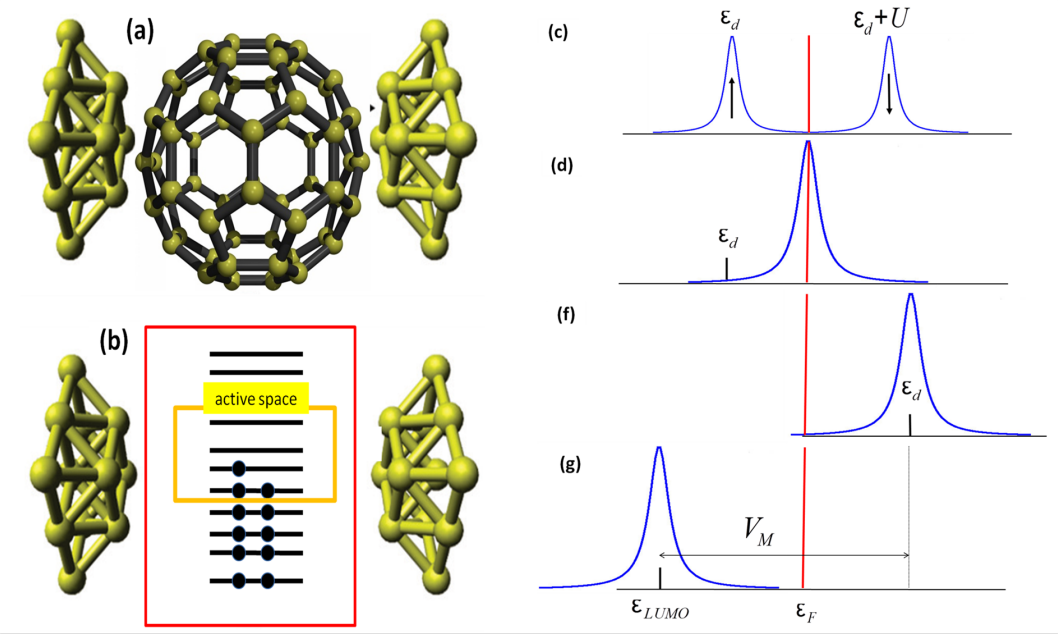

Fig. 7.2: (a) Schematic picture of the C60 molecule attached Gold electrodes. (b) Schematic representation of the active space. (c-g) Evolution to a model of one level to explain the difference between the calculations.

Kohn-Sham Hamiltonian of the molecule as well as the hybridization function of it. Since there is no privileged atom hosting the spin, we must work on the basis of eigenstates (molecular orbitals) of the Hamiltonian. Secondly, we select an active space composed of a set of molecular orbitals (MO's), typically the highest occupied (HOMO) and lowest unoccupied (LUMO), to properly introduce the correlations on them. Because the Kohn-Sham Hamiltonian already includes electronic interactions, we have to remove these prior to the addition of correlations. For this we propose a new idea based on a constrained DFT (CDFT) implementation that allows us to empty the active space. The thus emptied single-particle Kohn-Sham Hamiltonian along with the interactions between molecular orbitals are then introduced in the impurity solver. Different levels of theory such as the non-crossing approximation (NCA) or the one-crossing approximation (OCA) are used to obtain the spectral function. As an example we study a C_{60} molecule coupled to gold electrodes, in which Kondo resonances have been previously reported in different experiments [142, 143, 146] for various regimes.

The electronic structure of the C_{60} molecule attached to two Au leads is computed in the framework of DFT combined with the (non-equilibrium) Green's function formalism as implemented in our code ANT.G[59] which interfaces with GAUSSIAN [53]. In all calculations we have used a standard exchange-correlation functional in the generalized gradient approximation[33, 35]. We have employed a minimal $spd-$pseudopotentials basis set [86] and the leads have been modelled by a finite pyramidal shape[149] embedded in a (spd) tight-binding Bethe lattice model. This is shown in Fig. 7.3 (a).

When studying correlated states the first step is the selection of the physically relevant electronic levels which define the so-called active space. To begin with, we will project our Kohn-Sham Hamiltonian $\mathbf{H}^0$ onto the C_{60} molecule. As discussed in our previous work[150], the mathematical partition of this

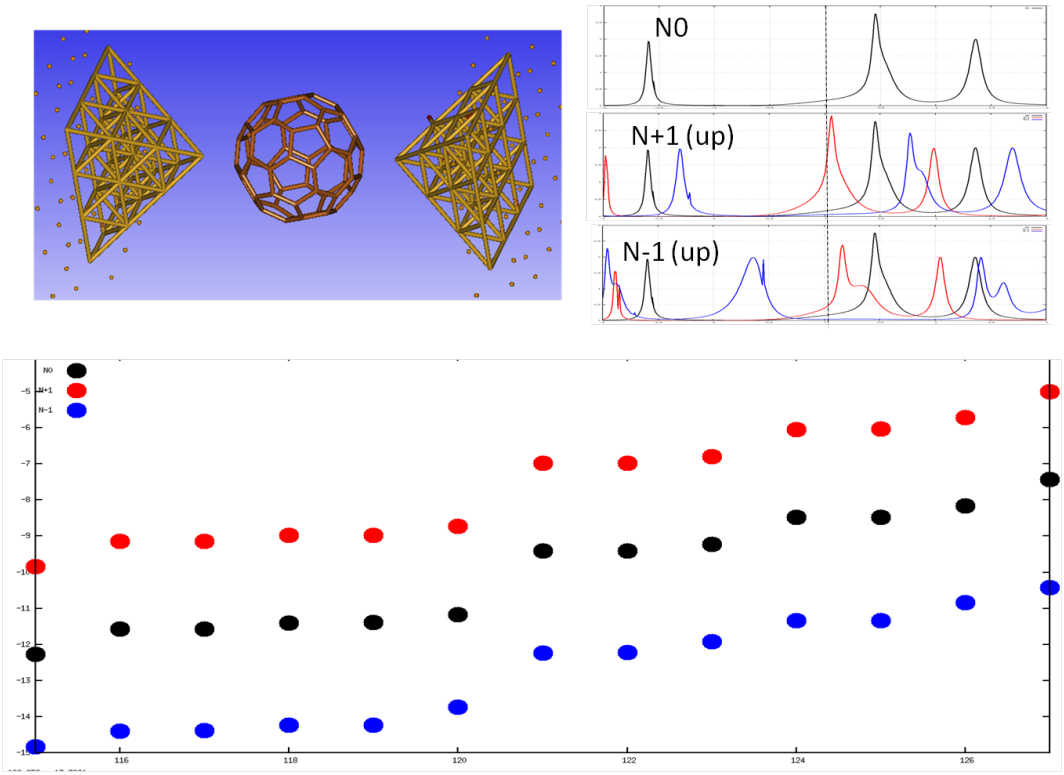

Fig. 7.3: (a) Schematic picture of the C60 molecule attached Gold electrodes. (b) Molecular spectrum (eigenvalues) and (c) transmission function of the system showed in (a) with three different charge states.

molecular bridge in different regions is not trivial due to the non-orthogonality of the basis set. Here we have chosen to transform the original metric of our basis to a block orthogonal metric[150], already introduced in Ref. Thygesen:prb:06. Thus the projector operator onto the molecular subspace is simply defined by the overlap matrix $\mathbf{S}_{\mathrm{M}}$ of the atomic orbitals basis subset of the C_{60} molecule: $\hat{\mathbf{P}}_{\mathrm{M}} = \sum_{m,n} |m\rangle \left[\mathbf{S}_{\mathrm{M}}\right]^{-1} \langle n|$. (Here on the sub-index M will represent the projection onto the molecular subspace.) In order not to loose essential information in the projection process, the Hamiltonian projected onto the molecule, $\hat{\mathbf{P}}_{\mathrm{M}}\hat{\mathbf{H}}^{0}\hat{\mathbf{P}}_{\mathrm{M}} := \mathbf{H}^{0}_{\mathrm{M}}$, must be supplemented by a self-energy obtained from reversal engineering of the projected Green's function $\hat{\mathbf{P}}_{\mathrm{M}}\hat{\mathbf{G}}^{0}\hat{\mathbf{P}}_{\mathrm{M}} := \mathbf{G}^{0}_{\mathrm{M}}$, where $\hat{\mathbf{G}}^{0}$ is the retarded Green's function operator of the whole system[150]. The self-energy matrix, as represented in the basis set, reads

$$\mathbf{\Sigma}^{0}_{\mathrm{M}} = (\omega - \mu)\,\mathbf{S}_{\mathrm{M}} - \mathbf{H}^{0}_{\mathrm{M}} - \mathbf{S}_{\mathrm{M}}[\mathbf{G}^{0}_{\mathrm{M}}]^{-1}\mathbf{S}_{\mathrm{M}}. \tag{7.1}$$

Here ω is the energy and μ the chemical potential which enforces the bound charge condition

$$\begin{aligned} &\int \rho^{0}(\mathbf{r})d\mathbf{r} - N_0 = \\ &-\frac{2}{\pi} Im \int_{-\infty}^{0} \left(\int \left\langle \vec{r}|\hat{\mathbf{G}}^{0}|\vec{r}\right\rangle d\vec{r} \right) d\omega - N_0 = 0, \end{aligned} \tag{7.2}$$

where N_0 is the total number of electrons of the molecular bridge and ρ^0 is the total electronic density. In what follows the index 0 will refer to the initial

DFT calculation which is not allowed to break spin symmetry, as required by our impurity solver.
The eigenstates of $\mathbf{H}^0_{\mathrm{M}}$ are MO's modified by the electrodes. Since this Hamiltonian results from a full DFT calculation of the molecular bridge several effects such as the crystal field and charge transfer induced by the electrodes already change the spectrum with respect to that of the bare molecule. Figure 7.3 (b) shows the relevant part of the spectrum of $\mathbf{H}^0_{\mathrm{M}}$. As can be appreciated, the five-fold and three-fold degeneracies of the HOMO and LUMO, respectively, are partially removed by the interaction with the electrodes and the charge transfer.
Since charge transfer naturally occurs from the Au electrodes to the molecule, our active space will be composed of the first 3 LUMO's, later augmented by the next 3 for reassurance. Likewise, if a gate voltage removes charge from the molecule and takes the chemical potential into the HOMO's one should consider these 5 levels instead. Importantly, it must be borne in mind that these KS levels already carry electronic interactions which must be removed before including correlations. Usually, when correlations involve only one atom, this double counting correction problem is taken care of by parametrized atomic Coulomb and exchange terms. Since our goal is to obtain a free-of-parameters theory, we propose a new idea based on CDFT techniques. In essence we propose to empty the active space before adding the correlations through the interaction integrals between MO's.
CDFT is a self-consistent ground state technique designed to directly construct charge and spin constrained states. In general, the CDFT makes use of a density functional giving the energy $E[\rho]$ and adds a Lagrange multiplier term representing the constrain to yield a new functional. In our model this functional is given by

$$\begin{aligned} E[\rho, V_{\mathrm{M}}, \mu] = E[\rho] + V_{\mathrm{M}} \left(\int \omega_{\mathrm{M}}(\mathbf{r}) \rho(\mathbf{r}) d\mathbf{r} - N_{\mathrm{M}} \right) + \\ \mu \left(\int (1 - \omega_{\mathrm{M}}(\mathbf{r}) \rho^0(\mathbf{r}) d\mathbf{r} + \int \omega_{\mathrm{M}}(\mathbf{r}) \rho(\mathbf{r}) d\mathbf{r} - Q \right). \end{aligned} \tag{7.3}$$

The weighting factor ω_{M}, in the simplest case, is 1 in the volumetric region of the molecule and 0 elsewhere, N_{M} is the charge in the molecule (constrained to be integer), and V_{M} the Lagrange multiplier or potential that ultimately controls this charge. For completeness of notation we have included the term that controls the overall charge of the system, Q. This number is chosen in such a way that the charge in the electrodes remains the same as that of the 0-calculation. Furthermore, at this point we could carry out a standard CDFT calculation. However, the purpose of our CDFT is to remove the charge that later will be added along with correlations through the impurity solver. Besides, we will use the hybridization function $Im\mathbf{\Sigma}^0_{\mathrm{M}} \equiv -\pi\Delta^0_{\mathrm{M}}$ corresponding to the original 0-calculation and the original charge of the molecule Q_{M}. In fact, after the impurity solver step, the resulting charge in the molecule should be essentially the same as that of the 0- calculation. Therefore, we choose to freeze the electron density of the electrodes (thereof the presence of ρ^0 in Eq. 7.3) and find in a self-consistent manner only the projected density of the molecule ρ_{M} and the projected Hamiltonian $\mathbf{H}^-_{\mathrm{M}}$ constrained to have

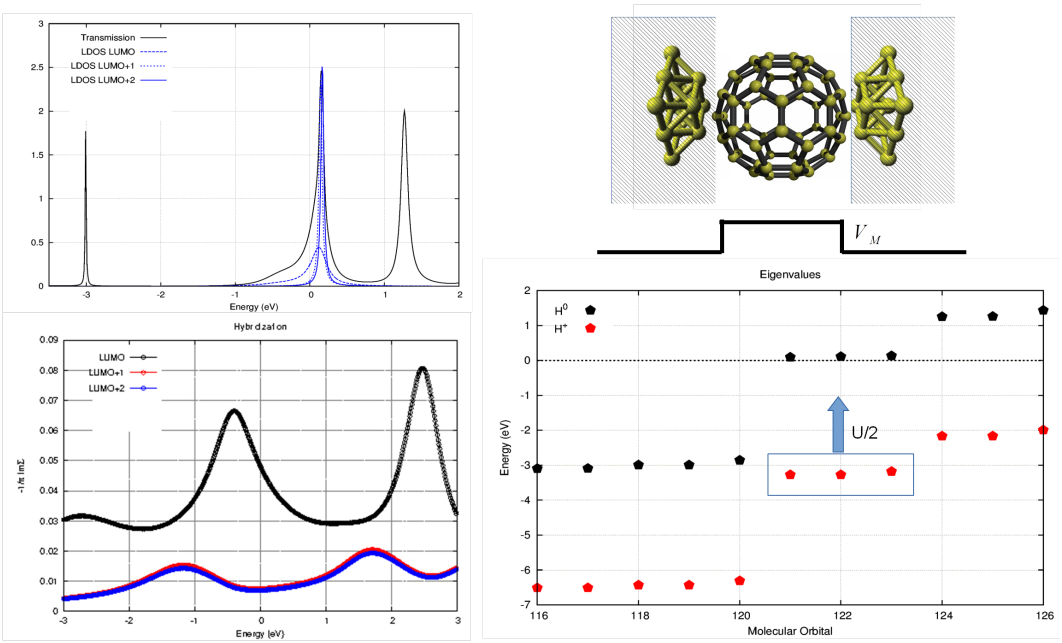

Fig. 7.4: (a) Local density of states projected onto the three LUMO's orbitals (b) Hybridization function projected onto the same orbitals. (The active space). (c) Toy picture to show the effect of the V_M potential. (d) Evolution of the eigenvalues of the Hamiltonian near the active space region showing the effect of the CDFT.

$N_{\rm M}(< Q_{\rm M})$ electrons. In practice the charge in the molecule is computed after projecting the charge density and integrating:

$$\begin{aligned}\int \rho_{\rm M}(\mathbf{r})d\mathbf{r} &= -\frac{2}{\pi}Im\int_{-\infty}^{0}\left(\int\left\langle \mathbf{r}|\hat{\mathbf{P}}_{\rm M}\hat{\mathbf{G}}^0\hat{\mathbf{P}}_{\rm M}|\mathbf{r}\right\rangle d\mathbf{r}\right)d\omega \\ &= -\frac{2}{\pi}Im\int_{-\infty}^{0}Tr\left\{\mathbf{G}_{\rm M}(\omega)[\mathbf{S}_{\rm M}]^{-1}\right\}d\omega\end{aligned} \tag{7.4}$$

In the 0-calculation we obtain $Q_{\rm M}\approx 242$ due to charge transfer from the electrodes (the number of electrons for the neutral C_{60} is 240, which here is chosen to be the value of $N_{\rm M}$). In any case, as shown below, this number can be tuned at will through μ as if a gate voltage was present.
We are now ready to include many-body effects beyond the DFT level. We will follow the DMFT+impurity solver method developed by D. Jacob et. al. [76, 135]. Fig. 7.4 shows the level spectrum of the "emptied" system $\mathbf{H}_{\rm M}^{-}$.
The second ingredient is the electron-electron interaction terms for the active space, which augment the single-particle Hamiltonian: $\mathbf{H}_U = \sum_{\alpha\beta\gamma\delta\sigma\sigma'}U_{\alpha\beta\gamma\delta}\hat{\mathbf{c}}^\dagger_{\alpha\sigma}\hat{\mathbf{c}}^\dagger_{\beta\sigma'}\hat{\mathbf{c}}_{\gamma\sigma'}\hat{\mathbf{c}}_{\delta\sigma}$. The integrals U can be easily computed from those of the atomic orbitals $\phi(\mathbf{r})$:

$$U_{ijkl} = \int d^3\mathbf{r}d^3\mathbf{r}'\phi^\dagger_{i\sigma}(\mathbf{r})\phi^\dagger_{j\sigma'}(\mathbf{r}')\phi_{k\sigma'}(\mathbf{r}')\phi_{l\sigma}(\mathbf{r})V(\mathbf{r}-\mathbf{r}').$$

through the unitary transformation $\mathbf{X}$ defined by the eigenvectors of $\mathbf{H}_{\rm M}^{-}$:

$$U_{\alpha\beta\gamma\delta} = \sum_{ijkl}X^\dagger_{\alpha i}X^\dagger_{\beta j}U_{ijkl}X_{k\gamma}X_{l\delta}. \tag{7.5}$$

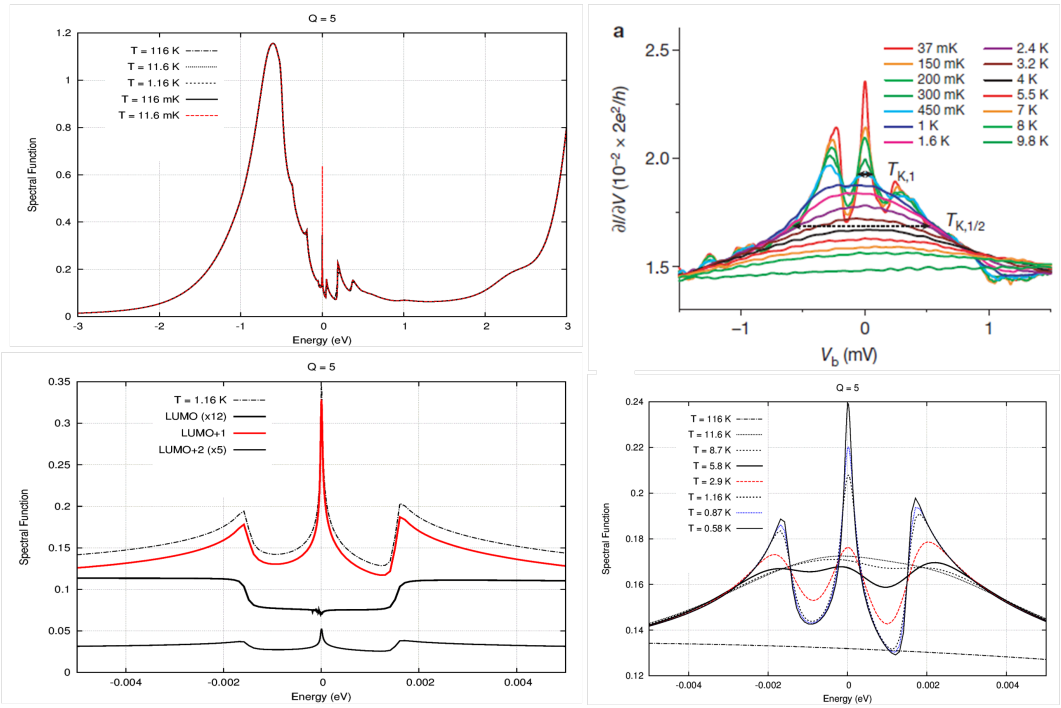

Fig. 7.5: Kondo resonance showing the singlet-triple transition.

We will reserve the Greek letter labels for the molecular orbitals basis set. In table X we show the direct Coulomb repulsion ($U_{\alpha\alpha\alpha\alpha}$, $U_{\alpha\beta\beta\alpha}$) and the exchange interaction ($J \equiv U_{\alpha\beta\alpha\beta}$) for the three LUMO's of the C_{60} molecule. These are unscreened interactions.

The final ingredient is the hybridization function $\Delta^0_{\rm M}$ describing the (dynamic) coupling of the molecular levels to the rest of the system and transformed to the new basis of MO's. In the same way, we should include the real part of the non-interacting self-energy, $\Re\mathbf{\Sigma}^0_{\rm a}(\mathrm{h}^-_{\rm a})$, at the energy of the impurity level, a, to include the splitting of the impurity levels due to the coupling with the electrodes. Notice that this term is not included in the Hubbard-type Hamiltonian, but with the dynamical correlations. This completes our first-principles Anderson impurity model (AIM).

In addition to obtain the singlet-triplet transition previous observed in this system [142], in the first instance we will propose to introduce a gate voltage as a simple shift of the impurity levels. Since the real part of the non-interacting self-energy is energy-dependent, the coupling with the leads is too. The inclusion of this term allows us to include the change in the splitting of the eigenstates of the empty non-interacting Hamiltonian due to the gate voltage in both, the dynamical correlations and the Hubbard-type Hamiltonian, taking always the value of the self-energy at the energy of the impurity level, i.e. $\Re\mathbf{\Sigma}^0_{\rm M}(\mathrm{h}^-_{\rm a})$. In Fig. 7.4 we show the spectrum of $\mathbf{H}^-_{\rm M} + \Re\mathbf{\Sigma}^0_{\rm M}(\mathrm{h}^-_{\rm a})$.

Solving the AIM problem yields the interacting self-energy $\Sigma^{\rm c}$. This self-energy is a dynamical correlation add(above, onto) to the non-interacting Green's function, $\mathbf{G}_{\rm a} = [(\omega-\mu)\mathbf{I}_{\rm a} - \mathrm{h}_{\rm a} - i\pi\Delta_a - \Sigma^c_{\rm a}]^{-1}$, which gives the spectral function for the correlated molecular level, a. Note that $\mathrm{h}_{\rm a} = \mathrm{h}^-_{\rm a} + \Re\mathbf{\Sigma}^0_{\rm a}(\mathrm{h}^-_{\rm a})$. Including the dynamical correlations into the non-interacting retarded Green's

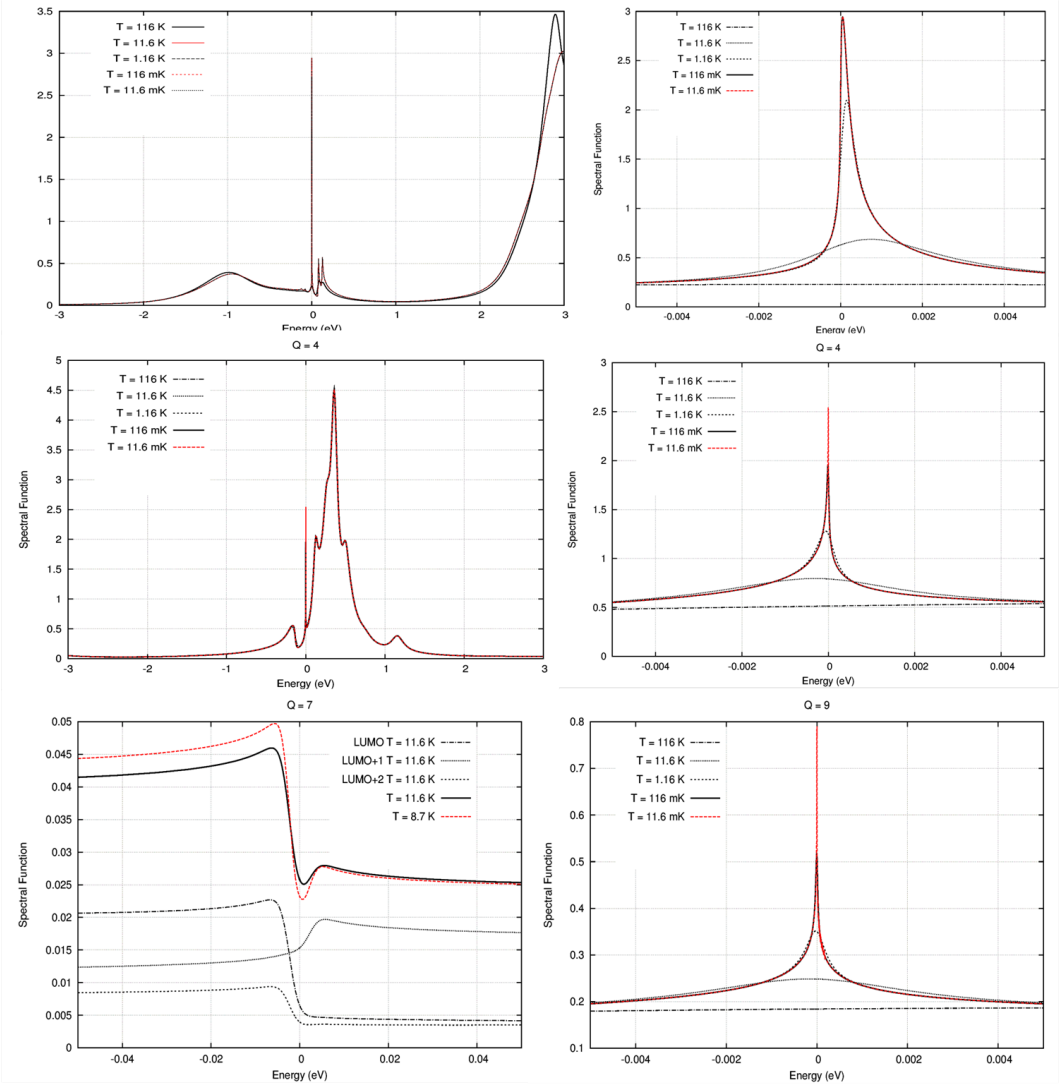

Fig. 7.6: Kondo resonance to different gate voltage.

function,

$$\mathbf{G} = [(\omega - \mu)\mathbf{I}_{\rm AS} - \mathbf{H}^{-}_{\rm AS} - \mathbf{\Sigma}^{\Delta}_{L,\rm AS} - \mathbf{\Sigma}^{\Delta}_{R,\rm AS} - \Sigma^{c}_{\rm AS}]^{-1}, \tag{7.6}$$

gives an useful expression for the transmission function in terms of Landauer-Butikker equation, $T = Tr[\mathbf{G}^{\dagger}\mathbf{\Gamma}_R\mathbf{G}\mathbf{\Gamma}_L]$. In the above equation the subindex AS stands by " Active space". The The differential conductance is thus obtained by $T = Tr[\mathbf{A}_{\rm R}\mathbf{\Gamma}_L]$, where $\mathbf{\Gamma}_L$ is the coupling matrix defined by $\mathbf{\Gamma}_L = i[\Sigma_{L,AS} - \Sigma^{\dagger}_{L,AS}]$.

Part III

II Part: Magnetoresistance

Chapter 8

Magnetoresistance in Mn-Based system

8.1 Green's Function approach to the tunneling problem.

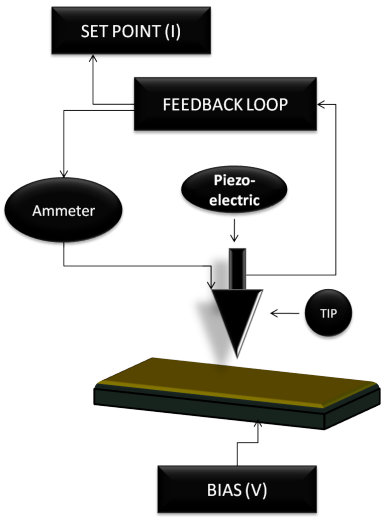

In STM an extremely sharp conducting tip (in the best case monoatomic) is brought into close proximity to a conductive sample, typically a few Angstroms. Applying a small bias voltage between the tip and the surface gives rise to a nanoamperometric current. To obtain 2D images, the motion of the tip is controlled by a piezo-electric material. As the name implies, this technique is based on the quantum tunneling effect. For electrons in the two conductors the gap between them represents an impenetrable energy barrier which cannot be overcome according to classical theory, but since electrons are quantum mechanical objects, electrons can tunnel through the barrier and a tunneling current between the tip and the surface can take place. Therefore, the obtained images are related to the tip and sample density of states, shown as different color scales or monochromatic hues. In STM, several operational modes can be used to scan the surface. The two most important modes are the so called constant height mode and constant current mode. Working in constant height mode the tip surface distance is kept constant and the changes in the current are measured. In contrast, the constant current mode keeps constant the tunneling current using a feedback system to adjust the tip-surface distance. In this mode, brighter areas appear as due to a greater density of states. These brighter areas are also related to higher elevations of the surface, hence allowing us to obtain a topographic image. So far we have not mentioned the dependence of the DOS on the spin degree of freedom.

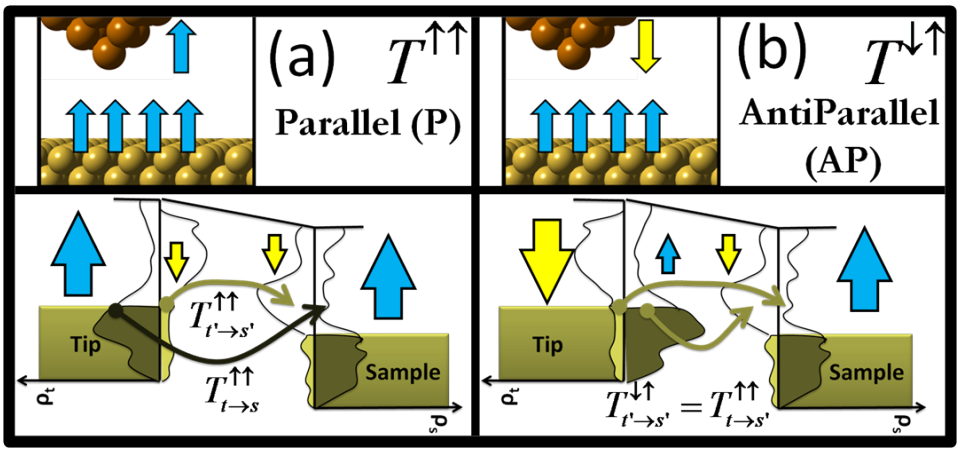

Fig. 8.1: Schematic representation of density of states convolution between a tip and a surface. Blue and yellow arrows represent the relative magnetic orientation of the tip and the surface to each other. In the a-case(b-case), the magnetic orientation of the tip and the surface is the same(opposite), the elastic electron tunneling from the tip to the surface is represented by curved arrows. $T^{\uparrow\uparrow}(T^{\downarrow\uparrow})$ means that majority density of states on tip and surface are parallel(antiparallel) as we show in a-case(b-case). $t(s)$ and $t'(s')$ are relative to the alpha and beta spin density of states of the tip(sample).

For magnetic materials the density of states splits up and there is a net imbalance between the occupation of electrons whose spin is oriented in one direction and the opposite. In the SP-STM techniques the tip is spin polarized and can thus obtain information on the polarization of the surface or the sample. The SP-STM is based on the fundamental property of magnetic materials, i.e., the imbalance in occupation of electrons with different spins. Due to the quantum mechanical exchange interaction between electrons, the density of states splits up into minority and majority states, dubbed down and up states or beta and alpha. The imbalance causes a spin polarization, in contrast to non-magnetic materials, in which the number of up and down electrons are identical. The splitting of the density of states has important consequences on the tunneling current, as Julliere [151] showed in 1975. In fact, Julliere's model assumes that the tunneling current is determined solely by the spin polarization obtained from the spin-split electronic density of states of the magnetic surface at the Fermi energy.

When electrons tunnel between two magnetic materials, the magnitude of the current is influenced by the magnetization of the two materials. This phenomenon is called **T**unneling **M**agneto**R**esistance effect, (TMR), and originates from the fact that the probability for an electron to tunnel through the barrier depends on the DOS convolution. The tunneling conductance depends on the relative orientation of the magnetization of the two electrodes. For parallel orientation, the convolution of alpha-alpha, beta-beta DOS usually is higher than for antiparallel orientation, where the convolution is now alpha-beta, beta-alpha. It's easy to see why that is true in the figure 8.1. Normally when the system have the same magnetization direction, is easy that the same polarization densities of states for the tip and the sample are of the same scale. Nevertheless, there is not any reason to think that this picture is always true and in this work we will talk about that. The quantum conductance for the

SP-tunnel current following the Landauer formalism is:

$$G_{Parallel} = G_P = \frac{e^2}{h}\left[T^{\uparrow\uparrow}_{t\to s} + T^{\uparrow\uparrow}_{t'\to s'}\right] \tag{8.1}$$

$$G_{AntiParallel} = G_{AP} = \frac{e^2}{h}\left[T^{\downarrow\uparrow}_{t\to s} + T^{\downarrow\uparrow}_{t'\to s'}\right] = \frac{e^2}{h}\left[T^{\uparrow\uparrow}_{t'\to s} + T^{\uparrow\uparrow}_{t\to s'}\right] \tag{8.2}$$

t(s) refers to the alpha spin density of states of the tip(surface), while t'(s') refers to beta spin density of states. In the antiparallel case, we have interchanged the alpha and beta spin densities for the tip, exactly as we can see in figure 8.1. The difference between the parallel and antiparallel conductance can be written as:

$$Diff(G) = \frac{e^2}{h}\left[G_P - G_{AP}\right] = \frac{e^2}{h}\left[T^{\uparrow\uparrow}_{t\to s} + T^{\uparrow\uparrow}_{t'\to s'} - T^{\downarrow\uparrow}_{t\to s} - T^{\downarrow\uparrow}_{t'\to s'}\right] \tag{8.3}$$

The P and AP conductances are generally not identical and $Diff(G) \neq 0$, leading to a variation of the tunneling current with the magnetic configuration of the electrodes, and allowing for the emergence of magnetic contrast spectroscopy. The tunneling magnetoresistance is defined then as:

$$TMR(\%) = \frac{G_P - G_{AP}}{G_P + G_{AP}}\,100 \tag{8.4}$$

The TMR value can be positive or negative. When the value of TMR is negative we talk about the negative tunneling magnetoresistance. Normally, the TMR is positive because the convolution of the majority densities of states (Parallel case) is usually larger than the mix convolution between the majority and minority density of states (antiparallel case). However, when the density of states changes abruptly at the Fermi level, the TMR can take negative values and complicate the interpretation of STS images since in this case the magnetic contrasts are reversed.

8.2 The electronic structure of the Mn surface.

The manganese grows on Fe (001) surface with tetragonal body center structure (TBC). In this structure, the magnetic coupling between the manganese layers is antiferromagnetic. This surface is very reactive owning to 4eV Work Function.

We have reproduced this surface using two levels of theory. First, using CRYSTAL, we have studied a periodic surface formed by seven layers of Manganese in the TBC structure, and with two layers of ghost atom on top and on the bottom of the surface. The use of ghost atom is recommended to obtain a good surface work function.

In this calculation we have chosen a triple Aldrich complete basis set [37] without pseudofunctional, and the GGA approximation in the functional,

BPBE functional [152]. We have obtained that the antiferromagnetic coupling between layers in this system is energetically more favorable than the ferromagnetic coupling. In the figure 8.2, we show the Density of state of this surface, computed using the CRYSTAL code [153].

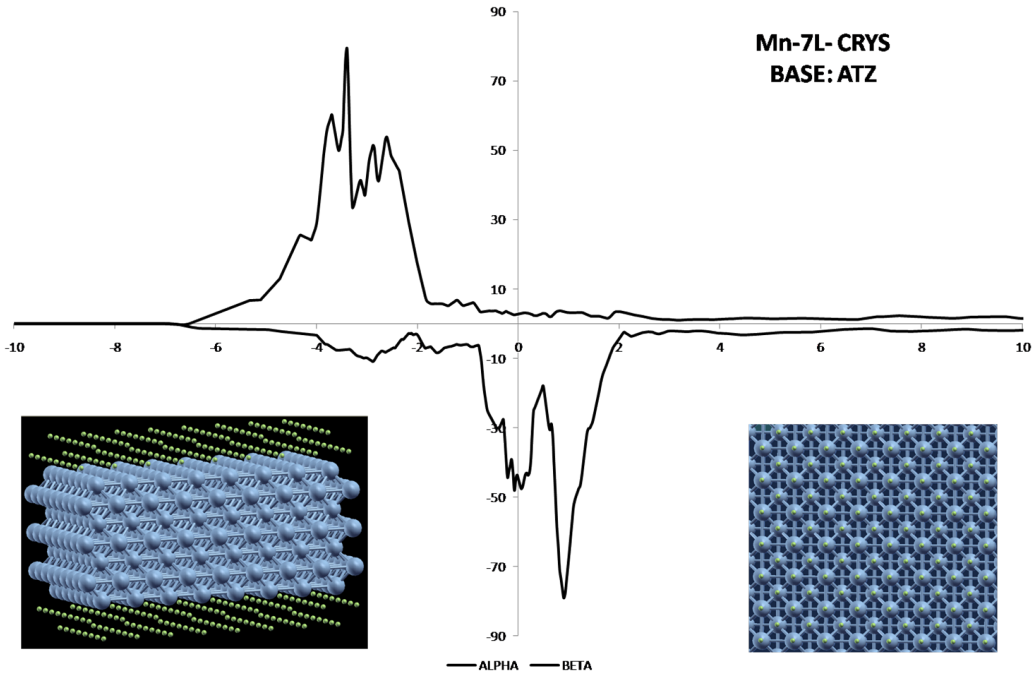

Fig. 8.2: Density of States of Mn surface.

Taking in account that we want realize the study of this surface in Gaussian, we have reduced the number of layers with the aim to compare this periodic surfaces with the finite surface or cluster computed in Gaussian. In this calculation we also have changed the base of the calculations because in Gaussian we need to use the smallest possible base.

In Gaussian we have formed a small cluster of 64 atoms. The basis set now is the CBL, i.e. the total compress CRENBL base, and the CBLE is the same base extended in the valence orbitals, i.e. s and d orbitals. In figure 8.3 we have shown the comparative DOS plots for this system:

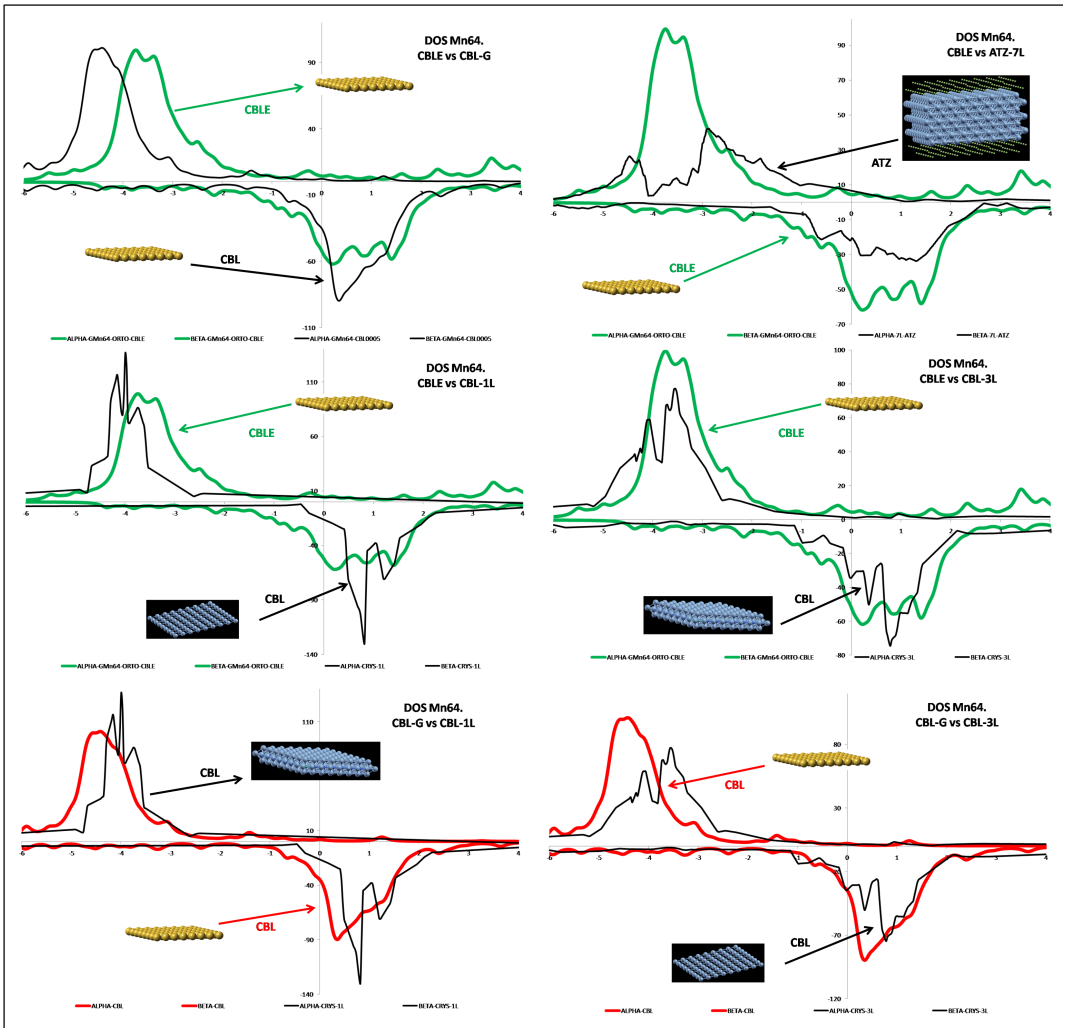

Fig. 8.3: In this figure we have shown different density of states plots. The Hamiltonian of yellow surfaces are computed using the Gaussian code [154] and the Densities of States have obtained using the Green's Functions formalism. (see appendix C for details). Blue surfaces and their corresponding densities of states are computed with CRYSTAL code. With the aim to compare these plots, we have used differents basis set and different number of layers.

Chapter 9

Inverse Magnetoresistance in Magnetic Metals

9.1 Inverse Magnetoresistance in Magnetic Metals in tunneling regimen.

When a bias voltage is applied between two ferromagnetic metallic materials separated by a thin insulating or metallic barrier, the generated current depends on the relative orientation of the spin magnetization. When parallel, the current I_{P} is generally larger than when anti-parallel (I_{AP}). This difference lies at the heart of the magnetoresistance phenomenon which soon after its discovery[155] found its way into applications. Typically defined as $MR = (I_{\mathrm{P}} - I_{\mathrm{AP}})/(I_{\mathrm{P}} + I_{\mathrm{AP}})$, the most extended idea is that the MR is positive, i.e., $I_{\mathrm{P}} > I_{\mathrm{AP}}$, which can be naturally understood in terms of the convolution of the density of states (DOS) of the two magnetic electrodes at the Fermi energy. The opposite case, the inverse magnetoresistance when $I_{\mathrm{P}} < I_{\mathrm{AP}}$ is much less frequent[156–158] and not so easily rationalized.
Spin-polarized scanning tunnelling microscopy (SP-STM) exploits the difference between I_{P} and I_{AP} to characterize magnetic surfaces. Since the current changes with the relative spin orientation between the magnetic tip and the sample, the SP-STM can be used to map regions of different spin orientations within otherwise identical crystallographic structure areas. For instance, high-spin metals such as Co, Fe, or even Mn are frequently used in SP-STM studies. Usually these materials appear as isomorphic growths of magnetic metals on metal surfaces. Well-known examples are Co growth on Cu(111)[159–161] or W growth on Cr(001). Another interesting material is Mn(001) which is obtained by depositing Mn on Fe(001). The isomorphic growth onto Fe forms a layered structure with the typical BCC crystal structure of Fe, showing an unusual antiferromagnetic coupling between layers. This peculiar magnetic structure has also been revealed on Cr surfaces by SP-STM. After choosing a magnetic tip, typically Mn or Fe, the magnetic superstructure appears as a current contrast between terraces or areas whose sign may change with the sign of the bias voltage or even the magnitude.
For magnetic characterization purposes of single-element surfaces as the ones mentioned above, it matters little whether the tunnelling magnetoresistance

(TMR) is positive or negative. However, when SP-STM addresses surfaces with different materials such as magnetic molecules on magnetic surfaces or the same material with different crystallographic environments, it is crucial to know whether the TMR is expected to be positive or negative. For instance, if the TMR changes from positive to negative depending on whether the tip is on the substrate or on the molecule, the wrong conclusion can be drawn regarding the important aspect of the relative magnetic orientation between regions. In fact, inverse TMR (I-TMR) have been experimentally reported in recent years by several groups in quantum confined systems such as molecular and metallic nanocontacts and magnetic nanoislands.

Although the SP-STM is a powerful tool to study magnetic surfaces, it is not easy to determine the tip-surface relative magnetic orientation in absence of magnetic field. Actually, SP-STM in magnetic fields where the magnetoresistive phenomenon itself (i.e., a change in the resistance with applied magnetic fields) is exploited is not so common. Theoretical techniques based on density functional theory (DFT) are thus essential for a full understanding of the experimental results. Here we model SP-STM in systems based on magnetic transition metals of the first row of periodic table (from Mn to Ni) concluding, contrary to commonly accepted wisdom, that the TMR is usually negative for all of them. This finding is further rationalized in terms or orbital contributions to the TMR effect.

The spin-resolved tunnelling current is computed using spin-unrestricted first-principles calculations in the framework of DFT and in combination with the non-equilibrium Green's function formalism as implemented in our ANT.G code [59]. This code interfaces with Gaussian09 [53] which works with localized orbital basis sets. The bias voltage V is accounted for in a fully self-consistent manner as explained in Ref. louis. In all cases we have used a general gradient approximation through the Becke and Perdew-Becke-Ernzerhof exchange-correlation functional [33, 35] The current is obtained by direct integration of the energy-dependent and bias-dependent transmission function $T(V,\omega)$:

$$I_{\mathrm{P(AP)}}(V) = \frac{e}{h}\int_{\epsilon_{\mathrm{F}}-eV/2}^{\epsilon_{\mathrm{F}}+eV/2} T_{\mathrm{P(AP)}}(V,\omega)d\omega, \tag{9.1}$$

where ϵ_{F} is the Fermi energy of the system in equilibrium and P and AP denote parallel and anti-parallel spin configurations. The transmission is in turn given by

$$T = Tr[\mathbf{\Gamma}_{\mathrm{T}}(\omega,V)\mathbf{G}^{-}(\omega,V)\mathbf{\Gamma}_{\mathrm{S}}(\omega,V)\mathbf{G}^{+}(\omega,V)]. \tag{9.2}$$

The dependence on energy and bias voltage will be assumed and dropped from the expressions from now on. In Eq. 9.2 the matrix $\mathbf{\Gamma}_{\mathrm{T(S)}}$ is obtained from the self-energy representing the bulk part of the tip (T) or substrate (S): $\mathbf{\Gamma} = i[\mathbf{\Sigma}^{\dagger} - \mathbf{\Sigma}]$, and $\mathbf{G}^{(\mp)} = lim_{\eta\to 0}\hat{\mathbf{G}}(\omega \pm i\eta)$ is the advanced(retarded) Green's function.

We have investigated various tip/surface systems such as Mn/Mn(001), Fe/Fe(001), Co/Co(111), and Ni/Ni(111) systems, as well as a prototypical Ni nanocontact to compare with previous results. In all cases the surfaces and tips are modelled using from two to four layers embedded in a minimal (*spd*) tight-binding Bethe lattice model (see insets in 9.1 for details). In all cases

various sets of parameters for the Bethe lattice have been tested, the main conclusions being unaffected by the particular choice. We have also considered a minimal basis set (*spd*) for all atoms attached to the Bethe lattice. The others atoms have been defined by a LANL2DZ basis set. All tips have been modelled within a pyramidal shape [149], following the crystal structure of the surface.

We will first discuss the Mn/Mn(001) system. This surface is an isomorphic growth of Mn on an Fe(001). The Mn/Fe(001) surface has a BCC crystal structure, typical of Fe, with an anti-ferromagnetic coupling between layers. The BCC structure of Mn is slightly distorted with respect to the Fe one with a 0.166 nm interlayer distance and a lattice constant of $a =$, (data obtained from previous experiments and calculations. We have considered two different three-layered Mn surfaces of sizes 113 atoms (not shown) and 41 atoms [see Fig. 9.1(h-j)]. Since the atomic and magnetic structure of the experimental tips are unknown, we have considered two different models for the tips, both ferromagnetic with a BCC(001) crystal growth. The first one is built with a Mn bulk lattice constant of $a =$ and used for the larger surface. The other tips [see insets in Figs. 9.1 (h-j)] are built with an Fe lattice constant ($a =$) as if Mn is just wetting an Fe tip and go along with the smaller surfaces. The latter choice is inspired in recent experiments. The first model is thus less compacted than the other ones.

In Figs. 9.1 (a-b) we show the P and AP current for the first model of the Mn/Mn(001) system. We have computed a range of distances from a near contact regimen (0.5 nm) to a pure tunnelling regime (0.9 nm), but we only show the two extreme cases. Notice that the distances are measured from the center of the apex tip atom to the center of the central surface atom. As we can observe, the Mn/Mn(001) system has highly asymmetric conductance with bias polarity. Its current-voltage characteristics presents a typical diode behaviour. It also presents a negative differential resistance at positive bias. The diode-like behaviour has been experimentally reported with an Fe tip. Most importantly, for negative bias we obtain the expected positive TMR, but, for positive bias we observe that $I_{\mathrm{AP}} > I_{\mathrm{P}}$, i. e., we obtain an I-TMR. In the insets one can see the actual values which, as regards the I-TMR are fairly independent of the distance while the TMR goes to zero for negative bias as the distance increases. The inversion of the TMR with the sign of the bias voltage has been experimentally reported before in a similar Co-based system. In Figs. 9.1(c-d) we show the P and AP current for the other models of the Mn/Mn(001) system. In all these cases, the tip-surface distance is kept at 0.9 nm, and we have studied the influence of the tip shape from atomically sharp to plane tips.

As we can see in the I-V graphs, the TMR behavior is the same, i.e. negative at positive bias and positive in the other bias direction. We can also observe that the absolute value of the TMR decreases as compared with the previous model of less compacted tip and, in general, with the planarity of the tips. The diode-like behavior seems to be characteristic of sharp tips since it tends to disappear for the planar ones [see Fig. 9.1(d)]. The negative differential resistance has also disappeared from the bias window considered.

To gain insight into the shape of the I-V curves and into the origin of the

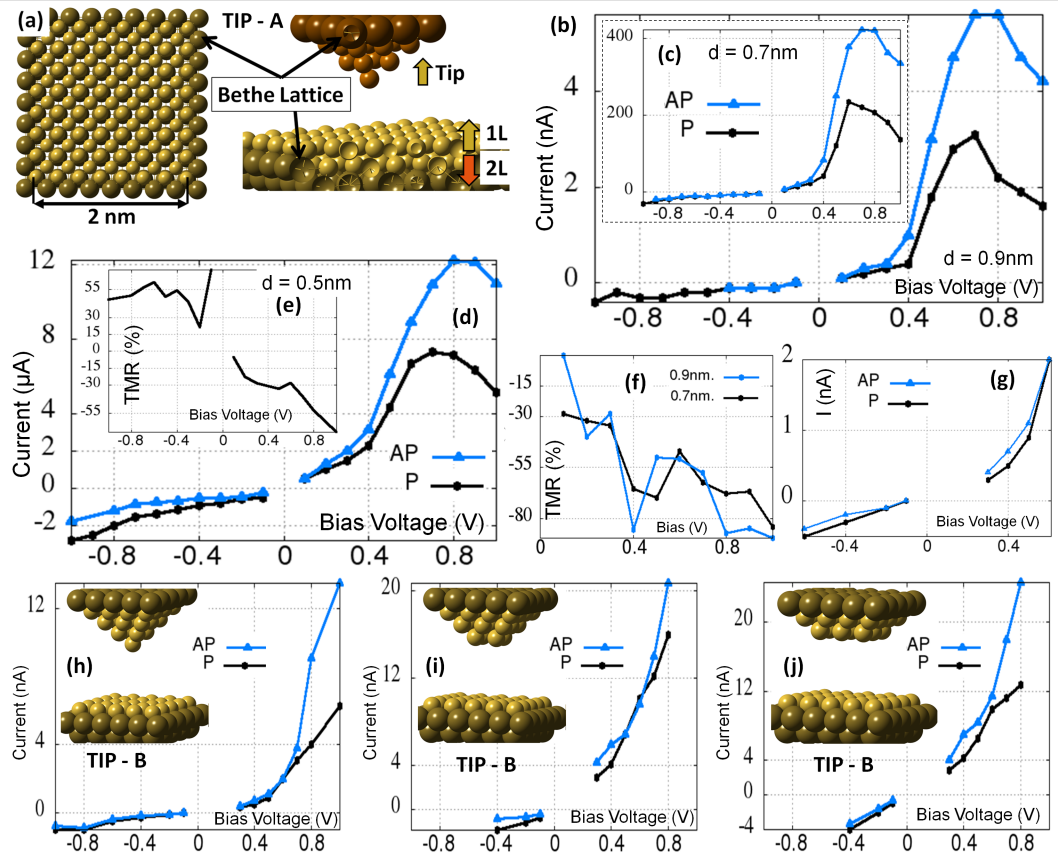

Fig. 9.1: All distance in this picture have been measured consider the atoms likes dots. (a) Schematic picture of the computed Mn(001) surface (TIP-A). (b,c,d) Spin polarized current and (e,f) TMR of the system schematized in insert (a). (g-j) Spin Polarized current with different B-type tips. (g) The current of the system drew in insert (h) at low bias.

I-TMR, we propose to resolve the transmission function given in Eq 9.2 in atomic orbitals. It is well-known that one cannot obtain useful information from the individual diagonal elements of the transmission matrix. Reducing the Green's function of the whole system by projecting it onto a few tip atoms avoids this problem. Following the projector theory for non-orthogonal basis sets developed by us in a previous work[150], we can obtain the reduced transmission function. This is done by performing two consecutive projections. The first one is a projection onto all tip atoms:

$$\hat{\mathbf{P}}_{\rm tip}\hat{\mathbf{G}}\hat{\mathbf{P}}^{\dagger}_{\rm tip} = \hat{\mathbf{P}}_{\rm tip}\left[\omega\hat{\mathbf{I}} - \hat{\mathbf{H}} - \hat{\mathbf{\Sigma}}_{\rm T} - \hat{\mathbf{\Sigma}}_{\rm S}\right]^{-1}\hat{\mathbf{P}}^{\dagger}_{\rm tip}.$$

where $\hat{\mathbf{H}}$ is the Hamiltonian operator of the atomically defined full system and $\hat{\mathbf{I}}$ is the identity operator with a representation in the non-orthogonal basis set given by the overlap matrix $\mathbf{S}$. After performing the projection one can obtain the self-energy matrix that replaces the whole substrate (not only the bulk part S represented by the Bethe lattice) by reversal-engineering: $\mathbf{\Sigma}^{\rm tip}_{\rm S} = \omega\mathbf{S}_{\rm tip} - \mathbf{H}_{\rm tip} - \mathbf{\Sigma}^{\rm tip}_{\rm T} - [\tilde{\mathbf{G}}_{\rm tip}]^{-1}$, where $\mathbf{\Sigma}^{\rm tip}_{\rm T} =: \hat{\mathbf{P}}^{\dagger}_{\rm tip}\hat{\mathbf{\Sigma}}_{\rm T}\hat{\mathbf{P}}_{\rm tip}$ (the symbol =: stands for "is the representation of") and $\mathbf{H}_{\rm tip}$ is the tip Hamiltonian represented in the non-orthogonal basis set. The tilde in $\tilde{\mathbf{G}}$ means that the Green's function is represented in the dual basis set, $\tilde{\mathbf{G}} = \mathbf{S}^{-1}\mathbf{G}\mathbf{S}^{-1}$. The

second projection is performed onto the apex tip atoms (ata):

$$\hat{\mathbf{P}}_{\text{ata}}\hat{\mathbf{G}}_{\text{tip}} : \hat{\mathbf{P}}^{\dagger}_{\text{ata}} = \hat{\mathbf{P}}_{\text{ata}}\left[\omega\hat{\mathbf{I}}_{\text{tip}} - \hat{\mathbf{H}}_{\text{tip}} - \hat{\mathbf{\Sigma}}^{\text{tip}}_{\text{T}} - \hat{\mathbf{\Sigma}}^{\text{tip}}_{\text{S}}\right]^{-1}\hat{\mathbf{P}}^{\dagger}_{\text{ata}},$$

from which the final expression of the projected self-energies is obtained: $\mathbf{\Sigma}^{\text{ata}}_{\text{T}} = \omega\mathbf{S}_{\text{ata}} - \mathbf{H}_{\text{ata}} - \mathbf{\Sigma}^{\text{ata}}_{\text{S}} - [\tilde{\mathbf{G}}_{\text{ata}}]^{-1}$ and $\mathbf{\Sigma}^{\text{ata}}_{\text{S}} =: \hat{\mathbf{P}}^{\dagger}_{\text{ata}}\hat{\mathbf{\Sigma}}^{\text{tip}}_{\text{S}}\hat{\mathbf{P}}_{\text{ata}}$. The double projection just described becomes essential in the contact regime, not so much in the tunnelling regime. In the latter case a single-shot projection can also be done.

Now we propose to rewrite Eq. 9.2 as $T = Tr[\tilde{\mathbf{A}}\mathbf{\Gamma}_{\text{S}}]$. Here $\tilde{\mathbf{A}}$ is the spectral function defined by $\tilde{\mathbf{A}} = \tilde{\mathbf{G}}^{+}\mathbf{\Gamma}_{\text{T}}\tilde{\mathbf{G}}^{-}$ [162]. Application of the projector theory explained above results in a transmission function which can be essentially reduced to information at the apex tip atoms and allows us to study the orbital contribution to the current directly from the diagonal elements of the transmission function:

$$T = Tr[\tilde{\mathbf{A}}_{\text{ata}}\mathbf{\Gamma}^{\text{ata}}_{\text{S}}] = 2\pi\sum_{i=s,p,d}\tilde{A}_i\Delta_i + \sum_{i\neq j}\tilde{A}_{ij}\Gamma_{ji}. \tag{9.3}$$

Here we have used the standard definition of hybridization function as $\Gamma_{ii} = 2\pi\Delta_{ii}$.

In the quantum transport context the hybridization function gives direct information of how open or closed atomic orbitals are for conduction; in this case the apex orbitals. The second term in the above equation represents the mixing of the orbitals due to the coupling and is usually smaller than the first term. The transmission function, to a very good extent, can always be read from the first term of the above equation.

Now the different orbital contributions to the current can be separated as well as the role played by the density of states (DOS) and the hybridization function. We plotto observed in the systems plotted in figure 9.1, we have represented in Fig. 9.2 the transmission (9.2.a), the atomic orbital resolved transmission (9.2.b), the LDOS (9.2.c1) and the Δ function (9.2.c2) for the system drew in the figure 9.1(h,g) at $-0.4/0.4$V.

In fig. 9.2(a) we can see that the AP current is higher than the P at positive bias, but not a negative bias in where the current is essentially not polarized. In fig 9.2(b) we can observed that the transmission is essentially due to a s-orbital. At positive bias we can observe a small d-orbital contribution to the transmission only in one spin orientation. This contribution is due to the compaction of the tip and it has a d_{z^2} character. This unexpected contribution of the d-orbital to the transmission is responsible for the inversion of the TMR, in this case from negative to positive, at 0.6V in the system with a high compacted tip (TIP-B) represented in fig. 9.2(d). We can assume that high compacted tips favor a strong hybridization between the s and d_{z^2} orbital which induces a positive TMR when the hybridization function is strong enough.

In general, the hybridization function of s-orbital in metallic systems out of the contact regimen is always one or more orders of magnitude higher than the rest of orbitals. As we can see in fig. 9.2(c) the LDOS is not enough to explain the inversion of the TMR or the diode effect. Notice that the LDOS of

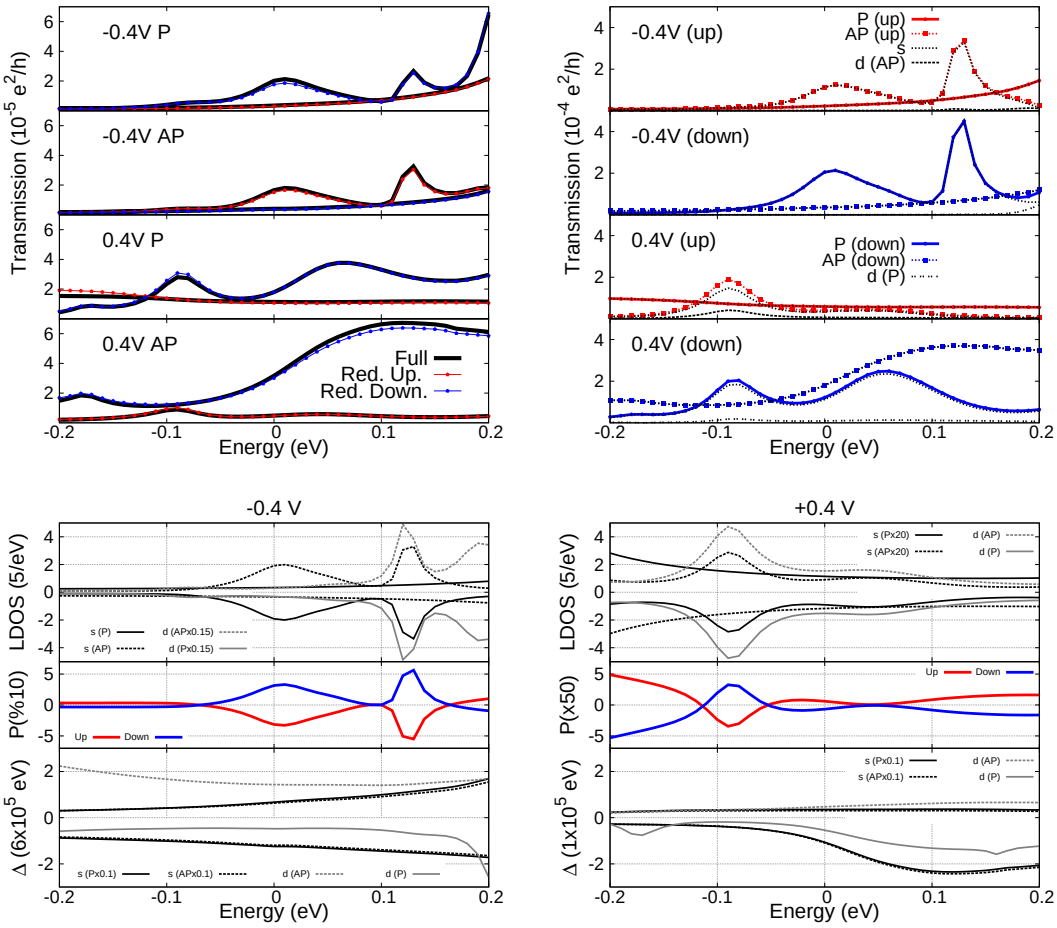

Fig. 9.2: (a-e) Analysis of the system drew in fig. 9.1(h). (a) Transmission function in the P (a1) and AP (a2) cases. In black we have plotted the transmission from the Eq. 9.2. In Red and blue we have used the Eq. 9.3. (b) Transmission function from the first term of the Eq. 9.3. Up (b1) and down (b2) contribution. (c) LDOS (c1) and Δ (c2). In green and red at 0.4V and in black at -0.4V. (d) Transmission from Eq. 9.3. System drew in Fig. 9.1(i) at 0.6V. The insert show a zoom at this bias. (e) LDOS and Δ. System drew in Fig. 9.1(a) at 0.9 nm.

s-orbital is higher at negative bias, where the current is negligible. In addition, the LDOS is essentially symmetric under an inversion of polarization, which not allows a magnetoresistive effect. Though the LDOS is not asymmetric under a change of polarization, the Δ yes it is. Hence the magnetoresistance is due to a strong asymmetric hybridization of s-orbital with the up/down spin channel in the surface. In the present case, this hybridization is independent of the spin polarization of the tip and the inversion of TMR is thus controlled by the difference in the available s-LDOS in the down channel.

Finally we can explain the tunnel effect and the NDC observed in fig. 9.1(b-d) for low compacted tips. In figure 9.2(e) we have represented the LDOS and the hybridization function of this system projected onto the orbital channel responsible for the transmission function. In this case the transmission is only controlled by the s atomic orbital channel. Concretely the transmission is due to the s-down spin channel because the hybridization function in the s-up channel is very low. In addition we can observe that the tunnel diode effect observed in theses systems is due to the absence of LDOS at negative bias. In contrast the NDC is due to the decrease in the hybridization function at

high voltage and hence, the NDC is due to a resonant tunneling. The resonant tunneling is due to localized tip states, since small displacements of the apex atom tip can generate a second tunnel barrier and the concomitant resonant tunneling effect.
We have studied this effect in other transition metals.
Near the contact regimen the antiparallel current is higher than the parallel current in all studied cases. As we can see in the graphs when we move to the tunneling regimen, the difference between the parallel and the antiparallel current is reduced. The limit of this reduction is the Co case in which the TMR is return normal.

Chapter 10

MnPc on Mn surface.

10.1 Manganese Phthalocyanine on Manganese little cluster.

In this section we have proposed a simplified model for the surface formed by four or five manganese atoms. To study the magnetic interaction in this model, we have proposed two different cases showed in figure 10.1:

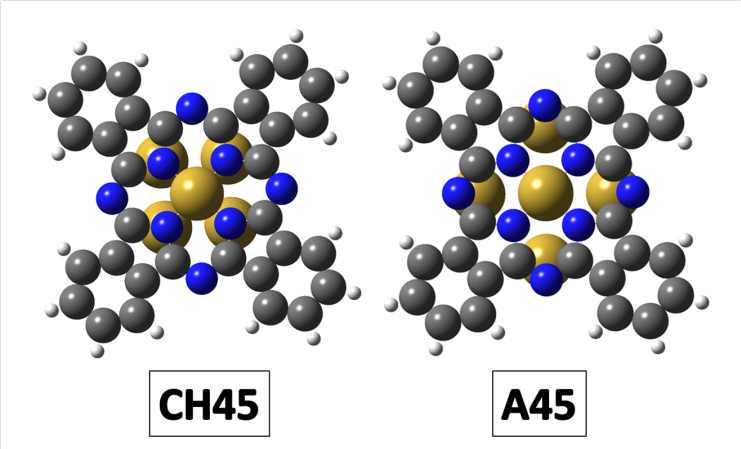

Fig. 10.1: Simple Model representation. MnPc on Mn little cluster

In the figure 10.1, the $CH45$ model represents the case where the MnPc is adsorbed on a hollow position on the Mn surface. This surface is represented in a simplified form by four manganese atoms, and should be emphasized that in this simplified model the four nitrogen atoms, painted in blue in the figure 10.1, lie on four the tetragonal body center (TBC) manganese surface. The $A45$ model is adsorbed on top position on the simplified five manganese atoms surface, with the four nitrogen atoms lie on a bridge formed between two manganese atoms of the surface. Of course, four or five atoms is not a surface, but, we assume with this model that the magnetic coupling is not dependent the surface properties, but rather only dependent the kind of exchange.

To analyze the electronic structure of these two simple models, we have represented the spin of the MnPc and the energy of the system as a function of the

multiplicity. See figure 10.2. The results in this case are the same that we have obtained by the dimer model. In the case where the MnPc is on top position on the little cluster formed by five manganese atoms, the magnetic interactions leaves an antiferromagnetic coupling, ($A45$ model), with a coupling constants of: $J = 0.0745eV$. The positive sign of the constant highlights the fact that the coupling is antiferromagnetic.

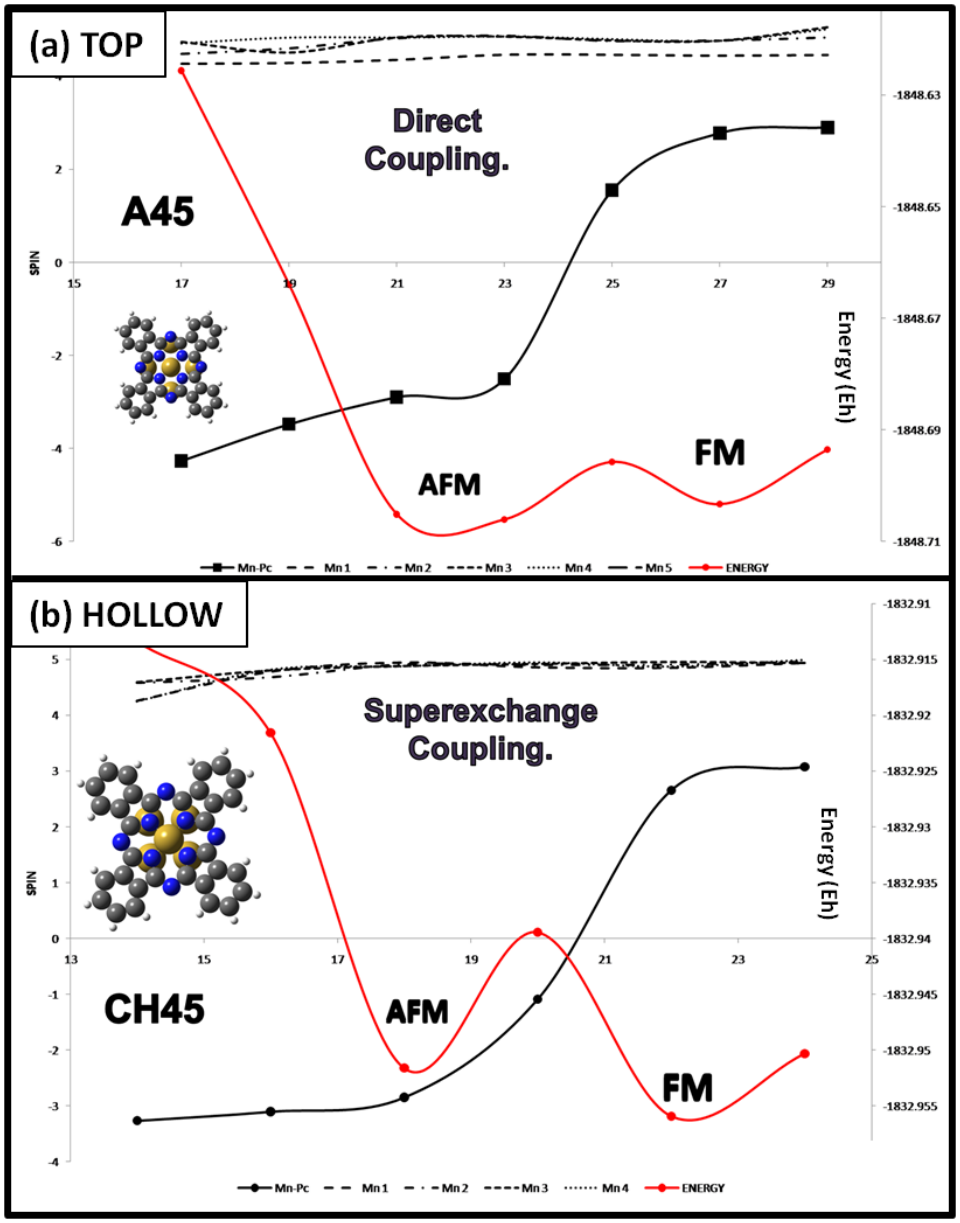

Fig. 10.2: In this figure in red we have shown the variation of the energy with the multiplicity of the system ($M = 2S + 1$). Black lines show the evolution of MnPc spin and dashed lines show the spin of surface manganese atoms.

The figure 10.2 shows a clear image of the antiferromagnetic - ferromagnetic transition. The red line represents the energy of the system as a function of the multiplicity. In the $CH45$ case we can see that the magnetic coupling in is ferromagnetic. The continuous black line shows the spin of the central manganese atom of the Phthalocyanine. Dashed line show the spin distribution

of the manganese atoms of the simplified surface, and we can observed that the magnetic moment of the surface remains unchanged basically. The coupling constant in the $CH45$ case is: $J = -0.1173eV$, the sign is negative because the coupling is ferromagnetic.

10.2 MnPc on Mn. The Adsorption Geometry

With the aim to understand the magnetic contrast images in the manganese phthalocyanine adsorbed on a manganese surface, we have carried out first-principles studies on the structural and electronic properties of this system. We have used a small monolayer cluster formed by sixty four atom of manganese with a manganese phthalocyanine molecule adsorbed on it. Our calculations were performed using density functional theory with generalized gradient approximation (GGA) implemented in Gaussian code [154]. The Becke exchange gradient correction and the Perdew-Burke-Ernzerhof correlation gradient correction were used, i.e. the so called BPBE functional [152]. The basis set consists of the double set calls LANL2DZ for the molecule and CRENBS for the surface [37]. The limits of this functional and this set of basis have been demonstrated in a previous section for the isolated systems. To study the adsorption geometry of the molecule, we have proposed several initial adsorption configurations including hollow (CH type), top (A type) and Bridge or Line (L type) sites. We can see these adsorption geometries in figure 10.3. In all cases we have studied two different rotation of the molecule, 45 and 0 degrees, about the principal axis of the surface.

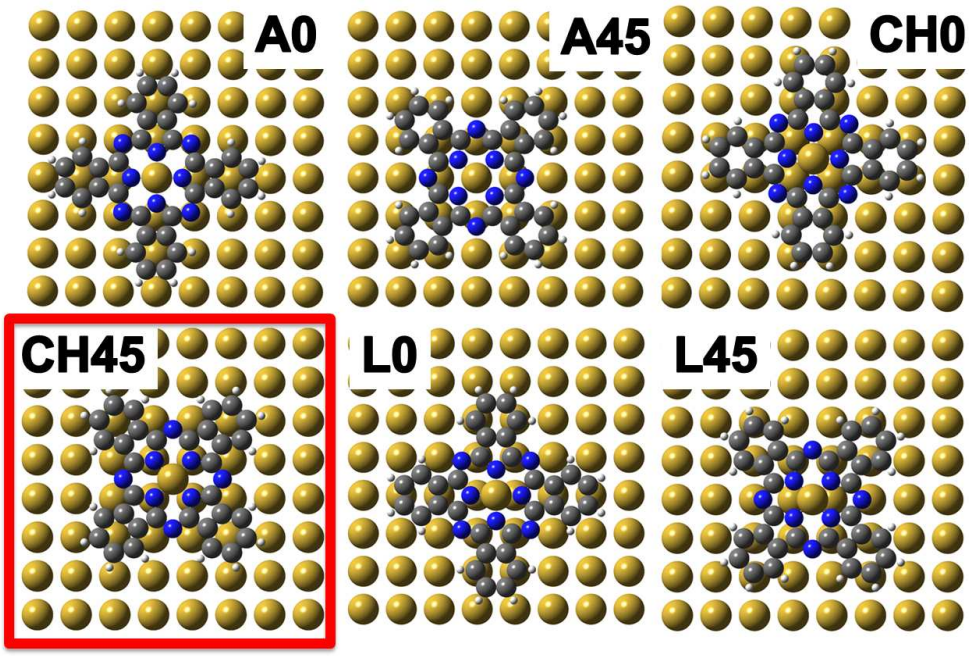

Fig. 10.3: Different adsorption geometries of the MnPc on Mn surface. The A letter A means that the molecule is adsorbed on top position. CH refers to hollow position adsorption site, and L refers to bridge position adsorption site. In all cases we have shown two different rotation of the molecule about the principal axis of the surface: 45 and 0 degrees. The red square shows the adsorption position of minimum energy.

Differences between these proposed structures lie in the position of the central manganese atom of the molecule in relationship with manganese atoms of the surface and the interaction of the four nitrogen atoms of the molecule with these surface atoms. In the hollow site the central manganese atom of the molecule lies on a hollow position formed by four manganese atoms of the surface. In addition, when the molecule is rotated forty five degrees regarding the principal axis of the surface, four nitrogens of the molecules lie on top of manganese atoms of the surface. The direct interaction between nitrogen atoms and manganese surface atoms is relevant because the orbital overlapping results in short-ranged interaction due the localization of atomic wave function where the magnetic superexchange mechanism can be invoked. Top-type adsorption sites leave the central manganese atom of the molecule in direct contact with a surface manganese atom. Bridge-type adsorption sites deposit the manganese atom of the molecule between two manganese atoms of the surface contained on a line.

In each possible adsorption sites is necessary to study all possible spin configurations for the total system, the so called multiplicity (M), $M = 2S+1$ as well as the equilibrium distance for each one of these spin values. Once done, we have obtained that the adsorption site of minimum energy is the hollow type site where the molecule is rotated forty four degrees regarding the principal axis of the surface.

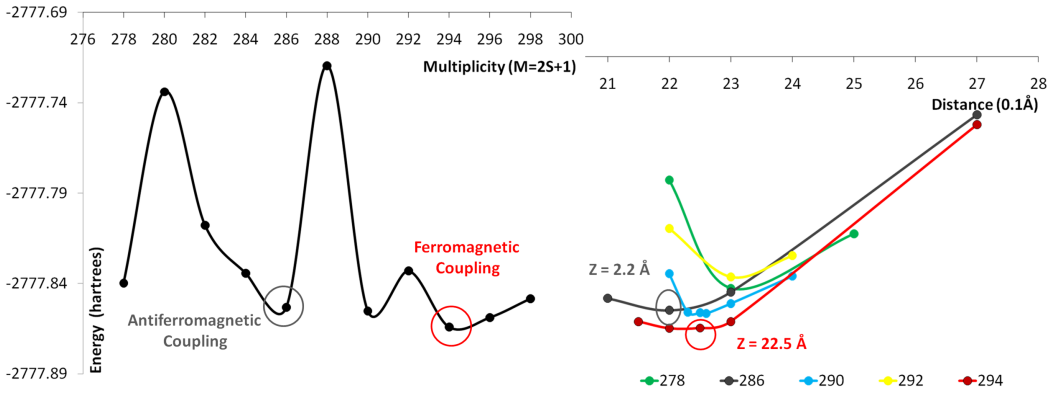

The equilibrium distance between the molecule and the surface is 2.3$\mathring{A}$. In this point, the magnetic coupling between the molecule and the surface is antiferromagnetic. The exchange mechanism is expected to be via superexchange through four atoms of nitrogen. So, this ferromagnetic coupling is compatible with Kanamori-Goodenough rules, and it is in agreement with the previous results obtained for most simple models. It was observed that after adsorption the charge transfer is very high, several electrons. With the aim to improve the charge transfer we have studied other basis set. Concretely, we have studied our system using the so called CRENBL basis set with compressed in two different levels. First, we have use the CRENBL compressed totally, the so called CBL basis set. The end basis set that we have used is the compressed CRENBL basis set, where valence orbitals have been extended. This basis set

is what we call CBLE basis set. The charge transfer is of eight electrons in the CRENBS basis set, of five electrons in the CBL basis set and of three electrons in the CBLE basis set. The direction of the charge transfer is in all cases from the surface to the molecule. In all cases we have obtained that the organic part of the molecule (the rest of the molecule that does not contain hydrogen or metallic atoms), is spin polarized due to the high charge in the molecule. Also, we have obtained that the magnetic moment of the manganese atom of the molecules remains unchanged despite the charge transfer. The change in the number of transferred electrons, that we have obtained when we change the basis set, is due to the change in the metal work function that take place, when we have changed the basis set. The work function of the Mn surface is around $-1.5eV$ for CRENBS basis set, $-2.2eV$ for CBL basis set and $-3.2eV$ for CBLE basis set. This last value is near to the convergence value of the work function of this surface. Also is near to the experimental work function, (around $-4.0eV$).

In summary, in all cases that we have studied the adsorption distance is around $2.4\mathring{A}$ and the magnetic coupling always is ferromagnetic. This result is in agreement with simple models exposed previously in the section 3.4.3.

Conclusion

In the first part of this thesis, we could say in summary that we have studied the correlated electronic structure of a MnPc adsorbed on the Pb(111) surface and on the Bi(110), as the CO-MnPc/Bi(110), fully taking into account the strong electronic correlations originating from the Mn $3d$-shell. Our results show that the adsorption does not essentially modify the total spin $S = 3/2$ of the molecule, being distributed among four of the five $3d$-orbitals, in the case of the MnPc on Pb(111), and in contrast with the MnPc on Bi(110), where the spin state is reduced to $S = 1$.
We further find that the experimentally observed asymmetric Kondo resonance in the MnPc on Pb(111) system [25, 99] is due to an underscreened Kondo effect where a spin 1/2 in the Mn $3d$-shell remains unscreened. The Kondo resonance in the tunnel spectra actually stems from only one of the Kondo-screened orbitals. Its peculiar lineshape arises from the modulation of the hybridization function due to a strong coupling to the organic ligand, not being necessary to invoke the superposition of two Kondo peaks with different Kondo temperatures as done in Ref. [25].
In the case of the MnPc on Bi(110) we have also found an underscreened Kondo effect due to the unhybridizated d_{xy} orbital. And in the case of the CO-MnPc we have attempt to defense a mix-valenced regimen due to the charge fluctuations.

We have also presented a fully first-principles approach to the Kondo problem in purely carbon-based molecules where the screened spin may be an unpaired π electron delocalized over many atoms such as in the case of C_{60}. Our starting point is a projection of the full Kohn-Sham Hamiltonian onto the molecule followed by a selection of the active space, e.g., a selection of the relevant molecular orbitals. A constrained density functional calculation has allowed us to avoid the double-counting correction problem. Once we have obtained the appropriate single-particle levels along with the hybridization function, the spectral density and transmission function was computed through a DMFT impurity solvent. We have applied this technique to a C_{60} molecule contacted by gold electrodes. By gating the system we study the zero-bias features arising in the mixed-valence regimen, the spin 1/2 Kondo, and the underscreened $S = 1$ Kondo regimes, where we have obtained the single-triplet transition, in agreement with the experiments.

In the last part of this thesis we have demonstrated that the TMR is usually negative in all transition metals from Mn to Ni. The high TMR observed in

these systems is due to a spin polarization symmetry broken in the hybridization function. The sign of TMR is controlled by the polarization of s-orbital, changing with the sigh of the bias voltage. Out of the contact regimen, the sporadic presence of d-orbitals strongly hybridized with the surface can induce a positive TMR following the Julliere's assumption.

Appendix A: More about Density Functional Theory

The Kohn-Sham equations

One year later, Kohn and Sham, making use of the density functional developed by Hohenberg and Kohn, proposed a self consistent method to solve the Schrödinger equation, based on the Hartree's method, but including the exchange and correlation effects [17]. The fundamental ansatz of the Hartree's method is that any many-electron wave function can be written as a product of a single electron wave function:

$$\Psi(\vec{r}_1, ..., \vec{r}_N) = \phi(\vec{r}_1)...\phi(\vec{r}_N) \tag{1}$$

The goal of Kohn-Sham approximation was to introduce an auxiliary system of non-interacting electrons, with the same density of the original one, and described by orthonormal wavefuncitons $\langle\phi_i|\psi_j\rangle = \delta_{ij}$.

$$n(\vec{r}) = \sum_{i=1}^{N} |\phi_i(\vec{r})|^2 \tag{2}$$

The universal density-energy functional, $G[n]$, proposed by Hohenberg and Kohn now is written as:

$$F[n] = \frac{1}{2}\int \frac{n(\vec{r})n(\vec{r}\,')}{|\vec{r} - \vec{r}\,'|} d\vec{r}d\vec{r}\,' + G[n]$$

$$G[n] = T[n] + E_{XC}[n] \tag{3}$$

where $T[n]$ is the kinetic energy of the auxiliary system of non-interacting electrons. $E_{XC}[n]$ is the exchange-correlation energy functional accounting for all the many-body effects. If the condition that the electronic density distribution, $n(\vec{r})$, varys sufficiently slowly, $\int \delta n(\vec{r}) d\vec{r} = 0$, is established, then:

$$E_{XC}[n] = \int n(\vec{r}) \in_{XC} [n(\vec{r})] d\vec{r} \tag{4}$$

Here $\in_{XC}$, is the exchange and correlation energy per electron of a uniform

electron gas of density n. The minimization of $F[n]$ can now be done and one-electron Schrödinger equations can be approximated by:

$$\left\{-\frac{1}{2}\nabla^2 + v_{ext}(\vec{r}) + v_{int} + \mu_{XC}[n(\vec{r})]\right\}\phi_i = \in_i \phi_i(\vec{r}) = \hat{H}_{KS}\phi_i(\vec{r}) \tag{5}$$

Where $\mu_{XC}[n(\vec{r})]$ is the Lagrange parameter derived in the Hohenberg-Kohn theory, whose physical meaning is the chemical potential, but now, this potential is expressed in terms of the exchange and correlation effects.

$$\mu_{XC}[n(\vec{r})] = \frac{d\left\{n \in_{XC} [n(\vec{r})]\right\}}{dn} \tag{6}$$

A self-consistently solution of the one-electron Schrödinger equations, leads the ground state total energy of the system given by:

$$E = \sum_{i=1}^{N} \in_i - V_{ee} + \int n(\vec{r})\left\{\in_{XC} [n(\vec{r})] - \mu_{XC}[n(\vec{r})]\right\} d\vec{r} \tag{7}$$

Where $\in_i$ is a Kohn-Sham eigenvalue, which only has physical meaning when $\in_i = \in_N$, whereas N is the total number of electrons. In other words, the eigenvalue $\in_N$ is the energy of the highest occupied eigenstate and determines the location of the Fermi surface.[163]
Self-Consistent Kohn-Sham equations can be reduced to Self-consistent Hartree equations neglects the many body exchange-correlations effects; Nevertheless, kohn-Sham equations can not be resolved exactly, as can be those of Hartree, because the exact exchange-correlations potential is unknown. This fact fixes the importance of choosing the functional, since the practical usefulness of density functional theory depends entirely on whether approximations for the functional $E_{XC}[n]$ could be found, which are at the same time sufficiently simple and sufficiently accurate.

The Hohenberg-Kohn Theorem

In 1964, based on the Thomas-Fermi theory, Hohenberg and Kohn introduced a universal functional $F[n(\vec{r})]$ where the density was the basic variable. They developed an exact formal variational principle for the ground state energy of an interacting electron gas in an external potential [30]. The goal of this theory was to show that given an external potential, $v_{ext}(\vec{r})$, not only the Hamiltonian is fixed, but also this potential, $v_{ext}(\vec{r})$ is a unique functional of the electronic density, $n(\vec{r})$.

$$\hat{H} = \hat{T} + \hat{V}_{ee} + \hat{V}_{ext} = \frac{1}{2}\int \nabla\psi^*(\vec{r})\nabla\psi(\vec{r})d\vec{r} + \frac{1}{2}\int \frac{\psi^*(\vec{r})\psi^*(\vec{r}\,')\psi(\vec{r}\,')\psi(\vec{r})}{|\vec{r} - \vec{r}\,'|}d\vec{r}d\vec{r}\,' + \\ + \int v_{ext}(\vec{r})\psi^*(\vec{r})\psi(\vec{r})d\vec{r} \tag{8}$$

$$n(\vec{r}) = \langle \Psi \left| \psi^*(\vec{r})\psi(\vec{r}) \right| \Psi \rangle \tag{9}$$

Since Ψ is the ground state for the electronic density $n(\vec{r})$, if we suppose now that another potential $v'_{ext}(\vec{r})$ has the same $n(\vec{r})$ electronic density in the ground state Ψ', and assume that Ψ and Ψ' satisfy different Schrödinger equations: $\hat{H}\Psi = E\Psi$ and $\hat{H}'\Psi' = E'\Psi'$; It easy to show that whereas E and E' are the ground states energies, the initial assumption is inconsistent.

$$E' = \left\langle \Psi' \left| \hat{H}' \right| \Psi' \right\rangle < \left\langle \Psi \left| \hat{H}' \right| \Psi \right\rangle = E - f\left(v_{ext} - v'_{ext}\right) \tag{10}$$

$$E = \left\langle \Psi \left| \hat{H} \right| \Psi \right\rangle < \left\langle \Psi' \left| \hat{H} \right| \Psi' \right\rangle = E' - f\left(v'_{ext} - v_{ext}\right) \tag{11}$$

$$f\left(v'_{ext} - v_{ext}\right) = -f\left(v_{ext} - v'_{ext}\right) \tag{12}$$

$$\begin{aligned} \mathbf{E}+\mathbf{E'} < E_{\Psi'} + E'_{\Psi} &= E' - f\left(v'_{ext} - v_{ext}\right) + E - f\left(v_{ext} - v'_{ext}\right) = \\ &= E' + E - f\left(v'_{ext} - v_{ext}\right) + f\left(v'_{ext} - v_{ext}\right) = \mathbf{E'}+\mathbf{E} \end{aligned} \tag{13}$$

Therefore, $v_{ext}(\vec{r})$ is a unique functional of $n(\vec{r})$, and also, Ψ, the ground state, is a functional of $n(\vec{r})$. Taking into account this theorem, Hohenberg and Kohn proposed a universal energy functional $E[n]$, i.e. independent of the number of particles and the external potential, $v_{ext}(\vec{r})$:

$$E[n] = \int v_{ext}(\vec{r})n(\vec{r})d\vec{r} + F[n] \tag{14}$$

$F[n]$ also is a universal density functional defined in terms of classical Coulomb energy (the electron-electron interaction similar to that used in the Thomas Fermi theory). $G[n]$ involves the kinetic energy term, and as we have commented in the main text, the exact definition of this term is unknown. Then Hohenberg and Kohn proposed that G[n] was a universal energy-density functional defined in terms of the one-particle density matrix, $n(\vec{r}) = n_1(\vec{r}, \vec{r}\,')$, and where the correlation and exchange energies have been taken into account.

$$F[n] = \frac{1}{2}\int \frac{n(\vec{r})n(\vec{r}\,')}{|\vec{r} - \vec{r}\,'|} d\vec{r}d\vec{r}\,' + G[n] \tag{15}$$

$$G[n] = \frac{1}{2}\int \nabla_{\vec{r}}\nabla_{\vec{r}\,'} n_1(\vec{r}, \vec{r})d\vec{r} + \frac{1}{2}\int \frac{C_2(\vec{r}, \vec{r}\,')}{|\vec{r} - \vec{r}\,'|} d\vec{r}d\vec{r}\,' \tag{16}$$

$$C_2(\vec{r}, \vec{r}\,') = n_2(\vec{r}, \vec{r}\,'; \vec{r}, \vec{r}\,') - n_1(\vec{r}, \vec{r})n_1(\vec{r}\,', \vec{r}\,') \tag{17}$$

Where $n_2(\vec{r},\vec{r}\,';\vec{r},\vec{r}\,')$ is the two-particle density matrix, and $C_2(\vec{r},\vec{r}\,')$ is the two-particle correlation energy. To minimize the functional is necessary to keep constant the number of electrons. The variational principle proposed by Hohenberg and Kohn reduces to the problem of, first, finding the minimum among 3N-dimensional many-body wave function with a given density,

$$E = min_{\Psi} \left\langle \Psi(\vec{r}_1 ... \vec{r}_N) \left| \hat{H} \right| \Psi(\vec{r}_1 ... \vec{r}_N) \right\rangle \tag{18}$$

and then finding the minimum of a 3-dimensional density function: $E = min_{n(\vec{r})} E[n(\vec{r})]$. Hohenberg and Kohn also demonstrated that if we neglect the exchange and correlations effects, we can approximate the kinetic energy for a free electron gas as: $G[n] = \frac{3}{10} \left[k_F(n)\right]^2 n$, where K_F is the Fermi momentum given by $K_F = \left(3\pi^2 n\right)^{1/3}$. Applying the calculus of variations, they obtained the following Thomas-Fermi equation:

$$n(\vec{r}) = \frac{1}{3\pi^2} \left\{2 \left[\mu - v_{ext}(\vec{r}) - v_{int}(\vec{r})\right]\right\}^{3/2} \tag{19}$$

$$\nabla^2 v_{int}(\vec{r}) = -4\pi n(\vec{r}) \tag{20}$$

$$\nabla^2 v_{int}(\vec{r}) = -\frac{2^{7/2}}{3\pi} \left[\mu - v_{ext}(\vec{r}) - v_{int}(\vec{r})\right]^{3/2} \tag{21}$$

List of publications.

- 2014. **M. Soriano**, J.J. Palacios. Phys. Rev. B 90, 075128.
- 2013. D. Jacob, **M. Soriano**, J.J. Palacios. Phys. Rev. B 88, 134417.
- 2012. A. Stróżecka, **M. Soriano**, J.I. Pascual, J.J. Palacios. Phys. Rev. Lett., 109, 14, 147202.

Acknowledgement

Hace poco cenando con mi hermana, me dijo que pensara en algo que me hubiera hecho feliz, un momento, un lugar, en el que hubiera sido feliz. Ella salía de un curso de psicología donde trabajaban la idea de implantar un refugio en la mente de los pacientes, un lugar al que poder escaparse cuando todo lo demás parece derrumbarse y la tormenta apremia. Un lugar donde sentirse a salvo. Yo encontré mi refugio en ANT. Aquel día que me puse a jugar con el código, aunque no tenía permiso para hacerlo y me dio un error. Me dio tanta rabia no poder solucionarlo que abrí el código. Cuando lo abrí me encantó y le dije a mi jefe: "No sabéis lo que tenéis aquí". Para mí en ese momento era un mundo lleno de posibilidades. Ese instante en el que abrí el código, justo ese momento es mi refugio.

Esta tesis puede considerarse parte de un sueño. ANT originalmente fue un sueño de mi jefe, Juan José Palacios: construir un código de transporte cuántico a partir de cálculos de primeros principios. A este sueño se unió David Jacob, quien también como parte de su trabajo doctoral trabajó desarrollando ANT, y luego continuó en su post-doc desarrollando las herramientas de DMFT/impurity-solver que han ayudado a hacer posible esta tesis. Ahora el sueño de ANT también es mío, ya que junto a ellos, he podido contribuir a desarrollar en mi tesis un modelo de Kondo molecular a partir de primeros principios, exento de parámetros. Por ello, les estoy profundamente agradecida a ambos. Por haberme dejado ser parte de este sueño.

Una tesis es un camino muy largo, y hay mucha gente que te acompaña en el recorrido. Una de las personas a la que más cosas tengo que agradecerle es a mi director de tesis, Juan José Palacios. Primero tengo que agradecerle que creara ANT y ATOMELIX, un espacio para nosotros, que nos lo llevamos porque nos sentimos parte de este proyecto. Tengo que agradecerle muy especialmente su dedicación a lo largo de estos años, siendo una fuente de inspiración constante, creando siempre algo a su alrededor, con su pasión por la física, y en general por el deporte, la vida, la buena música y sus "home-made", que yo personalmente adoro. Tengo que agradecerle que haya dirigido mi tesis, pese a los malos momentos que hemos tenido, que siempre los hay. Tengo que agradecerle que siempre haya procurado que no me faltara de nada a pesar de la falta de recursos inherentes a este país, y me diera la oportunidad de trabajar primero en Alicante durante el máster y luego en Madrid durante la tesis. Tengo que agradecerle las largas tardes de discusión, en las que aprendí mucho, y no sólo de física. Tengo que agradecerle el esfuerzo que ha puesto en mi trabajo, para que acabara siendo lo mejor posible, que nunca se haya rendido, incluso cuando yo sí lo hice. Tengo que agradecerle que haya luchado contra mi día tras día

para hacerme mejor persona, para hacerme mejor científica, y gracias a él seré mejor cada día. Y muy especialmente tengo que agradecerle que pusiera un libro de abstracts de March meeting en mis manos hace ya varios años, y por supuesto que me haya permitido ir a este congreso y cruzar el atlántico. Por último me gustaría agradecerle a su familia su paciencia, porque este trabajo va a casa más de un día, y alguna vez han sufrido las consecuencias del estrés y de los deadlines. Gracias por no rendirte nunca.
Me gustaría agradecerle a David Jacob que fuera una fuente de inspiración en mis primeros años de tesis gracias a su trabajo doctoral. También tengo que agradecerle que me acogiera en Halle durante mi estancia, donde fui recibida como una más del grupo desde el primer día y pude disfrutar de momentos muy divertidos, y un "otoño de verdad". Por supuesto también tengo que brindarle un profundo agradecimiento a María, por su acogida y su atención durante estas semanas. También quiero agradecerle a David que me haya enseñado a manejar el DMFT/impurity-solver y su colaboración incondicional a esta tesis, así como todas las discusiones que hemos tenido sobre el efecto Kondo.
Así mismo quiero agradecerle muy profundamente a Reyes Calvo su apoyo a lo largo de estos años, que me haya aguantado hasta en los peores momentos, y con quien he podido tener momento y viajes maravillosos. Y por supuesto por sus discusiones científicas, que no dejan indiferente a nadie.
Tengo que agradecerle a todo el grupo de nanofísica de la universidad de Alicante que me permitieran formar parte de él durante la época del máster. Muy especialmente a Joaquín Fernández-Rossier y a Carlos Untiedt. Así mismo a todos los compañeros con los que coincidí, con los que tuve muy buenos momentos, y sigo teniéndolos, Federico Muñoz, Pedro Nel, Fernando Delgado, Carlos Sabater, David Costa, David Soriano, Daniel Gosálvez y Giovani Saenz. También tengo que agradecerles muy especialmente a María José Caturla y a James su colaboración en el mantenimiento del cluster matcon/atsimat que me ha permitido realizar parte de este trabajo doctoral, así como a Jorge a título póstumo.
También agradecerles profundamente a José Soler y Felix Yndurain que me hayan admitido en el grupo de Madrid y me hayan dejado usar los recursos del cluster krypton, sin el cual esta tesis no sería posible. Por esto también tengo que agradecerle a Stefan Biliar su trabajo como administrador del cluster, sin el cual esto no sería posible.
También me gustaría agradecerle a Jaime Merino, Guillermo y Ruben Perez las discusiones que hemos tenido en algún momento. Así como a la gente de mi grupo, que aunque los he dejado para el final, no son menos importantes. Especialmente a Elsa Prada, por los buenos momentos del último march meeting y las comidas, y porque como mujer científica y luchadora nata, es una inspiración para mi. También a Tobias Stuart y Jose Vicente. Y por supuesto a todos mis compañeros de despacho, con los que he compartido muy buenos momentos, y siempre están preocupados por mi cuando me estreso. Con muchísimo cariño a Carlos Salgado, Acharya, Nuno, Mitzli, Laura y Kike, así como a Michael, Wendel, Daniel, Linda, Mohammed, Irene y Silvia. Y a Michelle con quien pude disfrutar este verano de un curso estupendo en Copenhagen.
Muy especialmente quiero agradecerle a Nacho Pascual y Ana su atención en

la colaboración experimental que realizamos, por haberme recibido en Berlín, y por los buenos momentos que pasé con ese trabajo. Así mismo también me gustaría agradecerle a Amadeo su colaboración experimental en otro proyecto. También me gustaría agradecer al centro de computación científica de la UAM y al proyecto MareNostrum el apoyo computacional incondicional que nos han dado, y sin el cual esta tesis no sería posible.
Y por último quiero agradecerle a mi familia todo el apoyo incondicional que me han dado siempre, no hay palabras para agradecerles todo lo que significan para mí, pero me gustaría agradecerles muy especialmente que se enorgullezcan de compartir conmigo este momento.

References

[1] Gordon E Moore. "cramming more components onto integrated circuits". *Electronics*, 38(8), 1975.

[2] R. P. Feymann. “there is plenty of room at the bottom”. *Engineering & Science*, 23:5, 1960.

[3] G Binnig and H Rohrer. "in touch with atoms". *Rev. Mod. Phys.*, 71(2):324, 1999.

[4] L. Ruan, F. Besenbacher, I. Stensgaard, and E. Laegsgaard. “atom resolved discrimination of chemically different elements on metal surfaces”. *Phys. Rev. Lett.*, 70(26):4079–4082, Jun 1993.

[5] K. E. Drexler. “engines of creation. the coming era of nanotechnology”. *Anchor Books.*, 1986.

[6] R. F. Curl, H. W. Kroto, and R. E. Smalley. "nobel prize in chemistry 1996".

[7] A. G. MacDiarmid A. J. Heeger and H. Shirakawa. “nobel prize in chemistry 2000”.

[8] A. Aviram and M. Ratner. “molecular rectifiers”. *Chem. Phys. Lett.*, 29:277, 1974.

[9] S. J. vd. Molen and P. Lilijeroth. “charge transport through molecular switches”. *J. Phys.: condens. Matter*, 22:133001, 2010.

[10] Christian Wäckerlin, Dorota Chylarecka, Armin Kleibert, Kathrin Müller, Cristian Iacovita, Frithjof Nolting, Thomas A. Jung, and Nirmalya Ballav. Controlling spins in adsorbed molecules by a chemical switch. *Nature Communications*, 1(5):1–7, August 2010.

[11] D. Cahen, A. Kahn, and E. Umbach. “energetics of molecular interfaces”. *Materials Today*, July/August:32, 2005.

[12] J. Singleton. “band theory and electronic properties of solids”. *Oxford University Press*, Oxford Master Series in Condensed Matter Physics.(Oxford.), 2008.

[13] M. Cinchetti, K. Heimer, J.P Wï¿½stenberg, O. Andreyev, M. Bauer, S. Lach, C. Ziegler, Y. Gao, and M. Aeschlimann. “determination of

spin injection and transport in a ferromagnet/organic semiconductor heterojunction by two-photon photoemission". *Nature Materials*, 8:115, 2009.

[14] M Reyes Calvo, Joaquin Fernandez-Rossier, Juan José Palacios, David Jacob, Douglas Natelson, and Carlos Untiedt. The kondo effect in ferromagnetic atomic contacts. *Nature*, 458(7242):1150–1153, 2009.

[15] WJ De Haas, J De Boer, and GJ Van den Berg. The electrical resistance of gold, copper and lead at low temperatures. *Physica*, 1(7):1115–1124, 1934.

[16] P. Hohenberg and W. Kohn. *Phys. Rev.*, 136:–864, 1964.

[17] W. Kohn and L. J. Sham. Self-consistent equations including exchange and correlation effects. *Phys. Rev.*, 140(4A):–1133, Nov 1965.

[18] N. Agraït, A. Levy Yeyati, and Jan M. van Ruitenbeek. *Physics Reports*, 377:81–279, 2003. and references therein.

[19] E Scheer and J. C. Cuevas. *Molecular Electronics*. Nanoscience and Nanotechnology. 2010.

[20] Y. Xue, S. Datta, and M. A. Ratner. *J. Chem. Phys.*, 115:4292, 2001.

[21] Jeremy Taylor, Hong Guo, and Jian Wang. Ab initio modeling of open systems: Charge transfer, electron conduction, and molecular switching of a c_60 device. *Phys. Rev. B*, 63(12):121104, Mar 2001.

[22] J. J. Palacios, A. J. Pérez-Jiménez, E. Louis, and J. A. Vergés. *Phys. Rev. B*, 64:115411, 2001.

[23] J J Palacios, A J Pérez-Jiménez, E Louis, and J A Vergés. Electronic transport through c60molecules. *Nanotechnology*, 12(2):160, 2001.

[24] N. B. McKeown, editor. *Phthalocyanine Materials - Synthesis, Structure and Function*. Cambridge University Press, 1998.

[25] K J Franke, G Schulze, and J I Pascual. Competition of superconducting phenomena and kondo screening at the nanoscale. *Science*, 332(6032):940–4, 2011.

[26] A. Stróżecka, M. Soriano, J. I. Pascual, and J. J. Palacios. Reversible change of the spin state in a manganese phthalocyanine by coordination of co molecule. *Phys. Rev. Lett.*, 109:147202, 2012.

[27] D. Jacob, M. Soriano, and J. J. Palacios. Kondo effect and spin quenching in high-spin molecules on metal substrates. *Physical Review B*, 88(13):134417, 2013.

[28] R. O. Jones and O. Gunnarsson. The density functional formalism, its applications and prospects. *Rev. Mod. Phys.*, 61:689, 1989.

[29] P. Hohenberg and W. Kohn. Inhomogeneous electron gas. *Phys. Rev.*, 136(3B):–864, Nov 1964.

[30] W. Kohn. Nobel lecture: Electronic structure of matter—wave functions and density functionals. *Rev. Mod. Phys.*, 71(5):1253–1266, Oct 1999.

[31] S.H. Vosko, L. Wilk, and M. Nusair. "accurate spin-dependent electron liquid correlation energies for local spin density calculations: a critical analysis". *Can. J. Phys.*, 58:1200, 1980.

[32] G. D. Mahan. *Many-Particle Physics.* Plenum Press, New York, 3 edition, 2000.

[33] John P. Perdew, Kieron Burke, and Matthias Ernzerhof. Generalized gradient approximation made simple. *Phys. Rev. Lett.*, 77:3865–3868, Oct 1996.

[34] A. Szabo and N. S. Ostlund. *Modern Quantum Chemistry.* McGraw-Hill, New York, 1989.

[35] A. D. Becke. Density-functional exchange-energy approximation with correct asymptotic-behavior. *Phys. Rev. A*, 38:3098, 1988.

[36] Chengteh Lee, Weitao Yang, and Robert G. Parr. Development of the colle-salvetti correlation-energy formula into a functional of the electron density. *Phys. Rev. B*, 37(2):785–789, Jan 1988.

[37] All basis sets were obtained from the extensible computational chemistry environment basis set database, version 1.0, as developed and distributed by the molecular science computing facility, environmental and molecular sciences laboratory which is part of the pacific northwest laboratory, p.o. box 999, richland, washington 99352, usa, and funded by the u.s. department of energy. the pacific northwest laboratory is a multi-program laboratory operated by battelle memorial institue for the u.s. department of energy under contract de-ac06-76rlo 1830. contact david feller or karen schuchardt for further information.

[38] Vladimir A. Ukraintsev. Data evaluation technique for electron-tunneling spectroscopy. *Phys. Rev. B*, 53(16):11176–11185, Apr 1996.

[39] T K Yamada, A L Vázquez De Parga, M M J Bischoff, T Mizoguchi, and H Van Kempen. Evaluation of sample spin-polarization from spin-polarized scanning tunneling spectroscopy experiments. *Microscopy research and technique*, 66(2-3):93–104, 2005.

[40] J. Bardeen. Tunnelling from a many-particle point of view. *Phys. Rev. Lett.*, 6(2):57–59, Jan 1961.

[41] Alex D Gottlieb and Lisa Wesoloski. "bardeen's tunnelling theory as applied to scanning tunnelling microscopy: a technical guide to the traditional interpretation". *Nanotechnology*, 17(8):R57, abril 2006.

[42] F. Flores J.M. Blanco and R. Pï¿½rez. "stm-theory: Image potential, chemistry and surface relaxation". *Progress in Surf. Sci.*, 81:403, 2006.

[43] J. Tersoff and D. R. Hamann. Theory and application for the scanning tunneling microscope. *Phys. Rev. Lett.*, 50(25):1998–2001, Jun 1983.

[44] J. Tersoff and D. R. Hamann. Theory of the scanning tunneling microscope. *Phys. Rev. B*, 31(2):805–813, Jan 1985.

[45] E. C. Goldberg, A. Martín-Rodero, R. Monreal, and F. Flores. Molecular orbital theory for chemisorption and physisorption: The case of he on metals. *Phys. Rev. B*, 39(9):5684–5693, Mar 1989.

[46] C. Julian Chen. Theory of scanning tunneling spectroscopy. *J. Vac. Sci. Technol. A*, 6(2):319, 1988.

[47] F. J. Garca-Vidal, A. Martn-Rodero, F. Flores, J. Ortega, and R. Pérez. Molecular-orbital theory for chemisorption: The case of h on normal metals. *Phys. Rev. B*, 44(20):11412–11431, Nov 1991.

[48] N. García, C. Ocal, and F. Flores. Model theory for scanning tunneling microscopy: Application to au(110) (12). *Phys. Rev. Lett.*, 50(25):2002–2005, Jun 1983.

[49] D. Jacob, J. Fernández-Rossier, and J. J. Palacios. "anisotropic magnetoresistance in nanocontacts". *Phys. Rev. B*, 77(16):165412, Apr 2008.

[50] C. Caroli, R. Combescot, P. Nozieres, and D. Saint-James. "direct calculation of the tunneling current". *J. Phys. C: Solid St. Phys.*, 4:916, 1971.

[51] J. J. Palacios, D. Jacob, A. J. Pï¿½rez-Jimï¿½nez, E. S. Fabiï¿½n, E. Louis, , and J. A. Vergï¿½s. Alacant. ab-initio quantum transport package., 2010.

[52] José M. Soler, Emilio Artacho, Julian D. Gale, Alberto García, Javier Junquera, Pablo Ordejón, and Daniel Sánchez-Portal. The siesta method for ab initio order- n materials simulation. *Journal of Physics: Condensed Matter*, 14(11):2745, 2002.

[53] M. J. Frisch et al. Gaussian 09 Revision A.1. Gaussian Inc. Wallingford CT 2009.

[54] C. Toher, A. Filippetti, S. Sanvito, and Kieron Burke. Self-interaction errors in density-functional calculations of electronic transport. *Phys. Rev. Lett.*, 95:146402, Sep 2005.

[55] Max Koentopp and Kieron Burke. Zero-bias molecular electronics: Exchange-correlation corrections to landauer's formula. *Physical Review B*, 73(12), 2006.

[56] C. Toher and S. Sanvito. Effects of self-interaction corrections on the transport properties of phenyl-based molecular junctions. *Phys. Rev. B*, 77:155402, Apr 2008.

[57] J. M. Garcia-Lastra, C. Rostgaard, A. Rubio, and K. S. Thygesen. Polarization-induced renormalization of molecular levels at metallic and semiconducting surfaces. *Phys. Rev. B*, 80:245427, Dec 2009.

[58] J. B. Neaton, Mark S. Hybertsen, and Steven G. Louie. Renormalization of molecular electronic levels at metal-molecule interfaces. *Phys. Rev. Lett.*, 97:216405, Nov 2006.

[59] J. J. Palacios, D. Jacob, and M. Soriano. ANT.G software package. `http://www.dfa.ua.es/en/invest/condens/Alacant`.

[60] D Jacob and J J Palacios. Critical comparison of electrode models in density functional theory based quantum transport calculations. *J Chem Phys*, 134(4):044118, 2011.

[61] Gerd Berghold, Christopher J. Mundy, Aldo H. Romero, Jürg Hutter, and Michele Parrinello. General and efficient algorithms for obtaining maximally localized wannier functions. *Phys. Rev. B*, 61:10040–10048, Apr 2000.

[62] Takashi Miyake and F. Aryasetiawan. Screened coulomb interaction in the maximally localized wannier basis. *Phys. Rev. B*, 77:085122, Feb 2008.

[63] Nicola Marzari and David Vanderbilt. Maximally localized generalized wannier functions for composite energy bands. *Phys. Rev. B*, 56:12847–12865, Nov 1997.

[64] Arrigo Calzolari, Nicola Marzari, Ivo Souza, and Marco Buongiorno Nardelli. Ab initio. *Phys. Rev. B*, 69:035108, Jan 2004.

[65] Nicola Marzari, Arash A. Mostofi, Jonathan R. Yates, Ivo Souza, and David Vanderbilt. Maximally localized wannier functions: Theory and applications. *Rev. Mod. Phys.*, 84:1419–1475, Oct 2012.

[66] Richard Korytár, Miguel Pruneda, Javier Junquera, Pablo Ordejón, and Nicolás Lorente. Band selection and disentanglement using maximally localized wannier functions: the cases of co impurities in bulk copper and the cu(111) surface. *Journal of Physics: Condensed Matter*, 22(38):385601, 2010.

[67] Shubin Liu, José M. Pérez-Jordá, and Weitao Yang. Nonorthogonal localized molecular orbitals in electronic structure theory. *The Journal of Chemical Physics*, 112(4):1634–1644, 2000.

[68] Dmitry A. Ryndyk, Andrea Donarini, Milena Grifoni, and Klaus Richter. Many-body localized molecular orbital approach to molecular transport. *Phys. Rev. B*, 88:085404, Aug 2013.

[69] K. S. Thygesen. Electron transport trough an interacting region: The case of a nonorthogonal basis set. *Phys. Rev. B*, 73:035309, 2006.

[70] Qin Wu and Troy Van Voorhis. Constrained density functional theory and its application in long-range electron transfer. *Journal of Chemical Theory and Computation*, 2(3):765, 2006.

[71] P. H Dederichs, S. Blugel, R. Zeller, and H. Akai. Ground states of constrained systems: Application to cerium impurities. *Phys. Rev. Lett.*, 53:2512, 1984.

[72] Jörg Behler, Bernard Delley, Karsten Reuter, and Matthias Scheffler. Nonadiabatic potential-energy surfaces by constrained density-functional theory. *Phys. Rev. B*, 75:115409, Mar 2007.

[73] K. G. Dyall, I. P. Grant, and S. Wilson. Matrix representation of operator products. *J. Phys. B: At. Mol. Phys.*, 17:493, 1984.

[74] E. B. Stechel, T.G. Schmalz, and J.C. Light. Quantum theory of exchange reactions: Use of nonorthogonal bases and coordinates. *J. Chem. Phys.*, 70:5640, 1979.

[75] Matthew G. Reuter and Robert J. Harrison. Rethinking first-principles electron transport theories with projection operator: The problems caused by partitioning the basis set. *J. Chem. Phys.*, 139:114104, 2013.

[76] D. Jacob, K. Haule, and G. Kotliar. Dynamical mean-field theory for molecular electronics: Electronic structure and transport properties. *Phys. Rev. B*, 82:195115, 2010.

[77] Satyam Priyadarshy, Spiros S. Skourtis, Seteven M. Risser, and David N. Beratan. Bridge-mediated electronic interactions: Differences between hamiltonian and green functions partitioning in a non-orthogonal basis. *J. Chem. Phys.*, 104:9473, 1996.

[78] Satyam Priyadarshy, Spiros S. Skourtis, Seteven M. Risser, and David N. Beratan. Bridge-mediated electronic interactions: Differences between hamiltonian and green functions partitioning in a non-orthogonal basis. *J. Chem. Phys.*, 104:9473, 1996.

[79] Emilio Artacho and Lorenzo Milans del Bosch. Nonorthogonal basis sets in quantum mechanics: Representations and second quantization. *Phys. Rev. A*, 43:5770, 1991.

[80] L.E Ballentine and M. Kolar. Recursion, non-orthogonal basis vectors, and the computation of electronic properties. *Journal of Physics C: Solid State Physics*, 19(7):981, 1986.

[81] David D. O'Regan, Mike C. Payne, and Arash A. Mostofi. Subspace representations in ab initio methods for strongly correlated systems. *Phys. Rev. B*, 83:245124, Jun 2011.

[82] Aurora E. Clark and Ernest R. Davidson. Population analyses that utilize projection operators. *International Journal of Quantum Chemistry*, 93(6):384, 2003.

[83] A. D. Becke. A multicenter numerical integration scheme for polyatomic molecules. *The Journal of Chemical Physics*, 88(4):2547, 1988.

[84] Célia Fonseca Guerra, Jan-Willem Handgraaf, Evert Jan Baerends, and F Matthias Bickelhaupt. Voronoi deformation density (vdd) charges: Assessment of the mulliken, bader, hirshfeld, weinhold, and vdd methods for charge analysis. *J Comput Chem*, 25(2):189–210, 2004.

[85] R. S. Mulliken. Electronic population analysis on lcaoâmo molecular wave functions. i. *The Journal of Chemical Physics*, 23(10), 1955.

[86] L.F. Pacios and P.A. Christiansen. *J. Chem. Phys.*, 82:2664, 1985.

[87] AM Clogston, BT Matthias, M Peter, HJ Williams, E Corenzwit, and RC Sherwood. Local magnetic moment associated with an iron atom dissolved in various transition metal alloys. *Physical Review*, 125(2):541, 1962.

[88] MP Sarachik, E Corenzwit, and LD Longinotti. Resistivity of mo-nb and mo-re alloys containing 1% fe. *Physical Review*, 135(4A):A1041, 1964.

[89] C. Zener. Interaction between the d shells in the transition metals. *Phys. Rev.*, 81:440–444, Feb 1951.

[90] J. Owen, M. Browne, W. D. Knight, and C. Kittel. Electron and nuclear spin resonance and magnetic susceptibility experiments on dilute alloys of mn in cu. *Phys. Rev.*, 102:1501–1507, Jun 1956.

[91] Kei Yosida. Magnetic properties of cu-mn alloys. *Phys. Rev.*, 106:893–898, Jun 1957.

[92] Friedel. *Nuovo Cimento Suppl VII*, 287, 1958.

[93] Philip Warren Anderson. Localized magnetic states in metals. *Physical Review*, 124(1):41, 1961.

[94] Jun Kondo. Resistance minimum in dilute magnetic alloys. *Progress of theoretical physics*, 32(1):37–49, 1964.

[95] JR Schrieffer and PA Wolff. Relation between the anderson and kondo hamiltonians. *Physical Review*, 149(2):491, 1966.

[96] Matteo Cococcioni and Stefano De Gironcoli. Linear response approach to the calculation of the effective interaction parameters in the lda+ u method. *Physical Review B*, 71(3):035105, 2005.

[97] JF Janak. Proof thatâ eâ n i= ε in density-functional theory. *Physical Review B*, 18(12):7165, 1978.

[98] Liwei Liu, Kai Yang, Yuhang Jiang, Boqun Song, Wende Xiao, Linfei Li, Haitao Zhou, Yeliang Wang, Shixuan Du, Min Ouyang, et al. Reversible single spin control of individual magnetic molecule by hydrogen atom adsorption. *Scientific reports*, 3, 2013.

[99] Ying-Shuang Fu, Shuai-Hua Ji, Xi Chen, Xu-Cun Ma, Rui Wu, Chen-Chen Wang, Wen-Hui Duan, Xiao-Hui Qiu, Bo Sun, Ping Zhang, Jin-Feng Jia, and Qi-Kun Xue. Manipulating the kondo resonance through quantum size effects. *Physical Review Letters*, 99(25), 2007.

[100] L. Gao, W. Ji, Y. B. Hu, Z. H. Cheng, Z. T. Deng, Q. Liu, N. Jiang, X. Lin, W. Guo, S. X. Du, W. A. Hofer, X. C. Xie, and H.-J. Gao. Site-specific kondo effect at ambient temperatures in iron-based molecules. *Phys. Rev. Lett.*, 99:106402, 2007.

[101] Aitor Mugarza, Cornelius Krull, Roberto Robles, Sebastian Stepanow, Gustavo Ceballos, and Pietro Gambardella. Spin coupling and relaxation inside molecule–metal contacts. *Nature communications*, 2:490, 2011.

[102] Bryce E. Williamson, Thomas C. VanCott, Michael E. Boyle, G. Christian Misener, Martin J. Stillman, and Paul N. Schatz. Determination of the ground state of manganese phthalocyanine in an argon matrix using magnetic circular dichroism and absorption spectroscopy. *J. Am. Chem. Soc.*, 114:2412, 1992.

[103] J. H. Van Vleck. Theory of the variations in paramagnetic anisotropy among different salts of the iron group. *Phys. Rev.*, 41:208, 1932.

[104] C. E. Housecroft and A. G. Sharpe. *Inorganic Chemistry*. Prentice Hall, 2004.

[105] Lapo Bogani and Wolfgang Wernsdorfer. Molecular spintronics using single-molecule magnets. *Nature materials*, 7(3):179–186, 2008.

[106] G Guillaud, J Simon, and JP Germain. Metallophthalocyanines: Gas sensors, resistors and field effect transistors1in memory of christine maleysson. 1. *Coordination Chemistry Reviews*, 178:1433–1484, 1998.

[107] Forest I Bohrer, Amos Sharoni, Corneliu Colesniuc, Jeongwon Park, Ivan K Schuller, Andrew C Kummel, and William C Trogler. Gas sensing mechanism in chemiresistive cobalt and metal-free phthalocyanine thin films. *Journal of the American Chemical Society*, 129(17):5640–5646, 2007.

[108] Yun Bai, Florian Buchner, Ina Kellner, Martin Schmid, Florian Vollnhals, Hans-Peter Steinrück, Hubertus Marbach, and J Michael Gottfried. Adsorption of cobalt (ii) octaethylporphyrin and 2h-octaethylporphyrin on ag (111): new insight into the surface coordinative bond. *New Journal of Physics*, 11(12):125004, 2009.

[109] Ken Flechtner, Andreas Kretschmann, Hans-Peter Steinrück, and J Michael Gottfried. No-induced reversible switching of the electronic interaction between a porphyrin-coordinated cobalt ion and a silver surface. *Journal of the American Chemical Society*, 129(40):12110–12111, 2007.

[110] Wolfgang Hieringer, Ken Flechtner, Andreas Kretschmann, Knud Seufert, Willi AuwaÌrter, Johannes V Barth, Andreas GoÌrling, Hans-Peter SteinruÌck, and J Michael Gottfried. The surface trans effect: influence of axial ligands on the surface chemical bonds of adsorbed metalloporphyrins. *Journal of the American Chemical Society*, 133(16):6206–6222, 2011.

[111] Jorge Miguel, Christian F Hermanns, Matthias Bernien, Alex KruÌger, and Wolfgang Kuch. Reversible manipulation of the magnetic coupling of single molecular spins in fe-porphyrins to a ferromagnetic substrate. *The Journal of Physical Chemistry Letters*, 2(12):1455–1459, 2011.

[112] Dorota Chylarecka, Christian Wackerlin, Timur K Kim, Kathrin Muller, Frithjof Nolting, Armin Kleibert, Nirmalya Ballav, and Thomas A Jung. Self-assembly and superexchange coupling of magnetic molecules on oxygen-reconstructed ferromagnetic thin film. *The Journal of Physical Chemistry Letters*, 1(9):1408–1413, 2010.

[113] Cristina Isvoranu, Bin Wang, Evren Ataman, Karina Schulte, Jan Knudsen, Jesper N Andersen, Marie-Laure Bocquet, and Joachim Schnadt. Ammonia adsorption on iron phthalocyanine on au (111): Influence on adsorbate–substrate coupling and molecular spin. *The Journal of chemical physics*, 134(11):114710, 2011.

[114] Cristina Isvoranu, Bin Wang, Evren Ataman, Jan Knudsen, Karina Schulte, Jesper N Andersen, Marie-Laure Bocquet, and Joachim Schnadt. Comparison of the carbonyl and nitrosyl complexes formed by adsorption of co and no on monolayers of iron phthalocyanine on au (111). *The Journal of Physical Chemistry C*, 115(50):24718–24727, 2011.

[115] I Horcas, R Fernandez, JM Gomez-Rodriguez, J Colchero, JWSXM Gómez-Herrero, and AM Baro. Wsxm: a software for scanning probe microscopy and a tool for nanotechnology. *Review of Scientific Instruments*, 78(1):013705, 2007.

[116] Ph. Hofmann. *Prog. in Surf. Sci.*, 81:191, 2006.

[117] Knud Seufert, Marie-Laure Bocquet, Willi Auwärter, Alexander Weber-Bargioni, Joachim Reichert, Nicolás Lorente, and Johannes V Barth. Cis-dicarbonyl binding at cobalt and iron porphyrins with saddle-shape conformation. *Nature chemistry*, 3(2):114–119, 2011.

[118] Knud Seufert, Willi AuwaÌrter, and Johannes V Barth. Discriminative response of surface-confined metalloporphyrin molecules to carbon

and nitrogen monoxide. *Journal of the American Chemical Society*, 132(51):18141–18146, 2010.

[119] L. Gao, W. Ji, Y. B. Hu, Z. H. Cheng, Z. T. Deng, Q. Liu, N. Jiang, X. Lin, W. Guo, S. X. Du, W. A. Hofer, X. C. Xie, and H.-J. Gao. Site-specific kondo effect at ambient temperatures in iron-based molecules. *Physical Review Letters*, 99(10), 2007.

[120] O Újsághy, J Kroha, L Szunyogh, and A Zawadowski. Theory of the fano resonance in the stm tunneling density of states due to a single kondo impurity. *Physical review letters*, 85(12):2557, 2000.

[121] A. C. Hewson. *The Kondo problem to heavy fermions.* Cambridge University Press, 1993.

[122] V. Madhavan, W. Chen, T. Jamneala, M. F. Crommie, and N. S. Wingreen. Tunneling into a single magnetic atom: Spectroscopic evidence of the kondo resonance. *Science*, 280:567–569, 1998.

[123] Jiutao Li, Wolf-Dieter Schneider, Richard Berndt, and Bernard Delley. Kondo scattering observed at a single magnetic impurity. *Phys. Rev. Lett.*, 80:2893–2896, 1998.

[124] Nikolaus Knorr, M. Alexander Schneider, Lars Diekhöner, Peter Wahl, and Klaus Kern. Kondo effect of single co adatoms on cu surfaces. *Phys. Rev. Lett.*, 88:096804, 2002.

[125] L. H. Yu, Z. K. Keane, J. W. Ciszek, L. Cheng, J. M. Tour, T. Baruah, M. R. Pederson, and D. Natelson. Kondo resonances and anomalous gate dependence in the electrical conductivity of single-molecule transistors. *Phys. Rev. Lett.*, 95:256803, 2005.

[126] M. Ternes, A. J. Heinrich, and W.-D. Schneider. Spectroscopic manifestations of the kondo effect on single adatoms. *J. Phys.: Condens. Matter*, 21:053001, 2009.

[127] Ph. Noziéres and A. Blandin. Kondo effect in real metals. *J. Physique*, 41:193–211, 1980.

[128] Nicolas Roch, Serge Florens, Theo A. Costi, Wolfgang Wernsdorfer, and Franck Balestro. Observation of the underscreened kondo effect in a molecular transistor. *Phys. Rev. Lett.*, 103:197202, 2009.

[129] J. J. Parks, A. R. Champagne, T. A. Costi, W. W. Shum, A. N. Pasupathy, E. Neuscamman, S. Flores-Torres, P. S. Cornaglia, A. A. Aligia, C. A. Balseiro, G. K.-L. Chan, H. D. Abruña, and D. C. Ralph. Mechanical control of spin states in spin-1 molecules and the underscreened kondo effect. *Science*, 328:1370–1373, 2010.

[130] S. Di Napoli, A. Weichselbaum, P. Roura-Bas, A. A. Aligia, Y. Mokrousov, and S. Blügel. Non-fermi-liquid behavior in transport through co-doped au chains. *Phys. Rev. Lett.*, 110:196402, 2013.

[131] S. Stepanow, P. Miedema, A. Mugarza, G. Ceballos, P. Moras, J. Cezar, C. Carbone, F. de Groot, and P. Gambardella. Mixed-valence behavior and strong correlation effects of metal phthalocyanines adsorbed on metals. *Physical Review B*, 83(22), 2011.

[132] Emi Minamitani, Noriyuki Tsukahara, Daisuke Matsunaka, Yousoo Kim, Noriaki Takagi, and Maki Kawai. Symmetry-driven novel kondo effect in a molecule. *Phys. Rev. Lett.*, 109:086602, 2012.

[133] Luis Dias da Silva, Murilo Tiago, Sergio Ulloa, Fernando Reboredo, and Elbio Dagotto. Many-body electronic structure and kondo properties of cobalt-porphyrin molecules. *Physical Review B*, 80(15), 2009.

[134] Richard KorytÃ¡r and NicolÃ¡s Lorente. Multi-orbital non-crossing approximation from maximally localized wannier functions: the kondo signature of copper phthalocyanine on ag(100). *Journal of Physics: Condensed Matter*, 23(35):355009.

[135] D. Jacob, K. Haule, and G. Kotliar. Kondo effect and conductance of nanocontacts with magnetic impurities. *Phys. Rev. Lett.*, 103:016803, 2009.

[136] F. Aryasetiawan, M. Imada, A. Georges, G. Kotliar, S. Biermann, and A. I. Lichtenstein. Frequency-dependent local interactions and low-energy effective models from electronic structure calculations. *Phys. Rev. B*, 70:195104, 2004.

[137] A. I. Lichtenstein and M. I. Katsnelson. Ab initio calculations of quasiparticle band structure in correlated systems: LDA++ approach. *Phys. Rev. B*, 57:6884–6895, 1998.

[138] M. T. Czyzyk and G. A. Sawatzky. Local-density functional and on-site correlations: The electronic structure of la_2cuo_4 and $lacuo_3$. *Phys. Rev. B*, 49(20):14211–14228, 1994.

[139] K. Haule, S. Kirchner, J. Kroha, and P. Wölfle. Anderson impurity model at finite coulomb interaction u: Generalized noncrossing approximation. *Phys. Rev. B*, 64:155111, 2001.

[140] Johannes Bauer, Jose Pascual, and Katharina Franke. Microscopic resolution of the interplay of kondo screening and superconducting pairing: Mn-phthalocyanine molecules adsorbed on superconducting pb(111). *Physical Review B*, 87(7), 2013.

[141] P. Coleman and C. Pépin. Singular fermi liquid behavior in the underscreened kondo model. *Phys. Rev. B*, 68:220405, 2003.

[142] Nicolas Roch, Serge Florens, Vincent Bouchiat, Wolfgang Wernsdorfer, and Franck Balestro. Quantum phase transition in a single-molecule quantum dot. *Nature*, 453(7195):633–637, 2008.

[143] Lam H Yu and Douglas Natelson. The kondo effect in c60 single-molecule transistors. *Nano Letters*, 4(1):79–83, 2004.

[144] Pablo Jarillo-Herrero, Jing Kong, Herre SJ Van Der Zant, Cees Dekker, Leo P Kouwenhoven, and Silvano De Franceschi. Orbital kondo effect in carbon nanotubes. *Nature*, 434(7032):484–488, 2005.

[145] Stefan Wagner, Ferdinand Kisslinger, Stefan Ballmann, Frank Schramm, Rajadurai Chandrasekar, Tilmann Bodenstein, Olaf Fuhr, Daniel Secker, Karin Fink, Mario Ruben, et al. Switching of a coupled spin pair in a single-molecule junction. *Nature nanotechnology*, 8(8):575–579, 2013.

[146] JJ Parks, AR Champagne, GR Hutchison, S Flores-Torres, HD Abruna, and DC Ralph. Tuning the kondo effect with a mechanically controllable break junction. *Physical review letters*, 99(2):026601, 2007.

[147] Antoine Georges, Gabriel Kotliar, Werner Krauth, and Marcelo J Rozenberg. Dynamical mean-field theory of strongly correlated fermion systems and the limit of infinite dimensions. *Reviews of Modern Physics*, 68(1):13, 1996.

[148] Gabriel Kotliar, Sergej Y Savrasov, Kristjan Haule, Viktor S Oudovenko, O Parcollet, and CA Marianetti. Electronic structure calculations with dynamical mean-field theory. *Reviews of Modern Physics*, 78(3):865, 2006.

[149] C. Sabater, C. Untiedt, J. J. Palacios, and M. J. Caturla. Mechanical annealing of metallic electrodes at the atomic scale. *Phys. Rev. Lett.*, 108:205502, May 2012.

[150] M. Soriano and J. J. Palacios. Theory of projections with non-orthogonal basis sets: Partitioning techniques and effective Hamiltonians. *ArXiv e-prints*, April 2014.

[151] M. Julliere. “tunneling between ferromagnetic films”. *Phys. Lett. A*, 54:225, 1975.

[152] Jp Perdew, K Burke, and M Ernzerhof. "generalized gradient approximation made simple.". *Phys. Rev. Lett.*, 77(18):3865, octubre 1996.

[153] R. Dovesi, V. R. Saunders, C. Roetti, R. Orlando, C. M. Zicovich-Wilson, F. Pascale, B. Civalleri, K. Doll, N. M. Harrison, I. J. Bush, and et al. Crystal06. release 1.0.2., 2006.

[154] M. J. Frisch, G.W. Trucks, H. B. Schlegel, G. E. Scuseria, M. A. Robb, J. R. Cheeseman, J. A. Montgomery, J. T. Vreven, K. N. Kudin, and et al. Gaussian03. revision b.01., 2003.

[155] M. N. Baibich, J. M. Broto, A. Fert, F. N. Van Dau, F. Petroff, P. Eitenne, G. Creuzet, A. Friederich, and J. Chazelas. Giant magnetoresistance of (001)fe/(001)cr magentic superlattices. *Phys. Rev. Lett.*, 61:2472, 1988.

[156] Z. K. Keane, L. H. Yu, and D. Natelson. Magnetoresistance of atomic-scale electromigrated nickel nanocontacts. *Appl. Phys. Lett.*, 88:062514, 2006.

[157] Hirofumi Oka, Kun Tao, Sebastian Wedekind, Guillemin Rodary, Valeri S. Stepanyuk, Dirk Sander, and Jürgen Kirschner. Spatially modulated tunnel magnetoresistance on the nanoscale. *Phys. Rev. Lett.*, 107:187201, Oct 2011.

[158] A. Bagrets et. al. *Nano Lett*, 12:5131, 2012.

[159] Y. Yayon, V. W. Brar, L. Senapati, S. C. Erwin, and M. F. Crommie. Observing spin polarization of individual magnetic adatoms. *Phys. Rev. Lett.*, 99:067202, Aug 2007.

[160] H. Oka, P. A. Ignatiev, S. Wedekind, G. Rodary, L. Niebergall, V. S. Stepanyuk, D. Sander, and J. Kirschner. Spin-dependent quantum interference within a single magnetic nanostructure. 327(5967):843–846, 2010.

[161] B. W. Heinrich, C. Iacovita, M. V. Rastei, L. Limot, J. P. Bucher, P. A. Ignatiev, V. S. Stepanyuk, and P. Bruno. Spin structure of an atomic protrusion: Probing single atoms on cobalt nanoislands. *Phys. Rev. B*, 79:113401, Mar 2009.

[162] S. Datta. *Electronic transport in mesoscopic systems*. Cambridge University Press, Cambridge, 1995.

[163] L. J. Sham and W. Kohn. One-particle properties of an inhomogeneous interacting electron gas. *Phys. Rev.*, 145(2):561–567, May 1966.